



FAKULTÄT FÜR PHYSIK
TECHNISCHE UNIVERSITÄT MÜNCHEN

Structure and Nonlinear Development of Edge Localized Magnetohydrodynamic Instabilities on the ASDEX Upgrade Tokamak

Alexander Felician Mink

Vollständiger Abdruck der von der Fakultät für Physik der Technischen Universität München zur Erlangung des akademischen Grades eines Doktors der Naturwissenschaften genehmigten Dissertation.

Vorsitzender: Prof. Dr. Alejandro Ibarra
Prüfer der Dissertation: 1. Prof. Dr. Ulrich Stroth
2. Prof. Dr. Peter Fierlinger

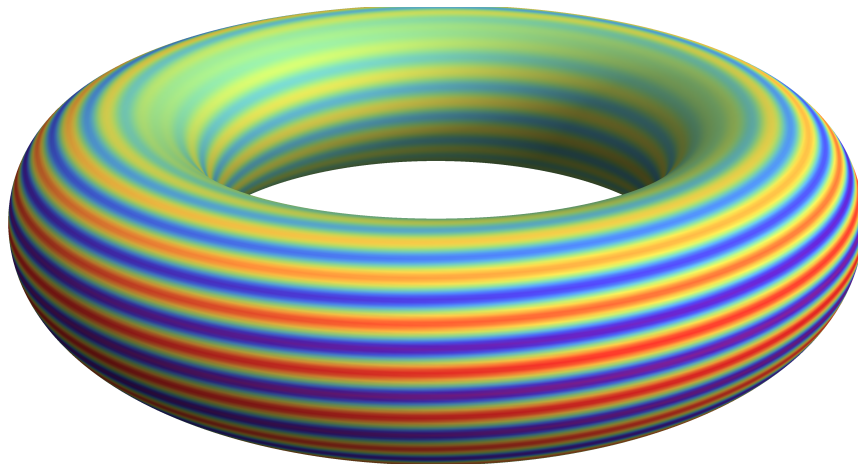
Die Dissertation wurde am 15.02.2018 bei der Technischen Universität München eingereicht und durch die Fakultät für Physik am 11.04.2018 angenommen.



FAKULTÄT FÜR PHYSIK
TECHNISCHE UNIVERSITÄT MÜNCHEN

Structure and Nonlinear Development of Edge Localized Magnetohydrodynamic Instabilities on the ASDEX Upgrade Tokamak

Author: Alexander Felician Mink
Supervisor: Prof. Dr. U. Stroth
Advisor: Univ.-Doz. Dr. E. Wolfrum
Submission Date: 15th February 2018



MAX-PLANCK-GESELLSCHAFT



ASDEX Upgrade



EUROfusion
HELMHOLTZ

RESEARCH FOR GRAND CHALLENGES

I have discovered the secret that after
climbing a great hill, one only finds that
there are many more hills to climb.

N. Mandela, *Long Walk To Freedom*

Abstract

Edge localized modes (ELMs) are magnetohydrodynamic (MHD) instabilities that occur in the high confinement regime (H-mode) of magnetically confined fusion plasmas. ELMs lead to sudden periodic releases of particles and stored energy on a millisecond time scale. These ELM crashes might cause intolerably high heat fluxes onto the divertor target plates or the first wall in future fusion devices. According to the broadly accepted linear peeling-ballooning model these MHD instabilities are driven by edge current density and steep edge pressure gradient, which are characteristic for the H-mode. However, details of the underlying process responsible for ELMs and their nonlinear development during the crashes are not yet fully understood. The focus of this thesis is to determine one of the main characterizing parameters of MHD instabilities, which is the periodic magnetic structure described by the poloidal and toroidal mode numbers m and n . These structures are investigated for ELMs and associated phenomena on the ASDEX Upgrade tokamak.

Mode numbers of instabilities are determined by recently upgraded magnetic pick-up coil arrays. It is shown that mode numbers of high frequency oscillations, $f \geq 50$ kHz, can only be reliably determined if the frequency dependent phase response of the coils is taken into account. Furthermore, a precise ELM synchronization enables the identification of mode numbers during the fast crash of ELMs, which was never achieved before on ASDEX Upgrade. In addition to that, mode numbers and positions of modes appearing between ELM crashes as well as their connection to the edge gradient development are determined for the first time, which is a big step forward in characterizing them and understanding their role for the ELM itself.

Ensembles of modes between ELM crashes are detected with different rotation velocities and thereby different locations at the plasma edge. Modes with higher toroidal mode numbers, $n = 7-13$, appear at the position of fastest poloidal plasma rotation, close to the maximum pressure gradient and might be interpreted as ideal modes without additional phase velocity. Modes with lower toroidal mode numbers, $n = 2-7$, exist further outwards close to the separatrix.

A similar low n structure is present during the ELM crash. The detection of this structure and other parameters of the crash such as induced energy losses or duration enables a quantitative comparison to results from modeling with the nonlinear MHD code JOREK for the first time. Here the $n = 6$ component with smaller structure size is linearly dominant, but nonlinear coupling in which $n = 1$ is particularly important leads to the dominance of larger structure sizes with $n = 3-5$ during the ELM crash which is in excellent agreement with experimental observations.

Moreover, the scaling of the toroidal and poloidal structure, intensity and duration of the ELM crash with plasma parameters is investigated in a database containing various plasma scenarios. It is found that n increases linearly with the inclination of the magnetic field lines, i.e. decreases with safety factor q . Furthermore, no intense ELMs are found at high edge q and no long lasting ELMs are found at low edge q . Other parameters such as normalized pressure gradient α , bootstrap current density j_{BS} or plasma triangularity δ , that should have, according to linear peeling-ballooning theory, an impact on n , do not show clear trends. Introducing a simple geometric model, the scaling of toroidal structure size with q can be explained by the dominance of one poloidal structure.

In order to place the nonlinear phase of ELMs into a wider context of other nonlinear edge phenomena, toroidal mode numbers are analyzed between ELM crashes on the JET tokamak and during ELM crashes mitigated with an external magnetic error field, ELM crashes of nitrogen seeded discharges and ELM-like magnetic bursts of the intermediate confinement regime (I-phase). The JET edge modes are found with similar properties as the ones on ASDEX Upgrade. The ELM crash structure is found to adopt to the one of the external error field while nitrogen seeding seems not to change it. I-phase bursts have the same toroidal structure as ELMs.

The characterization of the modes between and during ELM crashes in terms of mode numbers is a novelty on ASDEX Upgrade, enabling a quantitative comparison with nonlinear theory which is a big step forward in understanding the ELM. The appearance of low n structures during the ELM crash regardless of the variation of peeling-ballooning parameters underlines the fact that the crash phase cannot be described by the linear peeling-ballooning theory, but is caused by nonlinear mode coupling, possibly preferring one poloidal structure.

Zusammenfassung

Randlokalisierte Moden (ELMs) sind magnetohydrodynamische (MHD-) Instabilitäten, die in einem Szenario mit verbessertem Einschluss (H-mode) in magnetisch eingeschlossenen Fusionsplasmen auftreten. ELMs verursachen abrupte, periodische Ausstöße von Teilchen und gespeicherter Energie innerhalb von Millisekunden. Diese ELM-Crashes führen möglicherweise zu untragbar hohen Wärmeflüssen auf die Divertor-Platten oder die Wand zukünftiger Fusionsanlagen. Dem weithin akzeptierten linearen Peeling-Ballooning-Modell zufolge werden diese MHD-Instabilitäten von den für die H-mode charakteristischen Stromdichten und steilen Druckgradienten am Plasmarand ausgelöst. Details der zugrundeliegenden Prozesse, die für ELMs verantwortlich sind, sowie der nichtlineare Verlauf während der Crashes sind hingegen noch nicht vollständig verstanden. Der Fokus dieser Arbeit liegt auf der Bestimmung einer der Haupteigenschaften von MHD-Instabilitäten, nämlich ihrer periodischen magnetischen Struktur, welche durch die poloidalen und toroidalen Modenzahlen m und n beschrieben wird. Diese Struktur wird an ELMs und damit verbundenen Phänomenen am Tokamak ASDEX Upgrade (AUG) untersucht.

Die Modenzahlen der Instabilitäten werden mithilfe einer vor Kurzem erweiterten Anordnung von Magnetfeldsonden ermittelt. Es wird gezeigt, dass Modenzahlen hochfrequenter Ereignisse, $f \geq 50$ kHz, nur dann verlässlich bestimmt werden können, wenn die frequenzabhängige Phasenantwort der Spulen mitberücksichtigt wird. Weiterhin ermöglicht eine präzise ELM-Synchronisierung erstmalig an AUG das Erkennen von Modenzahlen während der schnellen ELM-Crashes. Darüber hinaus werden an Moden, die zwischen ELM-Crashes auftreten, Modenzahlen, radiale Positionen, sowie deren Einfluss auf die Randgradienten bestimmt, was einen großen Schritt für deren Beschreibung und dem Verstehen ihrer Rolle für die ELMs selbst darstellt.

Modensembles zwischen ELM-Crashes werden mit verschiedenen Rotationsgeschwindigkeiten und daraus folgend an verschiedenen Orten am Plasmarand gemessen. Moden mit höheren toroidale Modenzahlen von $n = 7-13$ tauchen an der Stelle mit der schnellsten poloidalen Plasmarotation in der Nähe des Maximums des Druckgradienten auf und könnten als ideale Moden ohne zusätzliche Phasengeschwindigkeit interpretiert werden. Moden mit niedrigeren toroidale Modenzahlen von $n = 2-7$ erscheinen weiter außen nahe der Separatrix.

Eine Struktur mit ähnlich niedrigen Modenzahlen ist während des ELM-Crashes vorhanden. Das Entschlüsseln dieser Struktur und anderer Parameter des Crashes, wie der hervorgerufene Energieverlust oder die Dauer, ermöglichen erstmalig einen quantitativen Vergleich mit Ergebnissen aus Modellierungen des nichtlinearen MHD-Codes JOREK. Hier ist die

Komponente mit $n = 6$, also kleinerer Strukturgröße, linear dominant, aber nichtlineare Kopplung, bei der insbesondere $n = 1$ wichtig ist, führt in exzellenter Übereinstimmung mit experimentellen Ergebnissen zu einer Dominanz von größeren Strukturen mit $n = 3-5$ während des ELM-Crashes.

Darüber hinaus wurde eine Datenbasis aus vielerlei Plasmaszenarien aufgebaut, um damit die Skalierung der toroidalen und poloidalen Modenstruktur, der Intensität und der Dauer des ELM-Crashes mit den Plasmametern zu untersuchen. Es wird beobachtet, dass n linear mit der Steigung magnetischer Feldlinien ansteigt, also mit dem Sicherheitsfaktor q fällt. Weiterhin treten keine intensiven ELMs bei hohem q und keine lang andauernden ELMs bei niedrigem q auf. Weitere Parameter wie der normierte Druckgradient α , die Bootstrap-Stromdichte j_{BS} oder die Triangularität δ des Plasmas, die der linearen Peeling-Ballooning-Theorie folgend einen Einfluss auf n haben sollten, zeigen keine klaren Trends. Mit dem Einführen eines schlichten geometrischen Modells kann jedoch die Skalierung der toroidalen Strukturgröße mit q durch die Dominanz einer poloidalen Struktur erklärt werden.

Um die nichtlineare Phase von ELMs in einem größeren Zusammenhang anderer nichtlinearer Rand-Phänomene zu betrachten, werden solche an dem Tokamak JET und auch in spezielleren Szenarien an AUG untersucht. Dabei zeigen Randmoden an JET ähnliche Eigenschaften wie an ASDEX Upgrade. Ferner passt sich die Struktur der ELM-Crashes der eines zusätzlichen externen Störfeldes an, wird jedoch anscheinend von der Beimischung von Stickstoff nicht verändert. Die Ausbrüche der I-phase haben zu guter Letzt die gleiche toroidale Struktur wie ELMs.

Die Charakterisierung von Moden zwischen und während ELM-Crashes im Sinne von Modenzahlen an ASDEX Upgrade ist ein wichtiger Schritt für das Verständnis von ELMs, da sie erstmalig einen quantitativen Vergleich mit nichtlinearer Theorie erlaubt. Während der ELM-Crashes treten Strukturen unabhängig von den Parametern, die für Peeling-Ballooning-Moden relevant sind, mit niedrigen n -Zahlen auf. Dies unterstreicht die Tatsache, dass die Phase des Crashes nicht durch die lineare Peeling-Ballooning-Theorie beschrieben werden kann, sondern durch nichtlineare Modenkopplung verursacht wird, die möglicherweise eine gewisse poloidale Struktur bevorzugt.

Contents

1. Introduction	1
1.1. Energy Supply	1
1.2. Nuclear Fusion on Earth	3
1.3. Magnetic Confinement and the Tokamak	4
1.4. ASDEX Upgrade Tokamak	7
1.5. H-mode and Edge Localized Modes	8
1.6. Thesis Objectives and Outline	9
2. Magnetohydrodynamics	11
2.1. Magnetohydrodynamic Equations and the Tokamak Equilibrium	11
2.2. Instabilities and Mode Numbers	13
2.3. Edge Localized Modes	17
2.4. Peeling-Ballooning Theory and Beyond	17
2.5. The JOREK Code	20
3. Relevant Diagnostics	23
3.1. Thomson Scattering	23
3.2. Lithium Beam	24
3.3. Electron Cyclotron Emission	25
3.4. Reflectometry	26
3.5. Interferometry	26
3.6. Charge Exchange Spectroscopy	27
3.7. Integrated Data Analysis	27
3.8. Magnetics	28
4. Mode Number Determination with Magnetic Pick-Up Coil Arrays	29
4.1. Mode Number Determination Principle	29
4.2. Examples for Toroidal Mode Number Determination	32
4.3. Examples for Poloidal Mode Number Determination	36
4.4. Influence of Intrinsic Coil Phases	37
4.5. Summary	38
5. Mode Characteristics During the ELM Cycle	39
5.1. Mode Numbers During the ELM Cycle	39
5.1.1. Phase I	45

5.1.2. Phase II	46
5.1.3. Phase III	47
5.1.4. Phase IV	48
5.1.5. Pre-ELM Phase	49
5.1.6. ELM Phase	50
5.2. Radial Position of Modes in the ELM Cycle	52
5.2.1. Position from Velocity Estimation	52
5.2.2. Position from m/n Determination	54
5.2.3. Position from Radially Localized Diagnostics	57
5.3. Poloidal Position of ELM Cycle Modes	59
5.4. Summary and Discussion	60
6. Comparison of the ELM Crash Structure to Nonlinear Simulations	63
6.1. Mode Numbers of the ELM Crash	63
6.2. Experimental Investigations	65
6.3. Nonlinear Simulation of the ELM Crash	68
6.4. Discussion and Outlook	72
7. Influence of Plasma Parameters on the ELM Structure	75
7.1. Mode Numbers Before and During the Crash	75
7.2. Influence of Plasma Parameters on the Structure of the ELM Crash	77
7.2.1. Toroidal Structure of the ELM Crash	81
7.2.2. Poloidal Structure of the ELM Crash	84
7.3. Influence of Plasma Parameters on the ELM Duration and Intensity	88
7.4. Summary and Outlook	91
8. Toroidal Mode Numbers of Various Operation Scenarios	93
8.1. I-phase Bursts	93
8.2. Nitrogen Seeded ELMs	96
8.3. ELMs with Magnetic Perturbations	98
8.4. ELMs at the JET Tokamak	101
8.5. Summary and Conclusion	102
9. Summary and Outlook	103
9.1. Summary and Discussion	103
9.2. Outlook	105
Bibliography	108
A. Details of the JOREK Run	117

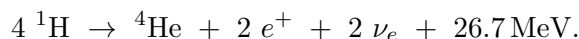
1. Introduction

Since centuries the world's human population and wealth is increasing [1–3]. This is connected with a tremendous increase of energy demand for heating, transport or electricity. The importance of nuclear fusion in providing this energy and how it could be directly used for energy supply is explained in the following with a special focus on the performance limiting edge instabilities of fusion devices.

1.1. Energy Supply

From a physics point of view there are only five possible ways to store energy, which are kinetic energy and the four fundamental potentials given by gravitation, Coulomb interaction, weak nuclear interaction and strong nuclear interaction. The latter is responsible for the energy stored in the atomic nucleus. Figure 1.1 (a) shows this stored energy per nucleon as a function of the mass number for different nuclei. From this plot it can be seen that energy will be released by either fission of heavier nuclei such as ^{235}U or fusion of light nuclei such as ^1H .

Energy supply on earth is in most cases directly or indirectly related to nuclear fission or fusion processes¹. The sun is heated by the exothermic proton-proton chain, where in total 4 protons are fused to helium, two positrons and two neutrinos:



These fusion processes release in total an energy of 26.7 MeV. A fraction of this energy is transported to earth mainly by electromagnetic radiation. Over millions of years this radiation has implanted energy on earth. It is stored in plants by photosynthesis and in the fossil fuels like coal, oil or natural gas that are formed from the plants again over millions of years. Up to now most of the energy is obtained from burning these fossil fuels. This has two main drawbacks. First of all the fossil fuel resources are limited. Second, burning of fossil fuels produces CO_2 and other green-house gases, which are responsible for global

¹The only two exceptions are: Geothermic and tidal power plants: The origin of geothermic heat is a mixture of nuclear fission processes and kinetic energy of the earth and tides are caused by the gravitation of the earth-moon and earth-sun system.

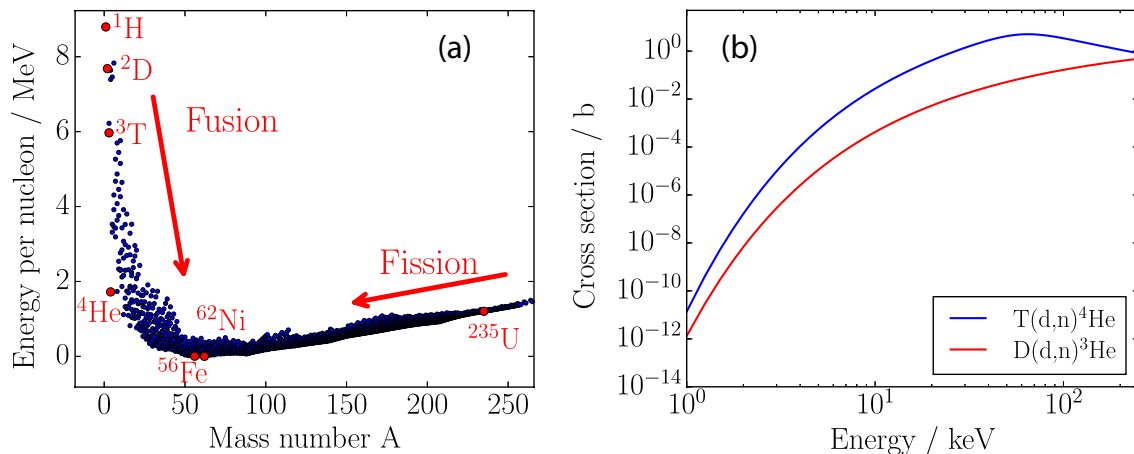


Figure 1.1.: (a) Energy per nucleon for a selection of known elements sorted by their mass number [4]. Some fusion and fission relevant elements are marked in red, i.e. hydrogen, deuterium, tritium, helium, iron, nickel and uranium. Energy can be released by fission of heavier nuclei such as uranium or by fusion of lighter nuclei such as hydrogen. (b) Cross sections against energy in the center of mass system for two exemplary nuclear fusion reactions [5] ².

warming. As global warming most probably causes dramatic and incalculable changes of the environment, it will influence human life significantly. Therefore, burning of fossil fuels has to be avoided.

A much more resources conserving possibility to gain energy originates from the sun directly. This is done in renewable energy power plants, like solar, wind or hydrogen power plants. Solar power plants use the photoelectric effect to produce electric energy directly from electromagnetic radiation from the sun. Wind power plants use the movement of air that is created by heating and cooling of the atmosphere by the sunlight. Finally, hydrogen power plants use the water cycle that is only possible due to the evaporation of water by the sun. The drawback of solar and wind power plants is essentially the availability of sunlight and wind. As both are locally not continuously available, while energy consumption is more or less continuous, energy storage or transport techniques have to be developed to make them a feasible world energy supply method. Hydrogen power plants have the drawback that they need mountain areas or rivers. Therefore, the capacities for water power plants are limited.

The approach of using nuclear energy directly as energy supply is followed since its discovery in the 1930s [6, 7]. Fission of heavy nuclei like ^{235}U is induced by bombarding the nuclei with neutrons. A first controlled fission of nuclei was possible in the 1940s and it contributes since then in an increasing amount to the world's electricity production. The main drawback

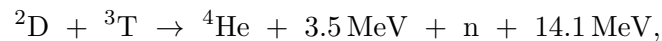
²The unit barn is common in particle physics, $1\text{ b} = 1 \cdot 10^{-28}\text{ m}^2$.

from nuclear fission is the production of various radioactive elements with long half life. Furthermore, the fission of nuclei is always connected with a production of additional neutrons which may then lead to further fission reactions. The thereby induced chain reaction opens up a certain uncontrollability of fission processes. Therefore, it might not be an acceptable method of energy supply in the future.

A last here mentioned approach is to use nuclear fusion directly on earth for electricity production. The probability for proton-proton cycle reactions like in the sun is so low, that a tremendous amount of hydrogen would be needed in order to gain enough power. Therefore, other fusion processes are needed.

1.2. Nuclear Fusion on Earth

Nuclear fusion is only achievable by bringing two nuclei so close together that the strong nuclear force becomes active. The positively charged nuclei therefore have to overcome the repulsive Coulomb force, which is why the particles have to collide with high velocities. This can be achieved if an ensemble of nuclei with a high thermal energy of several keV³ are confined together. At such temperatures atoms form a fully ionized plasma. Figure 1.1 (b) shows the cross section for two exothermic fusion reactions as a function of the center of mass energy. Shown in blue is the cross section for the process



where deuterium and tritium fuse to form helium and a neutron, together with an energy release of 17.6 MeV⁴. It is the process with the highest known cross section⁵. It is therefore the process that is investigated for nuclear fusion on earth. It is also very advantageous in terms of nuclear waste, safety and resources. The product helium is stable and the neutrons cannot lead to a chain reaction. The natural abundance of deuterium is around 0.015% of all hydrogen like atoms, which are present in water molecules. Tritium is not naturally available, but can be bred from lithium, which is abundant in the earth crust. In future fusion power plants the breeding of tritium will be inherently done by placing lithium in the wall, which is bombarded by the neutrons of the D-T process. As tritium is short lived with a half-life of 12.32 a, most present-day fusion research uses only deuterium and hydrogen. As the cross section for an exothermic D-D reaction, cf. red line in figure 1.1 (b), is much lower than for D-T, it is only used for research purposes and will

³1 keV corresponds to a temperature of about 11.6 MK.

⁴This value shows the enormous efficiency of nuclear reactions. In comparison, a chemical reaction like the burning of carbon $\text{C} + \text{O}_2 \rightarrow \text{CO}_2$ only releases 4 eV.

⁵The cross section for the proton-proton chain is by a factor of 10^{-25} smaller [8].

not be feasible for a fusion power plant.

In order to make fusion economically feasible the fusion power gain P_F has to be higher than the power that is put into the plasma for heating P_H . The ratio of both quantities is called the Q factor $Q = P_F/P_H$. In order to achieve a high enough value of Q, temperature, density and confinement have to be adequate. The temperatures have to be about 10 keV in order to balance losses from bremsstrahlung and gain from fusing particles placed in the tail of the energy distribution with energies close to the maximum of the D-T reaction cross section at 65 keV. Therefore, the most difficult part is to confine the plasma at such high temperatures. The quality of the confinement is measured by the energy confinement time τ , which is the energy stored in the plasma divided by the loss power.

There are different methods to confine a fusion plasma. The sun confines it by gravitation. Approaches that could be feasible on earth are inertial confinement [9] and magnetic confinement fusion. The up to now highest value of $Q = 0.64$ was achieved in the JET tokamak research facility [10], which relies on the magnetic confinement principle. The magnetic confinement and the tokamak principle are explained in the following section.

1.3. Magnetic Confinement and the Tokamak

One approach to confine the fusion plasma is the so-called magnetic confinement. At temperatures of several keV, deuterium and tritium form a fully ionized plasma. Ionized particles follow magnetic field lines in a gyro motion, according to the Lorentz force. Toroidal magnetic configurations such as the so-called tokamak can thereby avoid the interaction of the hot charged particles with the wall. 'Tokamak' is a transliteration of the Russian words **toroidalnaya kamera** and **magnitnaya katushka**, which stand for toroidal chamber and magnetic coil [11].

Figure 1.2 shows a sketch of a tokamak forming helically twisted magnetic field lines with a toroidal and a poloidal magnetic field component \vec{B}_ϕ and \vec{B}_θ . Such a combination of fields avoids instabilities of the plasma. In a tokamak the poloidal field is created by inducing a current I_P in the plasma, which is mainly driven by a solenoid placed in the center of the torus and which also contributes to the heating of the plasma. The toroidal magnetic field is produced by coils outside the plasma vessel. It drops with the major radius R . Therefore the inner plasma region is also called the high field side (HFS), whereas the outer region is called the low field side (LFS). The arrangement of the magnetic fields causes the formation of closed nested magnetic flux surfaces, shown in blue, on which the magnetic flux $\psi = \int \vec{B} d\vec{A}$ and the pressure are constant. It is therefore common to introduce the

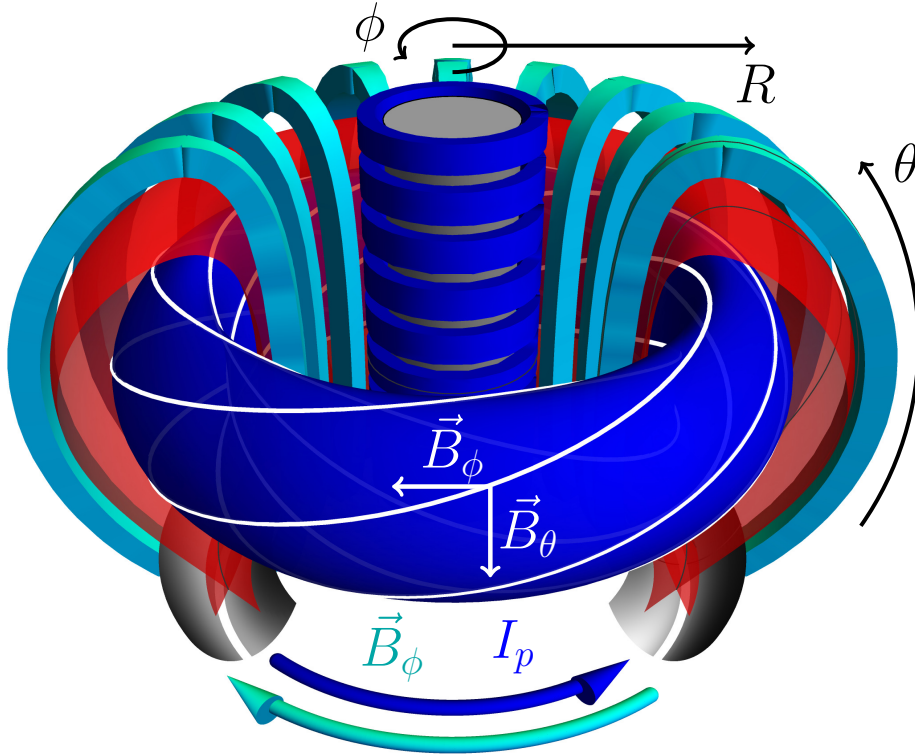


Figure 1.2.: Principle of a tokamak: The central solenoid creates a current I_p in the plasma (blue) yielding a poloidal field \vec{B}_θ . Coils around the plasma create a toroidal field \vec{B}_ϕ (cyan). Both magnetic fields lead to the formation of helically twisted closed field lines (white). The separatrix (red) separates closed and open field lines. Plasma particles further outside are guided onto the divertor (grey). Current and magnetic field directions are shown for the ASDEX Upgrade standard configuration.

magnetic flux label ρ as a radial coordinate ⁶:

$$\rho = \sqrt{\frac{\psi - \psi_0}{\psi_{\text{Sep}} - \psi_0}}, \quad (1.1)$$

where ψ_0 is the magnetic flux on the central magnetic axis ($B_\theta = 0$) and ψ_{Sep} is the flux at the so-called separatrix. The separatrix is the last closed flux surface, shown in red in figure 1.2. On the closed flux surfaces the helical field lines close themselves and therefore

⁶The definition of these surfaces is independent of the choice of the surface orientation $\vec{A}/|A|$, but it is most convenient to choose a surface perpendicular to one of the magnetic fields, i.e. toroidal or poloidal flux. In the following the poloidal flux is chosen ($\rho_{\text{pol}} = \rho$).

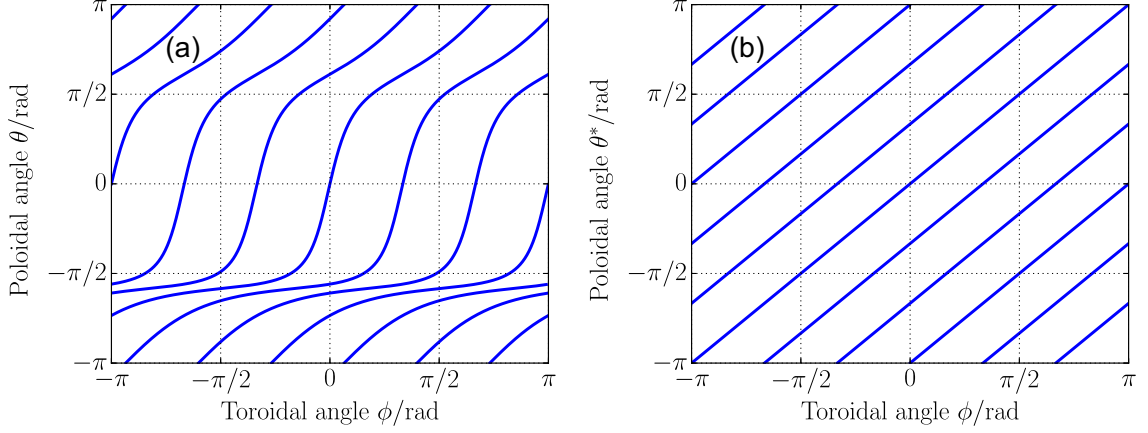


Figure 1.3.: Field lines on a $q = 1$ flux surface in (a) the real space coordinate system and (b) the coordinate system with the straight field line angle θ^* . Due to plasma shaping the slope of the field lines $\Delta\phi/\Delta\theta$ is typically higher at the outboard midplane ($\theta = 0$) and lower close to the so-called X-point ($\theta = -\pi/2$).

confine the particles. The so-called safety factor q ,

$$q = \frac{\text{number of toroidal turns}}{\text{number of poloidal turns}}, \quad (1.2)$$

counts the number of turns that a field line does, before it closes itself. It is proportional to the inverse of the slope of the field lines $\Delta\phi/\Delta\theta$. As the poloidal plasma cross section is not necessarily circular, $\Delta\phi/\Delta\theta$ changes along θ and is therefore only a local measure. This is illustrated in figure 1.3. Therefore, it is common to introduce the so-called straight field line angle θ^* which is defined such, that the slope does not change along θ^* . It furthermore defines the global quantity $q = \Delta\phi/\Delta\theta^*$.

Although single particles are perfectly confined, collisions and collective phenomena such as turbulence introduce perpendicular transport of particles into the region beyond the separatrix. This region is called the scrape off layer. The most successful tokamaks have a divertor configuration. That means that the particles that cross the separatrix are guided along open field lines onto specially hardened plates at the top or bottom of the tokamak. These divertor target plates are shown in grey in figure 1.2.

Table 1.1.: ASDEX Upgrade design parameters [14, 16–18]

Parameter	Value
Plasma current I_p	0.4–1.6 MA
Toroidal field B_ϕ	up to 3.2 T
NBI Heating	20 MW
ECR Heating	4 MW
ICR Heating	4 MW
Major radius R	1.65 m
Minor radius a	0.5 m

1.4. ASDEX Upgrade Tokamak

The ASDEX Upgrade tokamak (AUG)⁷ is a divertor tokamak situated in Garching, Germany. It is equipped with a powerful auxiliary heating system. The high ratio of heating power P_H to the system size given by the major radius R is worldwide unique. AUG is mainly used for ITER [12] and DEMO [13] plasma scenario development [14–16]. Main AUG design parameters are given in table 1.1.

The powerful external heating system on ASDEX Upgrade is based on two different mechanisms, which are explained in the following.

The neutral beam injection (NBI) heating on ASDEX Upgrade consists out of two systems both equipped with four beam sources. In the sources neutral deuterium is ionized. From there it is accelerated with electric fields to energies of about 50–100 keV. The fast particles are neutralized and injected into the plasma. The energy of the injected particles is transferred to the plasma particles via collisions. The power injected into the plasma from one source can be up to 2.5 MW. The maximum injected power from all NBI sources is up to 20 MW.

The injection of electromagnetic waves into the plasma is an effective heating method if the frequency meets a resonance in the plasma. On AUG the electron and ion cyclotron resonances are used. Accordingly, the two heating systems are electron cyclotron resonance heating (ECRH) and ion cyclotron resonance heating (ICRH). The cyclotron resonance frequency is given by charge and mass of the particular particle and the magnetic field $2\pi f = qB/m$. As the B_ϕ drops from HFS to LFS, also the position of the deposited heat can be chosen by choosing the injected frequency. The second harmonic central heating at $B = 2.5$ T by ECRH is achieved for a frequency of $f = 140$ GHz. The maximum injected power from ECRH as well as from ICRH is 4 MW.

ASDEX, the predecessor of AUG, was the first experiment that showed an operation regime

⁷‘Axial Symmetrisches Divertor Experiment’

with unexpectedly low radial transport, i.e. good confinement, which was mainly achieved by increased external heating [19]. Most nowadays tokamaks investigate and rely on this high confinement regime (H-mode). Although the details of this scenario are not yet fully understood, also the next generation tokamak ITER⁸, which is planned to show that it is possible to gain energy from fusion and achieve $Q \geq 10$, will rely on the improved confinement of the H-mode [12]. The general findings, benefits and disadvantages of the H-mode are given in the next section.

1.5. H-mode and Edge Localized Modes

The high confinement mode (H-mode) was discovered in 1982 on the ASDEX tokamak [19]. It is an operational scenario with strongly improved confinement compared to the up to then standard low confinement mode (L-mode). It can only be accessed when overcoming a certain heating power threshold [20, 21]. The main processes responsible for the H-mode take place in the very edge of the plasma. Here the level of fluctuations that cause transport is strongly reduced and an edge transport barrier (ETB) is formed. This transport barrier allows that density, temperature and therefore pressure gradient in the edge get much steeper. Figure 1.4 (a) shows the pressure profile of a discharge with distinct L-mode and H-mode phases (red/blue). As it can be seen the profile is elevated especially in the edge region. This edge area where the gradients are steepest is called the pedestal. From this picture it is clear that the confinement increase is mainly due to the edge region as the gradient continues similar to L-mode further inwards.

Together with the formation of the ETB in H-mode, also a strong plasma flow velocity shear in this region occurs. It is thought that this velocity shear reduces the edge turbulence level by decorrelation of turbulent eddies and thereby decreasing the transport, which enables the formation of the transport barrier [23]. The origin of the edge flow is a radial electric field \vec{E}_r , that leads to a $\vec{E} \times \vec{B}$ plasma drift in the direction perpendicular to the magnetic field, which is mainly upwards on the plasma outboard side⁹. This radial electric field is proportional to the pressure gradient [24]. This shows that the causality in the formation of the H-mode is not yet fully clarified, namely what comes first: the pressure gradient rise or the rise of the velocity shear. Figure 1.4 (b) shows the pressure gradient dp/dr which is essentially proportional to the velocity profile in the edge. From this figure it is again visible that the H-mode has a much stronger velocity shear exactly in the edge region, which enables the reduction of turbulence.

⁸'International Thermonuclear Experimental Reactor' or 'the Way' in Latin

⁹This direction is also called electron diamagnetic drift direction, as electrons drift according to their charge in this direction $\vec{v}_{dia} = -\frac{\nabla p \times \vec{B}}{qnB^2}$. Accordingly, the opposite is called ion diamagnetic drift direction.

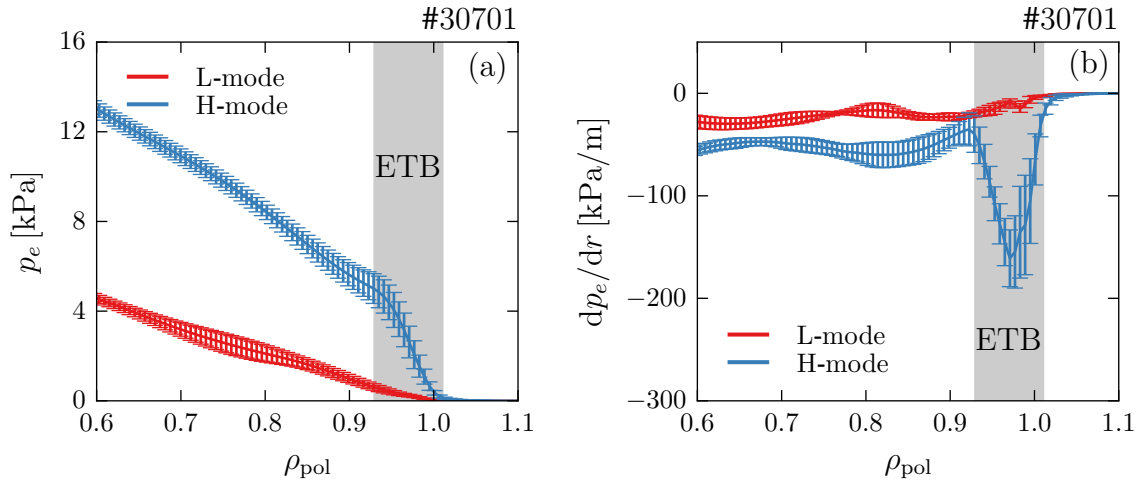


Figure 1.4.: Edge profiles of (a) electron pressure p_e and (b) pressure gradient dp/dr , being responsible for the formation of the edge transport barrier [22].

The additional free energy that is stored in the pedestal of H-mode plasmas gives rise to another phenomenon that is typical for the H-mode, which is the so called edge localized mode (ELM). The ELM periodically destroys the pedestal and thus leads to events with strong heat fluxes across the separatrix and onto the first wall materials. In future fusion machines ELMs will be a serious issue as their induced heat loads might reach the material limits of about 0.3 GWm^{-2} [25–27]. Therefore, it is of high interest to understand the mechanism that leads to ELMs in order to develop techniques to control these instabilities. As this thesis aims at giving a better understanding of the ELM, the theory behind the ELM is explained in further details in chapter 2.

1.6. Thesis Objectives and Outline

Edge localized modes (ELMs) limit the pedestal gradient and thereby the performance of magnetically confined fusion plasmas. Furthermore, they might lead to critical heat loads onto the first wall materials in future fusion devices.

The aim of this thesis was to deliver a better understanding of ELMs during the whole ELM cycle including the ELM crashes and the phases where the pedestal is reestablished and the next ELM starts to evolve. One of the most important characteristics of magnetohydrodynamic modes are their structure determined by the poloidal and toroidal mode numbers m and n . Therefore, these mode numbers are experimentally determined on the ASDEX Upgrade tokamak and compared with linear and nonlinear magnetohydrodynamic models.

In order to do so the determination of toroidal structures was improved by an upgraded magnetic probe system and by taking into account its frequency dependent phase response. Furthermore, a carefully conducted ELM synchronization is used for decomposing the fast ELM event and the modes appearing between ELM crashes.

The role of parameters that are dominantly influencing the ELM crash in the framework of the peeling-ballooning model are evaluated by a wide range database. Instabilities in other plasma regimes are investigated regarding their similarities to ELMs.

The thesis is structured as follows:

Chapter 2 gives an overview on the basic concepts and theories on magnetohydrodynamic instabilities. Main focus here is on the fundamental picture of the edge localized mode drawn from the linear peeling-ballooning model. Chapter 3 explains the diagnostics on the ASDEX Upgrade tokamak, which were relevant for this thesis. Chapter 4 gives a deeper insight into the magnetic diagnostic and explains how it can be used to determine the mode numbers m and n . Furthermore, the limitations of this method are explained and examples of mode number determinations are given. A detailed analysis of one type-I ELM cycle is given in chapter 5. Modes that appear during the ELM cycle are characterized in terms of mode numbers, phase velocity and position. Chapter 6 presents the structure of the ELM crash and compares the properties of the crash to nonlinear simulations with the JOREK code. Chapter 7 contains a database of 30 discharges with 2500 ELMs and investigates the influence of various plasma parameters on the ELM crash properties. Chapter 8 shows the analysis of phenomena similar to the ELM in terms of their toroidal magnetic structure. Chapter 9 concludes the thesis and gives a short outlook on what can be done as next steps.

2. Magnetohydrodynamics

The theoretically exact description of a tokamak plasma with N particles would need to solve a system of $6N$ electromagnetically coupled differential equations. As a typical tokamak volume contains more than 10^{20} particles, this would be computationally impossible. That means that the system can only be described in simplified models. The model that is used and described here is a single fluid picture of the plasma, which is the so-called magnetohydrodynamic (MHD) theory.

The following sections will explain the derivation of the MHD equations, the linear approximations and the basic properties of plasma equilibrium and instability. For further details the reader might be referred to various books [11, 28–30]. The book by *Freidberg* [28] is maybe the best lecture to start with and especially detailed in the derivation of the very basics. *Zohm* [30] is less detailed but includes connections to recent experimental findings.

2.1. Magnetohydrodynamic Equations and the Tokamak Equilibrium

MHD theory describes a plasma with macroscopic quantities like density, velocity, temperature or pressure, similar to hydrodynamics. These macroscopic quantities are derived from integration of velocity weighted Maxwellian distribution functions of the different species over the velocity space. The exact derivation of these quantities can be found in previously mentioned literature [11, 28–30].

Here we start directly from one-fluid quantities. The most dominant ions in a fusion plasma are hydrogen isotopes. Therefore, the charge number can be approximated by $Z = 1$. Together with the much higher mass of the ions compared to the electrons and the charge neutrality in a plasma ($n_e = n_i = n$) this leads to the following simplifications. The mass density

$$\rho_m = n_i m_i + n_e m_e \approx n m_i \tag{2.1}$$

is mainly given by the density and mass of ions. The center of mass velocity

$$\vec{v} = \frac{1}{\rho_m} (n_i m_i \vec{u}_i + n_e m_e \vec{u}_e) \approx \vec{u}_i \quad (2.2)$$

is mainly given by the fluid velocity of the ions \vec{u}_i . The electrical current density

$$\vec{j} = en_i \vec{u}_i - en_e \vec{u}_e = en(\vec{u}_i - \vec{u}_e) \quad (2.3)$$

is given by the difference between ion and electron fluid velocity and the pressure

$$p = p_i + p_e \quad (2.4)$$

is given by the sum of ion and electron pressures.

With these quantities we can formulate the MHD equations. The continuity equation

$$\frac{\partial \rho_m}{\partial t} + \nabla \cdot (\rho_m \vec{v}) = 0, \quad (2.5)$$

the momentum conservation or force balance

$$\rho_m \frac{\partial \vec{v}}{\partial t} = -\nabla p + \vec{j} \times \vec{B}, \quad (2.6)$$

the generalized Ohm's law

$$\vec{E} + \vec{v} \times \vec{B} = \eta \vec{j} + \frac{1}{en} (\vec{j} \times \vec{B} - \nabla p_e) - \frac{m_e}{e^2 n} \frac{\partial \vec{j}}{\partial t} \quad (2.7)$$

with resistivity η and the four Maxwell's equations, which are Gauß's law, Farady's equation, Magnetic Gauß's law and Ampère's law

$$\nabla \cdot \vec{E} = \frac{e}{\epsilon_0} (n_i - n_e) \quad (2.8)$$

$$\nabla \times \vec{E} = -\frac{\partial \vec{B}}{\partial t} \quad (2.9)$$

$$\nabla \cdot \vec{B} = 0 \quad (2.10)$$

$$\nabla \times \vec{B} = \mu_0 \vec{j} + \epsilon_0 \mu_0 \frac{\partial \vec{E}}{\partial t}. \quad (2.11)$$

The last equation needed for closure is an assumption on how pressure and density are related. Here we use the adiabatic equation

$$\frac{d}{dt} \left(\frac{p}{\rho_m^{\gamma_a}} \right) = 0 \quad (2.12)$$

with the adiabatic factor γ_a .

This set of equations is the basis for all MHD calculations. Some further assumptions lead to the so-called ideal MHD equations, like zero resistivity $\eta = 0$, negligence of high frequency and short wavelength fluctuations, $\epsilon_0 = 0$, negligence of electron inertia, $m_e \rightarrow 0$ and negligence of the Hall term $(\vec{j} \times \vec{B} - \nabla p_e)/en \ll \vec{v} \times \vec{B}$. Other assumptions like a toroidal geometry with dominant, time-independent toroidal magnetic field, lead to the so-called reduced MHD equations.

These MHD equations allow to derive how the current, magnetic field and pressure gradient can be arranged in order to achieve a force free situation, i.e. an equilibrium. In such an equilibrium every plasma element is stationary, i.e. $\partial/\partial t \rightarrow 0$. From the force balance equation 2.6 it can be seen that in that case the pressure gradient is balanced by current density and magnetic field, $\nabla p = \vec{j} \times \vec{B}$. From this equation it is clear that the pressure can only change perpendicular to the magnetic field, which shows that the pressure is constant on the previously mentioned flux surfaces. One constellation for achieving an equilibrated plasma is the tokamak, described in section 1.3. The equation that describes the axisymmetric tokamak equilibrium is the Grad-Shafranov equation [28]

$$R \frac{\partial}{\partial R} \left(\frac{1}{R} \frac{\partial \psi}{\partial R} \right) + \frac{\partial^2 \psi}{\partial z^2} = -\mu_0 (2\pi R)^2 \frac{dp}{d\psi} - (2\pi)^2 R B_\phi \frac{d(RB_\phi)}{d\psi}. \quad (2.13)$$

The exact nature, i.e. position and shape, of the equilibrium described by this nonlinear partial differential equations depends mainly on the variation of pressure with the magnetic flux ψ and the toroidal magnetic field B_ϕ . The next section will describe how to determine whether an equilibrium is stable or unstable and how an instability looks like in a tokamak.

2.2. Instabilities and Mode Numbers

In the previous sections it was explained that the tokamak can confine a plasma in a force free situation that is described by the Grad-Shafranov equation. Nevertheless, a force free system can still be stable or unstable against small deviations from the equilibrium. In order to investigate whether a certain parameter combination of ∇p , \vec{j} and \vec{B} leads to instabilities we show here an energy principle of the linearized MHD equations. Of course, the linearized MHD equations do not contain the full physics, but it is easy to see the main plasma instabilities, which are pressure and current driven ones.

For linearizing the MHD equations every quantity Q is written as a sum of its equilibrium value and a small deviation $Q = Q_0 + Q_1$. In addition a small displacement $\vec{\xi}$ of the equilibrium ($\vec{v}_0 = 0$) is defined by $\vec{v}_1 = \frac{d\vec{\xi}}{dt}$. Substituting these definitions and Ampère's

law in the force balance equation, retaining up to first order quantities leads to the linearized force balance equation

$$\begin{aligned} \rho_0 \frac{\partial^2 \vec{\xi}}{\partial t^2} &= \frac{1}{\mu_0} (\nabla \times \vec{B}_0) \times (\nabla \times (\vec{\xi} \times \vec{B}_0)) \\ &+ \frac{1}{\mu_0} (\nabla \times (\nabla \times (\vec{\xi} \times \vec{B}_0))) \times \vec{B}_0 \\ &+ \nabla (\vec{\xi} \cdot \nabla p_0 + \gamma_a p_0 \nabla \cdot \vec{\xi}) \end{aligned} \quad (2.14)$$

which is only dependent on equilibrium quantities and the displacement $\vec{\xi}$. As it is a linear equation it can also be written in the form

$$\rho_0 \frac{\partial^2 \vec{\xi}}{\partial t^2} = \hat{\mathbf{F}} \vec{\xi} \quad (2.15)$$

with the force operator $\hat{\mathbf{F}}$ acting on $\vec{\xi}$. As there is no explicit time dependence on the equilibrium quantities, it is possible to make a temporal Fourier ansatz and separate the time variable from this equation, with $\vec{\xi}(t) = \vec{\xi}_0 \exp(-i\gamma t)$

$$-\gamma^2 \rho_0 \vec{\xi} = \hat{\mathbf{F}} \vec{\xi}. \quad (2.16)$$

This is an eigenvalue equation for the force operator. It can be shown that all eigenvalues are real and therefore the solutions $\vec{\xi}(t) = \vec{\xi}_0 \exp(-i\gamma t)$ are either purely oscillatory ($\gamma^2 > 0$, i.e. stable) or exponentially growing and decaying ($\gamma^2 < 0$, i.e. unstable). Only in very few cases it is possible to find analytic expressions for eigenfunctions and eigenvalues of $\hat{\mathbf{F}}$. Therefore, the next step to get further analytic understanding of the different instabilities appearing in a tokamak is to use the energy principle.

The energy principle formulates the problem not in the force frame but in the energy frame by integration of the force operator:

$$\delta W = -\frac{1}{2} \int \vec{\xi}^* \cdot \hat{\mathbf{F}} \vec{\xi} dV \quad (2.17)$$

with $\vec{\xi}^*$ being the complex conjugate of $\vec{\xi}$. This calculation can then show whether the system depending on $\vec{\xi}$ can get into an energetically better position, i.e. $\delta W < 0$, or not. The integration can be done step-wise in the different regions of the tokamak, i.e. plasma, surface and vacuum. Here we only consider the plasma or fluid part, as the vacuum part is usually stabilizing and the surface part can be neglected in a first approach, assuming that

no surface currents are allowed. The fluid part can be written as [30]

$$\delta W_F = \frac{1}{2} \int_F \left[\frac{|B_{1\perp}|^2}{2\mu_0} + \frac{B_{0\perp}^2}{2\mu_0} |\nabla \cdot \vec{\xi}_\perp + 2\vec{\xi}_\perp \cdot \vec{\kappa}|^2 + \gamma_a p_0 |\nabla \cdot \vec{\xi}|^2 \right. \\ \left. - \underbrace{2(\vec{\xi}_\perp \cdot \nabla p_0)(\vec{\kappa} \cdot \vec{\xi}_\perp^*)}_{\text{pressure}} - \underbrace{\frac{j_{0\parallel}}{B_0} (\vec{\xi}_\perp^* \times \vec{B}_0) \cdot (\nabla \times (\vec{\xi} \times \vec{B}_0))}_{\text{current}} \right] dV, \quad (2.18)$$

with $\vec{\kappa}$ being the curvature of the magnetic field defined as $\vec{\kappa} = (\frac{\vec{B}}{B} \cdot \nabla) \frac{\vec{B}}{B}$ and '||' and '⊥' denoting parallel and perpendicular to the magnetic field.

From this equation one can see the main drivers for instabilities. The first three terms are all positive and give rise to stable Alfvén and sound waves [31]. The last two terms can be negative and are therefore potentially drivers for the two main kinds of instabilities:

Pressure driven instabilities: The pressure term is unstable if pressure gradient ∇p and curvature κ are parallel, whereas this term is stabilizing if they are anti parallel. In the tokamak ∇p points towards the plasma center, whereas the curvature of the toroidal field points towards the center of the tokamak. This leads to the formation of the so-called bad curvature and good curvature regions, which are on the outboard and inboard side of the torus, respectively. These type of instabilities are also called interchange instabilities, similar to the Rayleigh-Taylor instability [32, 33], because the plasma tries to interchange position with the magnetic flux, i.e. field lines get shorter and plasma expands. As the effect is essentially important on the outboard side, the plasma gets blown up in this region similar to a balloon. Therefore, in the tokamak these instabilities are also called 'ballooning instabilities'.

Current driven instabilities: The current term is proportional to the current density parallel to the magnetic field $j_{0\parallel}$. The instability driven by this term leads to a kinking of a plasma tube. The kinking minimizes the total energy although field lines are elongated by the kinked topology. A mechanical analogon is the kinking of a towel, when twisting it. The current that is responsible for the kinking in a tokamak is in many cases not the externally driven current, but the intrinsic bootstrap current [34]. As the bootstrap current can be dominant in the edge, the appearing kinks "peel off" the plasma edge. This is why the edge localized kinks are also called "peeling instabilities" ¹.

¹Although previously neglected, the surface term becomes important when speaking about the edge localized peeling modes.

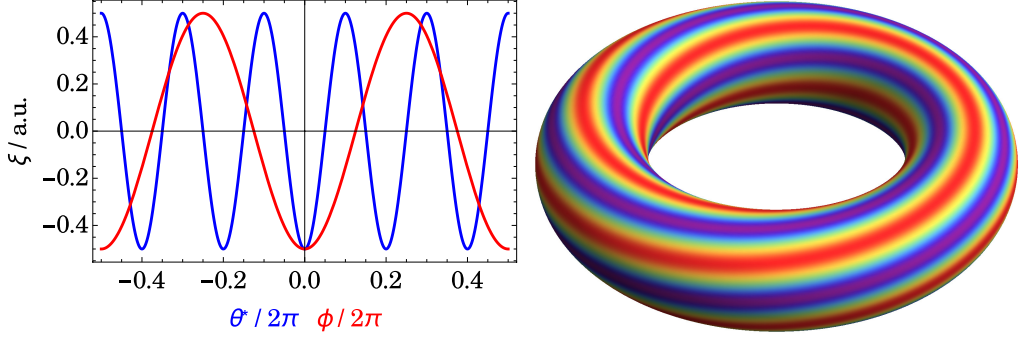


Figure 2.1.: Visualization of the structure ξ of a $(5, 2)$ mode in the tokamak shape (right) and its poloidal and toroidal projection (left).

These are the two major types of instabilities. Up to now no geometry was chosen for the system. Going back to the tokamak, which is periodic in toroidal and poloidal angle ϕ and θ^* , it makes sense to write the displacement vector as a sum of periodic functions in these angles, i.e. make a Fourier decomposition

$$\vec{\xi}(r, \theta^*, \phi) = \sum_{m,n} \vec{\xi}_{m,n}(r) \exp(i(m\theta^* + n\phi)), \quad (2.19)$$

where the periodicities of the displacement m and n are called poloidal and toroidal mode numbers. Thereby each instability is now described by certain combinations of Fourier modes with given (m, n) . As an example figure 2.1 shows the amplitude of the displacement of a $(5, 2)$ mode in the tokamak shape (right) and its poloidal and toroidal projection (left). Continuing the calculation of the energy principle in a tokamak geometry shows that the instabilities most probably appear at that position in the plasma where the periodicities of the instabilities are the same as the one of the field lines, which is reflected by the safety factor

$$q = \frac{m}{n}. \quad (2.20)$$

If this condition is fulfilled, the displacement of the instability follows the field lines. These special positions in the plasma are called rational surfaces. The reason why the instabilities appear there is that the field line bending is minimized if the deformation is field aligned. Obviously this condition is equally well fulfilled by Fourier components with $q = m/n = 2m/2n = 3m/3n \dots$. These Fourier components with higher (m, n) numbers but the same q are also called harmonics. Note that modes that follow field lines have equally separated maxima only in the straight field line system θ^* and only in this system they can be described with one single m .

In summary, modes or instabilities reduce the energy of the plasma and mainly occur in regions of strong pressure gradient or current density close to rational surfaces. All of these conditions are met in the very edge of H-mode tokamak plasmas. These edge localized modes are topic of the next section.

2.3. Edge Localized Modes

Edge localized modes (ELMs) occur as repetitive bursts of magnetic activity and particle and energy losses and thereby inducing high heat fluxes to the wall. Figure 2.2 shows time traces of an AUG discharge including three ELM crashes starting at the red dashed lines. The crashes cause a drop of the plasma stored energy (a), line integrated edge electron density (b) and edge electron temperature (c). The strong rise of the inner divertor shunt current (d) is a measure for the increased temperature in the divertor indicating the increased transport across the separatrix during the crash. The magnetic bursts (e) at the ELM onsets indicate the growth of a magnetohydrodynamic instability. The magnetic signature of these edge instabilities are a major content of this thesis.

Edge localized modes were seen and described for the first time in H-mode scenarios in ASDEX [19, 35]. As mentioned previously the H-mode is characterized by the strong edge pressure gradient. This pressure gradient provides the energy that is released with the ELM crashes. After each crash the pedestal recovers providing the drive for the next crash and thereby completing the ELM cycle. The cyclic behavior is quite reproducible in discharges with constant parameters which makes it possible to determine a so-called ELM frequency f_{ELM} . Nevertheless, varying plasma parameters can lead to strongly varying ELM cycles, which led to the definition of different types of ELMs [36]. However, the type-I ELM, also called 'giant ELM' [37], is of special interest as it is the most common type occurring in developed H-modes causing high energy losses. Therefore, the scope of this thesis is on these 'standard' type-I ELMs. The most accepted basic theory for the type-I ELM is the peeling-ballooning theory. Its basic concepts are explained in the following section.

2.4. Peeling-Ballooning Theory and Beyond

The peeling-ballooning theory is the most accepted theory in order to describe the type-I ELM cycle. However, the basic models that were introduced in the 1980s and 90s [38–40] have developed over the last years quite a lot and can no longer withstand the detailed experimental investigation of the whole ELM cycle. Nevertheless, the rough idea from this basic peeling-ballooning picture is still valid and should be explained here shortly.

Edge H-mode plasmas are characterized by strong pressure gradients providing a strong

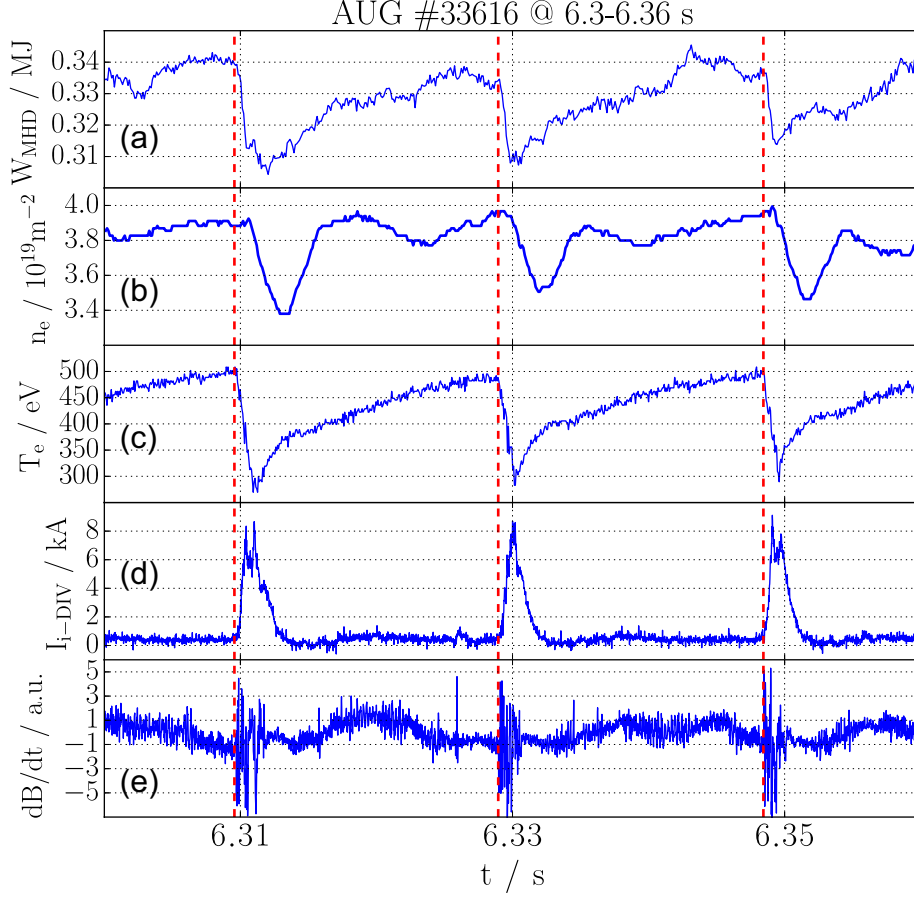


Figure 2.2.: Time trace of the (a) plasma stored energy, (b) line integrated edge electron density, (c) pedestal top electron temperature, (d) inner divertor shunt current, (e) temporal derivative of radial magnetic field. Red dashed lines mark the ELM onsets. Density measurements from interferometry always have slight time delays due to electronics.

drive for the interchange or ballooning modes that were mentioned previously. Similarly, the idea for the drive of the edge localized mode is that a certain normalized pressure gradient

$$\alpha = -Rq^2 \frac{2\mu_0}{B^2} \nabla p \quad (2.21)$$

exists at which a ballooning mode sets in. The mode lowers then the pressure gradient such that the edge is again stable against the ballooning and the pedestal can build up until it reaches the critical α again. This basic idea was supported by measurements in the DIII-D tokamak, which found the origin of the ELM being at the outboard midplane, meaning in the bad curvature region [38]. Nevertheless, the pressure gradient alone cannot be responsible as H-mode plasmas were found to stay above the critical pressure gradient

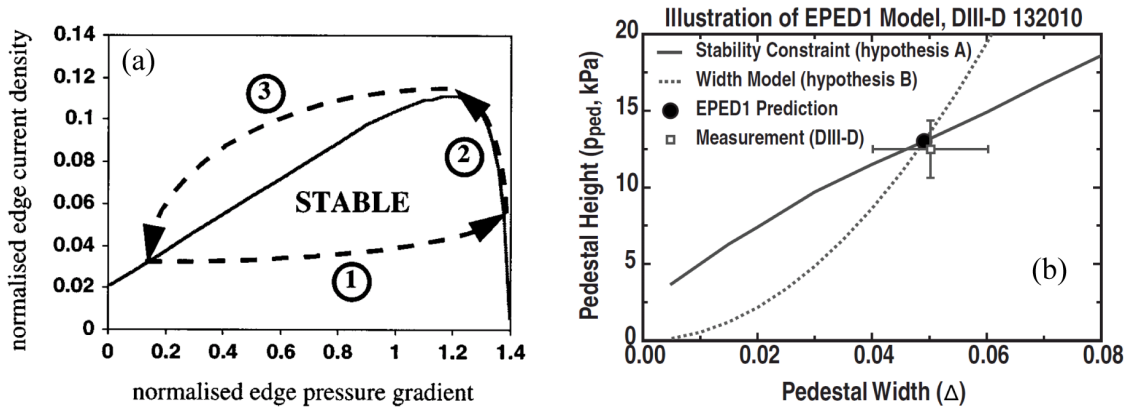


Figure 2.3.: (a) Stability diagram for the combined peeling-ballooning mode. Stable and unstable regions in the parameter space are separated by the solid line, whereas the ELM cycle is indicated with the dashed arrows [40]. (b) Stability diagram for the EPED model containing two boundaries. The onset of modes that allow a growth of pedestal width is determined from the dashed line. The onset of the ELM crash is determined from the solid line [43].

quite some time before the ELM crash appears [41]. Furthermore, it could not be explained how the ballooning mode increases the transport by such a strong factor.

The second ingredient for the peeling-ballooning ELM model is the edge current density [42]. This current density is to a high fraction driven by the bootstrap current, given by [34]

$$j_{bs} \propto \frac{T}{B_\theta} \left(\frac{dn_e}{dr} + \frac{dn_i}{dr} \right) \sim \frac{\nabla p}{B_\theta}. \quad (2.22)$$

As it is roughly proportional to the pressure gradient, it is clear that the H-mode edge is very prone to high current densities. These current densities are the main driver for external kink modes, which are the peeling modes.

Combining both ingredients led in the 90s to the peeling-ballooning model of the ELM cycle, illustrated in Figure 2.3 (a). After an ELM crash the plasma is stable and the pressure gradient increases until a critical α is reached (1). The plasma becomes unstable against very localized ballooning modes. They create enough transport to limit or slightly reduce the pressure gradient, but the bootstrap current still rises due to further reduction of collisionality, i.e. increase of temperature, in the edge (2). This drives at a certain point the peeling mode unstable which causes the strong transport event (3).

The basic idea that neither ballooning nor peeling modes alone explain the ELM cycle is still valid, which is why both driving mechanisms need to be evaluated simultaneously. Therefore, state of the art techniques, like the code MISHKA fast [44], evaluate for certain equilibria in tokamaks the linear peeling-ballooning boundary and find the H-mode edge

plasmas operating always close to this boundary. Also the slightly advanced EPED model, see figure 2.3 (b), which is nowadays broadly accepted, describes the plasma with reaching a certain pressure gradient boundary (given by the dashed line). This pressure gradient creates the drive for a ballooning type of mode, which creates enough transport for almost fixing the gradient. Still the gradient length can grow and thereby creating a broader region in which the unstable mode can develop leading to the ELM crash, which is again a combination of peeling and ballooning mode [43].

However, obtaining predictions or explanations for details of the ELM cycle including the crash behavior is not possible from these linear analysis methods. As a coupling of modes is important, only a nonlinear theory is able to explain the whole dynamics. Several other ingredients like the shear flow or the resistivity might play important roles and have been investigated in the last decades [45–47]. Key aspects for the comparison of experiment and theory are not only the development of pedestal profiles, but also the structure of the appearing modes. The basic idea is that the ballooning mode needs to have high toroidal mode numbers n in order to be localized on the outboard side, whereas the peeling mode is usually most unstable for $n = 1$ or at least low mode numbers $n \leq 5$ [48]. Therefore, the toroidal structure of edge localized modes and associated instabilities was investigated a lot before and is also the main topic of this thesis [36, 49–62].

2.5. The JOREK Code

The numerical code JOREK was developed in order to study the evolution of ELMs [63]. It solves the nonlinear reduced MHD equations on a 3D grid which is decomposed in toroidal direction in Fourier series, whereas bi-cubic Bézier finite elements are used in the poloidal plane for discretization [64]. Thereby a full toroidal X-point geometry including the separatrix and open and closed field lines can be described. The poloidal grid is flux surfaces aligned. Input parameters are pressure and magnetic flux profiles obtained from experimental measurements and solutions of the Grad-Shafranov equation, see equation 2.13. Figure 2.4 shows such a flux surface aligned grid together with a pressure and q profile used for a JOREK simulation. The toroidal decomposition can in principle be done by a selectable amount of Fourier harmonics, which allows a tuning of computational time, which is typically in the order of 10^4 – 10^5 CPU h.

Besides solving the one fluid MHD equations, additional terms describing diamagnetic bi-fluid velocity, neoclassical friction or sources of parallel rotation can be added. Nevertheless, code development and implementation of more advanced features such as a resistive wall is ongoing [66]. Further details on the JOREK code and the derivation of the reduced MHD equations can be found in [67, 68].

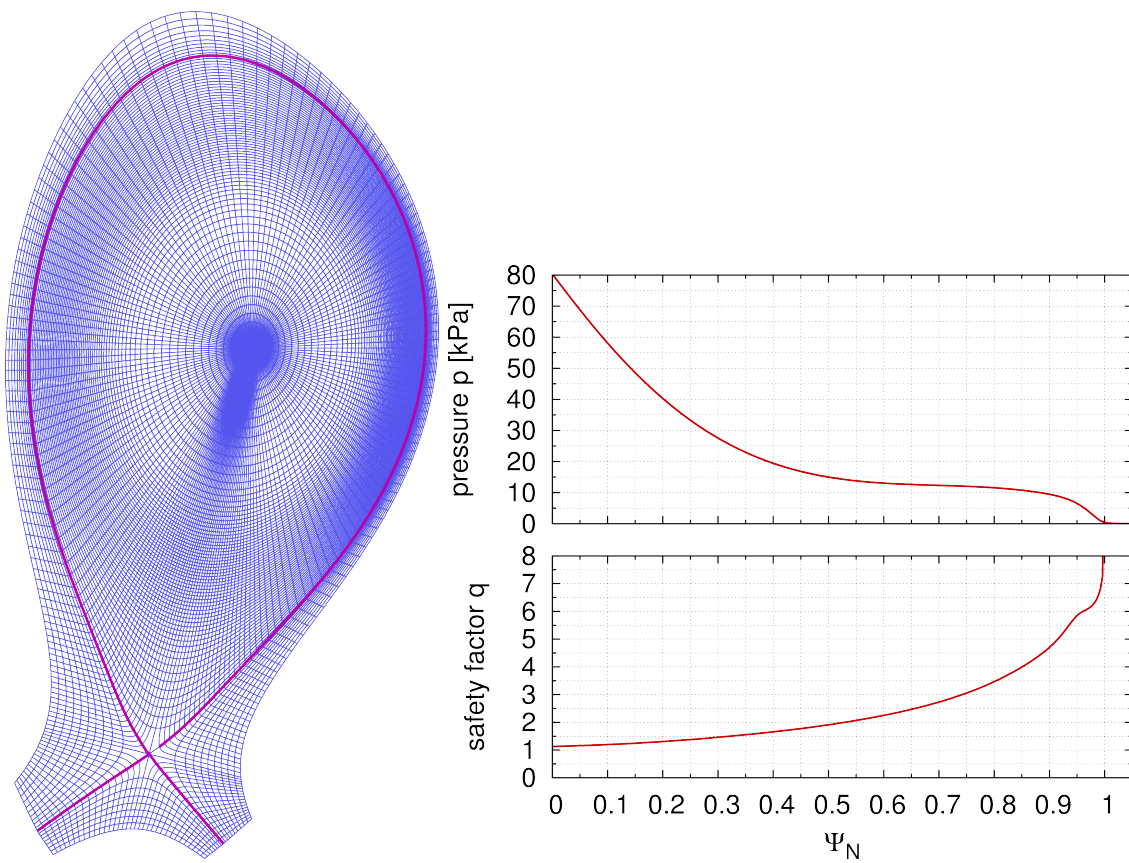


Figure 2.4.: Left: Flux surface aligned X-point grid with separatrix. Right: Profiles of safety factor and pressure ($\psi_N = \rho^2$), taken from [65].

3. Relevant Diagnostics

In this chapter the main diagnostics used in this thesis are explained. Figure 3.1 shows the ASDEX Upgrade tokamak in a poloidal and toroidal projection together with the positions or lines of sight of these diagnostics.

3.1. Thomson Scattering

The Thomson scattering diagnostic is used to gain information on electron density and temperature. The fundamental basis of this diagnostic is the scattering of electromagnetic waves on charged particles, i.e. electrons [69]. In the nonrelativistic dipole approximation the scattered spectrum of an incident wave is proportional to the velocity distribution of the charged particles, which is typically a Maxwellian distribution. The integrated intensity of the spectrum gives information about the electron density n_e , whereas the width of the Maxwellian contains information about the electron temperature T_e . The Thomson scattering diagnostic is a standard diagnostic on various fusion devices [70, 71]. With its possibility of measuring temperature and density at the same position, it is especially used for aligning temperature and density profiles measured from different diagnostics.

The ASDEX Upgrade Thomson system [72] has two beam paths, see figure 3.1. One for probing the edge region and one for the core region of the plasma. Six Nd:YAG lasers with pulse duration of 10 ns, repetition rate of 20 Hz and energies below 1 J are available for the edge region and four for the core region of the plasma. The regions are investigated at 16 scattering volumes in the core and 10 volumes in the edge with a spatial resolution of 25 mm and 3 mm, respectively. These volumes are imaged on the polychromators, which contain four spectral channels with silicon avalanche photodiodes as detectors.

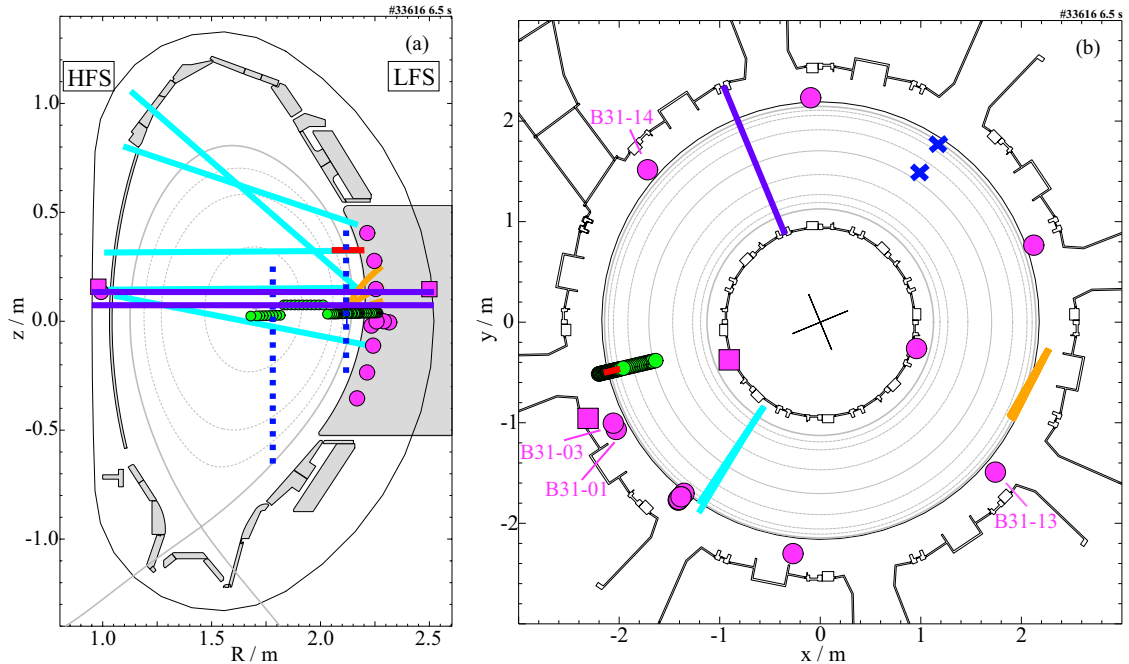


Figure 3.1.: (a) Poloidal and (b) toroidal cross section of the AUG tokamak with positions and lines of sight of the diagnostics used for this thesis: Thomson scattering (blue), lithium beam (red), ECE (green), Interferometry (cyan), CXRS (orange), reflectometers (violet) launched at LFS (upper) and HFS (lower), pick up coils (magenta) measuring radial (circles) and poloidal (squares) magnetic field fluctuations.

3.2. Lithium Beam

The lithium beam diagnostic is used for measuring the electron density of the edge plasma. The basis for this diagnostic is the electron impact excitation of neutral lithium atoms. Therefore, neutral lithium atoms are injected into the plasma. The emitted light from excited atoms at 670.8 nm, corresponding to the transition $2p \rightarrow 2s$ is measured and the emission profile together with a collisional radiative model yield the information on the electron density. As the beam gets attenuated by ionization, ion impact excitation and charge exchange processes the diagnostic is only able to measure the very edge of the plasma [73]. The lithium beam diagnostic is used for gaining the edge density profile on various fusion machines [74, 75].

On ASDEX Upgrade [76] the lithium atoms are launched into the plasma slightly above the LFS midplane, see figure 3.1, with energies of 35–60 keV and a maximum power of 180 W, which makes it also a non perturbative diagnostic. The emission profile is taken by 26+35 channels from two different optical systems with 5–6 mm spatial resolution along the beam. The maximum data acquisition rate is 200 kHz although profile measurements

usually acquire averaging over 50–1000 μs to reduce the noise level. For background light subtraction the beam is chopped with typically 56 ms beam on and 24 ms beam off phases.

3.3. Electron Cyclotron Emission

The electron cyclotron emission (ECE) diagnostic is a standard diagnostic for measuring the electron temperature on many fusion experiments [77, 78]. The basis is the emission and absorption of electromagnetic waves of the gyrating electrons in the strong magnetic field. A single gyrating electron in a magnetic field B emits an electromagnetic wave at the l^{th} harmonics of the gyro frequency:

$$\omega_l = k_{\parallel}v_{\parallel} + l\frac{eB}{\gamma m_e}, \quad l \in \mathbb{N}, \quad (3.1)$$

where k_{\parallel} and v_{\parallel} are the velocity and wavevector components along the magnetic field and $\gamma = (1 - (v/c)^2)^{-1/2}$ is the Lorentz factor.

In a tokamak, the dominant toroidal magnetic field drops with the major radius $B(R) = B_0/R$. Therefore, the light collected from a certain frequency can be assigned a certain origin in the plasma. If all of the emitted light is absorbed by surrounding electrons, i.e. the plasma is optically thick, the emitted intensity approaches the black body radiation characteristic (Rayleigh-Jeans law):

$$I = \omega_l^2 \frac{k_B T_e}{(\pi c)^2}, \quad (3.2)$$

which is proportional to the electron temperature. With this equation the temperature can be calculated from the frequency dependent intensity [79]. However, plasmas can be optically thin especially in the edge region. In this case a more advanced forward modeling of the electron emission profile is needed in order to make proper estimations of the electron temperature profile¹ [81, 82].

The ECE system installed on ASDEX Upgrade measures the 2nd harmonic ECE spectrum with a 60 channel heterodyne radiometer receiver, see figure 3.1, with a sample rate of up to 1 MHz. The receiver is sensitive to frequencies from 85–185 GHz with a band width of 300–600 MHz. This allows a radial resolution depending on the magnetic field of about 5 mm [79, 82].

¹See also: "shine-through" effect, meaning a deviation of the measurement position from the position expected for optical thickness [80]

3.4. Reflectometry

The reflectometry diagnostic can be used for measuring electron density profiles or fluctuations. Basis of this diagnostic is the reflection of microwaves at the cutoff density layer of magnetized plasmas. The plasma frequency ω_p depends on the electron density:

$$\omega_p = \sqrt{\frac{n_e e^2}{m_e \epsilon_0}}. \quad (3.3)$$

An incident microwave with the electric field vector polarized parallel to the magnetic field with frequency ω is reflected from a plasma layer if $\omega_p > \omega$. Due to the density gradient at the plasma edge, also the plasma frequency gradually increases towards the center. Thereby, measuring the delay of a reflected microwave yields the position of the cutoff layer which is connected to a certain density via the plasma frequency. The incident frequency can either be swept for profile determination or can be kept constant in order to measure fluctuations at a fixed position. Reflectometry systems are installed on different fusion devices worldwide [83, 84].

On ASDEX Upgrade various types of reflectometers with different operation regimes and purposes are installed [85–87]. The one used in this thesis measures both on HFS and LFS of the plasma, see figure 3.1. It is able to sweep frequencies between 17 and 100 GHz within 20 μ s for obtaining profiles. On the other hand the system can measure fluctuations typically at fixed frequency at a 2 MHz sample rate [87–89].

3.5. Interferometry

Interferometry is used for measuring the line integrated density. The basis of this diagnostic is to measure the phase of a coherent electromagnetic wave (laser) with frequency ω after a transition through a plasma with refractive index $N = \sqrt{1 - \omega_p^2/\omega^2}$ and of length L given by [69]:

$$\varphi = \int_0^L N \frac{\omega}{c} dl. \quad (3.4)$$

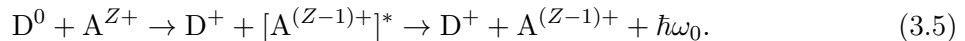
If the laser frequency is much higher than the plasma frequency ω_p , the phase shift $\Delta\varphi$ between a laser going through the plasma and going through vacuum is proportional to the line integrated density.

On ASDEX Upgrade a deuterium cyanide laser with a wavelength of 195 μ m is used as coherent light source. The phase shift $\Delta\varphi$ is measured with a Mach-Zehnder-type interferometer with a heterodyne detection system. Five beam lines pass through the plasma

at different positions, see figure 3.1. The sample rate is 10 kHz [90]. Furthermore, it is equipped with a 4 kHz anti-aliasing filter, which can lead to measurement time delays of up to 250 μ s.

3.6. Charge Exchange Spectroscopy

The charge exchange recombination spectroscopy (CXRS) is used for measuring ion temperature, and plasma rotation. In combination with the force balance equation the radial electric field E_r can be determined. Typically line transitions from impurity ions A that are excited by charge exchange with neutral deuterium atoms are investigated [91]:



The neutral deuterium atoms are injected by means of a diagnostic or a heating beam. The emission spectrum of the excited impurity ions is Gaussian shaped for a thermally equilibrated plasma [69], where the width of the Gaussian is directly connected to the temperature of the impurity ions T_A and the intensity is proportional to the impurity density n_A . Under the assumption that the main ions are also in thermal equilibrium with the impurity ions, the main ion temperature is $T_i = T_A$. Furthermore, the Gaussian intensity distribution is Doppler shifted if the impurity ions rotate. From this Doppler shift the rotation velocity can be obtained.

On ASDEX Upgrade several CXRS systems are installed investigating core and edge regions and poloidal and toroidal rotation velocities from He^{2+}, B^{5+}, C^{6+} or N^{7+} impurity concentrations with various lines of sights and spectrometers. Recent upgrades improved the spatial resolution of the edge CXRS system, see figure 3.1, to 5 mm and the temporal resolution to 50 μ s [92, 93].

3.7. Integrated Data Analysis

The integrated data analysis (IDA) is not a diagnostic itself but a computational tool to combine results from several diagnostics in a self consistent way with a Bayesian probability approach in order to achieve reliable electron density and temperature profiles [94]. The likelihoods for the different diagnostics are calculated from sufficient forward models, e.g. a Gaussian distribution for the Thomson scattering signal. Additional priors, e.g. smoothness, monotonicity or non-negativity constraints, are provided in order to suppress faulty outputs. The integrated diagnostics are the lithium beam, interferometry, Thomson

scattering and ECE, which are all mapped to the normalized poloidal flux coordinate ρ , see chapter 1.3. The output posteriors provide not only measures of density and temperature profiles but also suitable error estimations. IDA typically provides profiles with a 1 ms time resolution.

3.8. Magnetics

Magnetic coils are one of the most common diagnostics on magnetic confinement fusion devices [95, 96]. There are various types of coils with different purpose, but all are based on Faraday's law, see equation 2.9. Accordingly, a voltage U is induced in a wire loop with surface \vec{A} , if a temporally varying magnetic field \vec{B} is penetrating it,

$$U = -\frac{d\Phi}{dt} = -\frac{d(\vec{B} \cdot \vec{A})}{dt}. \quad (3.6)$$

From the vector quantities \vec{B} and \vec{A} , it is clear that coils mounted close to the plasma can measure toroidal, poloidal or radial magnetic flux fluctuations depending on their orientation. One can group the different coils mainly in two groups. One group of coils is used to measure equilibrium quantities, like the total plasma current or plasma position. These quantities are connected to the measured fluxes via the Grad-Shafranov equation, see equation 2.13. As the important quantities here are total flux and not the temporal variation, signals usually need to be integrated over time.

The second group of coils measures deviations from the magnetic equilibrium, which are the instabilities mentioned in section 2.2. These coils are called pick-up coils and are mounted in toroidal or poloidal arrays on ASDEX Upgrade. The coils that were relevant for this thesis are shown in figure 3.1. The toroidal array at the outboard midplane was recently extended to include eight pick-up coils. The data are collected by analog-to-digital converters that measure 512 kHz low-pass filtered voltages from the coils in a range of ± 10 V with a sample rate of 2 MHz [97]. The determination of the mode structure from the phase shift between different coil signals and its limitations are the basis of this thesis and are explained in the next chapter in more details.

4. Mode Number Determination with Magnetic Pick-Up Coil Arrays

In this chapter, the method of determining the mode numbers m and n on ASDEX Upgrade from magnetic pick-up coils is reviewed and examples of mode determinations are presented to show the accuracy and the limits of the method. The significant improvement of the determination of mode numbers of high frequency fluctuations by considering intrinsic coil phases [98] is demonstrated. Furthermore, the self-consistent position determination from poloidal and toroidal mode numbers under the assumption that modes follow the field lines ($q = m/n$) is presented. Parts of the results from this chapter are published in [57].

4.1. Mode Number Determination Principle

For the determination of mode numbers of coherent radial magnetic oscillations two pick-up coil arrays with a sample rate of 2 MHz are installed on ASDEX Upgrade, see figures 3.1 and 4.1. The coils are placed inside the vessel close to the plasma. Coils of the first array are toroidally distributed along the outer midplane. Coils of the second array are poloidally distributed between $\theta \in [-\frac{\pi}{5}, \frac{\pi}{5}]$ at one toroidal angle. The surface normal of each coil points to the geometric center of the torus and therefore they are mainly measuring the temporal derivative of the radial magnetic field \dot{B}_r .

Figure 4.1 shows the periodic structure $B(\phi, \theta^*) = B_0 \sin(m\theta^* + n\phi)$ of a $(m, n) = (5, 2)$ mode and the positions of the magnetic pick-up coils in the θ - ϕ -plane¹. The mode is field aligned to the $q = m/n = 2.5$ flux surface. As mentioned in section 1.3, the real space distance between field lines and thereby distances between maxima and minima of the mode are varying with θ . A conversion to the θ^* system is therefore necessary in order to describe the modes properly with one poloidal mode number m .

If such a mode structure with a wavelength perpendicular to the magnetic field lines

$$\lambda_{\perp} = \left(\left(\frac{n}{U_{\phi}} \right)^2 + \left(\frac{m}{U_{\theta^*}} \right)^2 \right)^{-\frac{1}{2}}, \quad (4.1)$$

¹Figure 2.1 shows the same mode in a 3D representation.

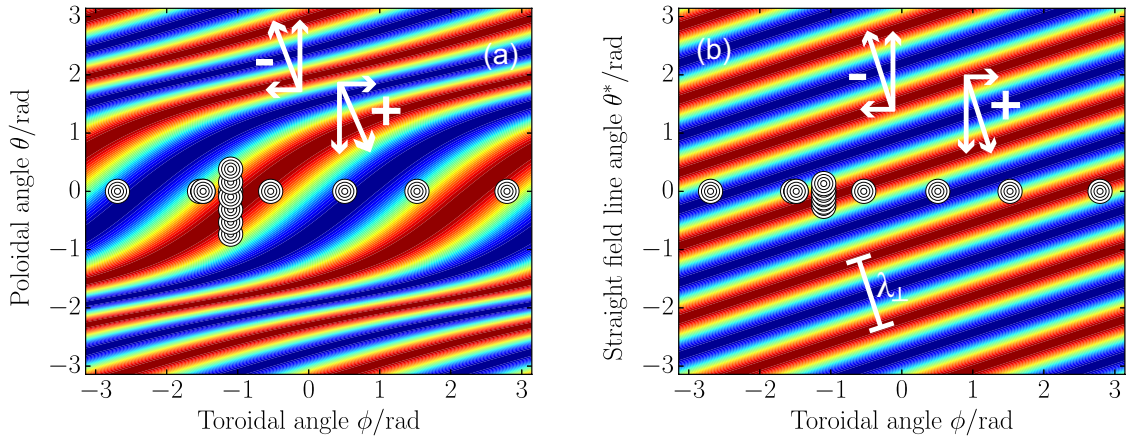


Figure 4.1.: Toroidal and poloidal structure of a (5,2) mode field aligned to the $q = 2.5$ surface in (a) θ and (b) θ^* coordinates together with the pick-up coil arrays (\vec{r} pointing towards the observer). Arrows visualize the sign convention for the mode numbers depending on the propagation for the ASDEX Upgrade standard field configuration.

with the toroidal and poloidal circumference U_ϕ and U_{θ^*} , exists in the rotating plasma, the pick-up coils measure a sinusoidal oscillation. The mode structure and rotation velocity, which can also be described as a sum of toroidal and poloidal rotation \vec{v}_ϕ and \vec{v}_{θ^*} , determine the frequency that is measured

$$\omega = \frac{2\pi\vec{v}_\perp}{\lambda_\perp} = 2\pi \left(\vec{v}_\phi \frac{n}{U_\phi} + \vec{v}_{\theta^*} \frac{m}{U_{\theta^*}} \right). \quad (4.2)$$

Figure 4.2 shows a time trace measured from the pick-up coils B31-13 and B31-14, which are toroidally separated by a toroidal angle $\Delta\phi = \pi$, see figure 3.1. During the present time trace an $n = 1$ structure and weaker harmonics up to $n = 9$, all rotating with the same velocity in the direction of the plasma current ('co-current'), are present. The measured signal (blue) reflects this sum of several sinusoidal structures. The decomposed fluctuations from the most dominant $n = 1$ and $n = 2$ component are plotted in green and red, respectively. From the phase difference $\Delta\varphi$ measured by the coils (dashed black lines) and the position ϕ of the coils the mode number n can be calculated by $n = \Delta\varphi/\Delta\phi$, which is $n = \pi/\pi = 1$ and $n = 2\pi/\pi = 2$, respectively. Furthermore, the rotation velocity can be obtained from the time delay (solid black lines).

If the phases of a coherent magnetic oscillation with a frequency ω measured by each of the coils in the toroidal or poloidal array are known, the associated mode number can be calculated by a linear fit to the phases against the positions ϕ_i (θ_i for the poloidal array)

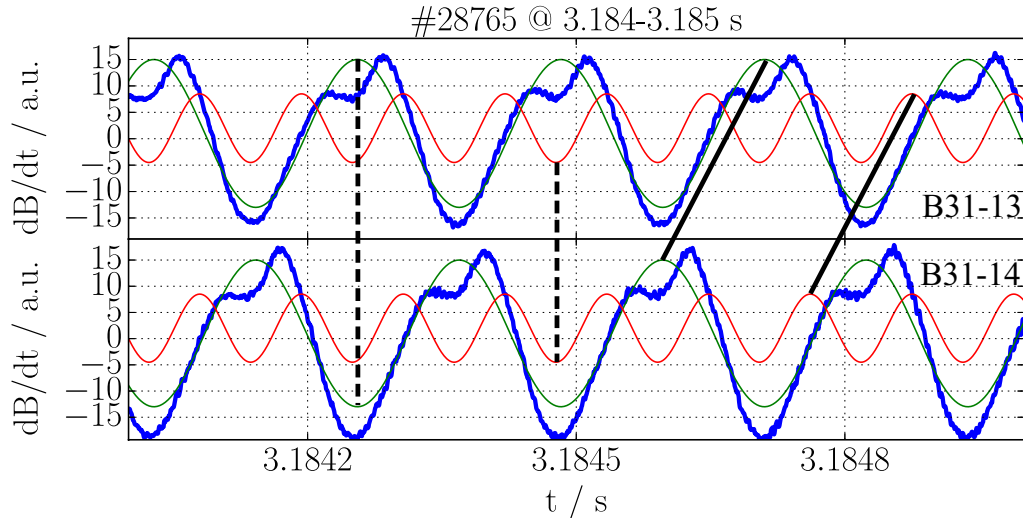


Figure 4.2.: Magnetic fluctuations from an $n = 1$ mode with weaker harmonics measured in the magnetic pick-up coils B31-13 and B31-14 (blue) together with the contribution of the $n = 1$ (green) and $n = 2$ (red) harmonics to the signal. Black dashed lines guide the eye for obtaining the phase differences, while solid lines indicate the propagation velocity.

of the coils². The phases $\varphi_i(\omega)$ of each coil i can be determined from the real part \Re and the imaginary part \Im of the Fourier transform $\hat{S}_i(\omega)$ of the coil signal $S_i(t)$:

$$\varphi = \arctan \left(\frac{\Im(\hat{S})}{\Re(\hat{S})} \right) \quad (4.3)$$

To avoid edge effects in the Fourier analysis of very short time windows, which usually create noise close to $\omega = 0$, it is reasonable to include proper windowing functions. In this case a Gaussian windowing function $W(t)$ was used, which reduces the low frequency noise, without smearing out frequencies strongly:

$$\hat{S}(\omega) = \sum_j S(t_j) W(t_j) \exp(i\omega t_j). \quad (4.4)$$

Figure 4.3 visualizes how a mode number is determined with the whole toroidal pick-up coil array. The data are from a 10 ms time span where the previously discussed harmonics of an $n = 1$ core mode are present. The calculated phases for the present $n = 2$ and $n = 3$ components (with different ω) are plotted against the coil positions ϕ with blue circles. As the calculated phases are limited to values $\varphi \in [-\pi, \pi)$, an $|n| \geq 2$ mode will experience already at least one phase jump of 2π between two coils. Therefore, it is necessary to allow

²The working principle is explained in the following with the toroidal array. All of these basics also hold for the poloidal array distributed along θ .

shifts of the phases by $\Delta\varphi = l(\pm 2\pi)$, $l \in \mathbb{N}$, to calculate the absolute phase of each coil. The mode number is given by the slope of the best fitting line, calculated from a least square regression. In this context the sign of the slope determines the direction of the propagation in the laboratory frame. A positive (negative) slope is connected to a propagation in the ion (electron)-diamagnetic or co (counter)-current direction, which are the directions indicated by the white arrows in figure 4.1. In the present case of two core mode harmonics the fit with a positive slope reproduces the data much better than with the wrong negative slope, which is in line with the plasma core rotation in the direction of the current.

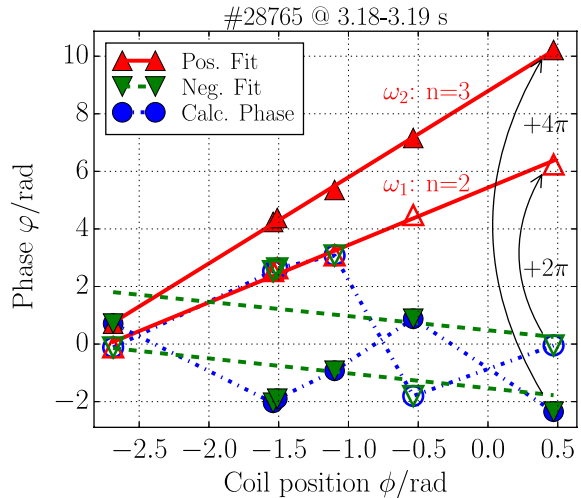


Figure 4.3.: Linear fits to the calculated phases $\varphi(\omega)$ allowing shifts of $\Delta\varphi = l(\pm 2\pi)$, $l \in \mathbb{N}$ for $n = 2$ (ω_1 , open symbols) and $n = 3$ (ω_2 , closed symbols) harmonics measured by the toroidally distributed pick-up coils at positions ϕ .

The poloidal mode numbers m can be obtained in a similar way by using the phase difference φ between poloidally separated

coils. The only difference here is that a conversion to the θ^* coordinate is needed in order to find a linear variation of the phases with the coil position. This conversion can be obtained from the shape and position of the equilibrium, which needs solving the Grad-Shafranov equation 2.13. First of all this is often not possible in a sufficient precision for fast transient events as profile and flux measurements are not accurate enough. Furthermore, the conversion is dependent on q . Therefore, an assumption on the radial position of the mode needs to be taken into account. Assuming that the investigated mode follows the field lines ($q = m/n$) and n is known, the correct m and q can be obtained in an iterative way.

The following subsections show two examples in which toroidal and poloidal mode numbers are determined and give further insights into the limits of the mode number determination.

4.2. Examples for Toroidal Mode Number Determination

Examples which show the precision of the determination of toroidal mode numbers for two different discharges with different MHD phenomena present are given in Figures 4.4 and 4.5. The figures show a coil averaged sliding time window frequency spectrum (a). To create such a frequency spectrum a certain time interval which is given on the top of the plot is

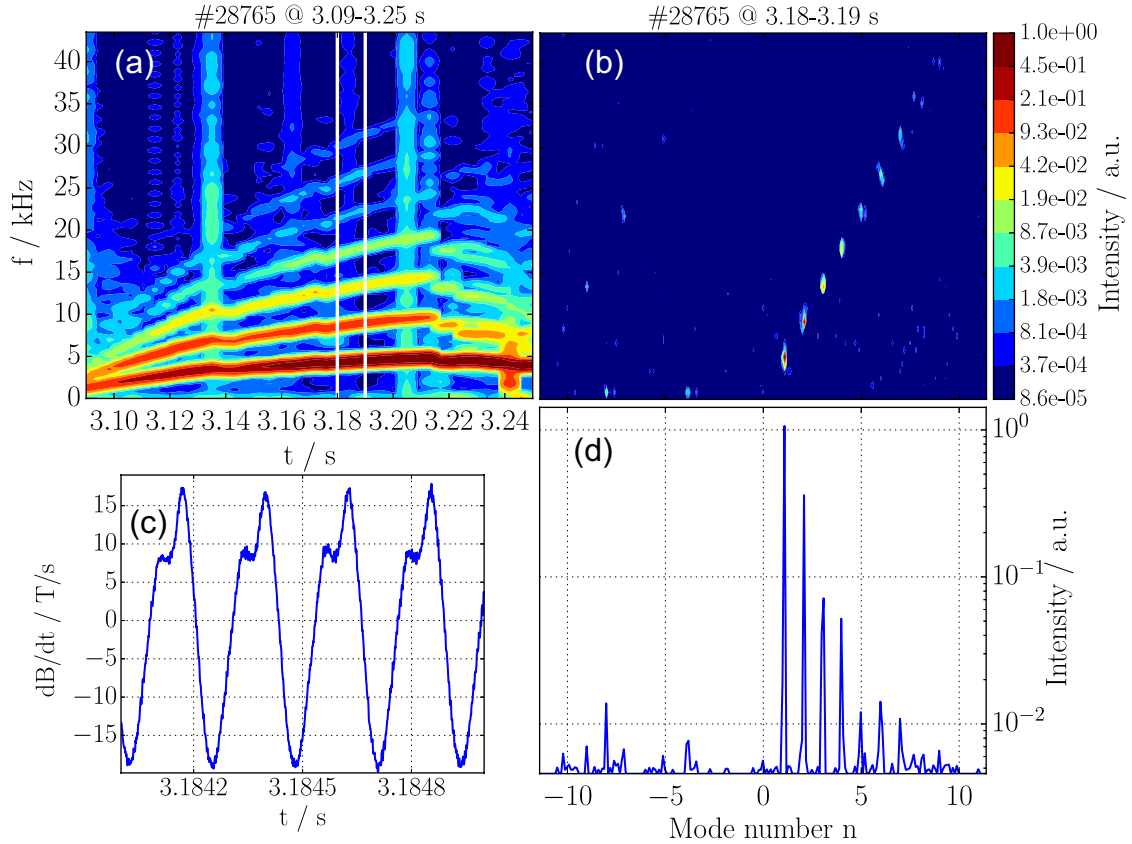


Figure 4.4.: (a) Frequency spectrum, (b) f - n spectrum, (c) magnetic signal of the B31-14 coil and (d) n spectrum for an $n=1$ core mode propagating in the co-current direction and its higher harmonics.

divided into overlapping 1 ms sub-intervals. Spectra from all sub-intervals and all toroidal pick-up coils are obtained by a fast Fourier transformation. The spectra are summed for each sub-interval and normalized to the overall maximum intensity. The frequency spectrum shares both intensity scale and frequency axis with the plot (b).

Plot (b) shows a frequency and toroidal mode number spectrum (f - n spectrum), calculated from a time range with constant plasma conditions, as marked with white vertical lines in the spectrum (a). This time window is then evaluated by the previously described mode number determination method for each frequency. The intensity is again averaged over all coils.

Plot (c) shows the raw signal of one of the magnetic pick-up coils which reflects the characteristic shape of the present mode.

Plot (d) is the toroidal mode number spectrum (n spectrum) obtained from (b) by integrating the intensities over all frequencies. Therefore, it shares the mode number axis with

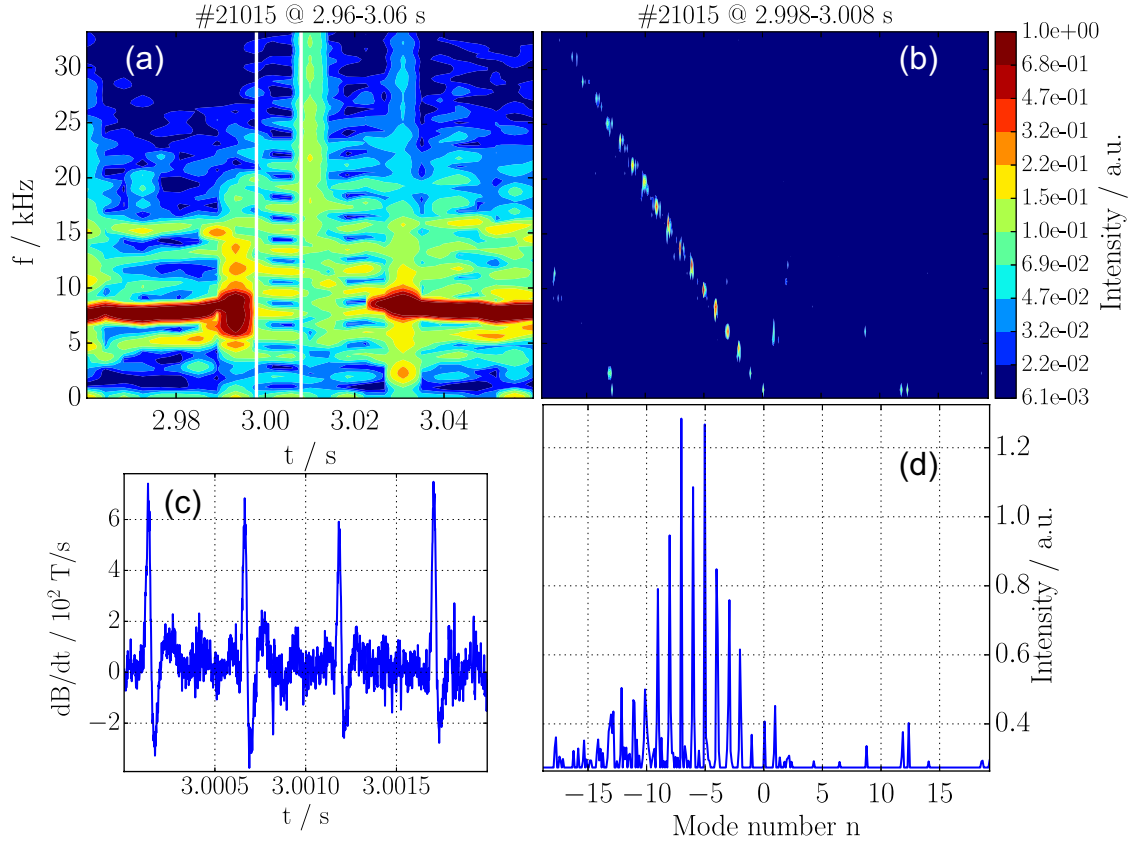


Figure 4.5.: (a) Frequency spectrum, (b) f - n spectrum, (c) magnetic signal of the B31-14 coil and (d) n spectrum for an $n = -(1-16)$ edge snake propagating in the electron diamagnetic direction.

plot (b). The integration can also be restricted to a given frequency range to pronounce special aspects. If a certain range is chosen it is highlighted in the plot itself, otherwise integration is done over the whole frequency range.

In figure 4.4 an $(m, n) = (2, 1)$ core mode with higher harmonics of up to $n = 9$ propagating with the core plasma rotation velocity is analyzed³. The frequency spectrum shows that the core mode rotation velocity increases, leading to a rise of the frequencies. For the f - n spectrum, figure 4.4 (b), a short time interval of 10 ms was chosen such that the frequency stays almost constant. The spectral components of the core mode form a straight line through the origin at $f = 0$ kHz, $n = 0$ in this plot. The formation of such a straight line means that all of the harmonics ($n = 1-9$) have the same f/n value. Hence, they are most

³As shown in the next paragraph the $m = 2$ cannot be calculated from the pick-up coil array mentioned here. There are other magnetic pick-up coil arrays and other diagnostics like XUV measurements that are better suited for poloidal mode number determination of core events that calculate $m = 2$ reliably.

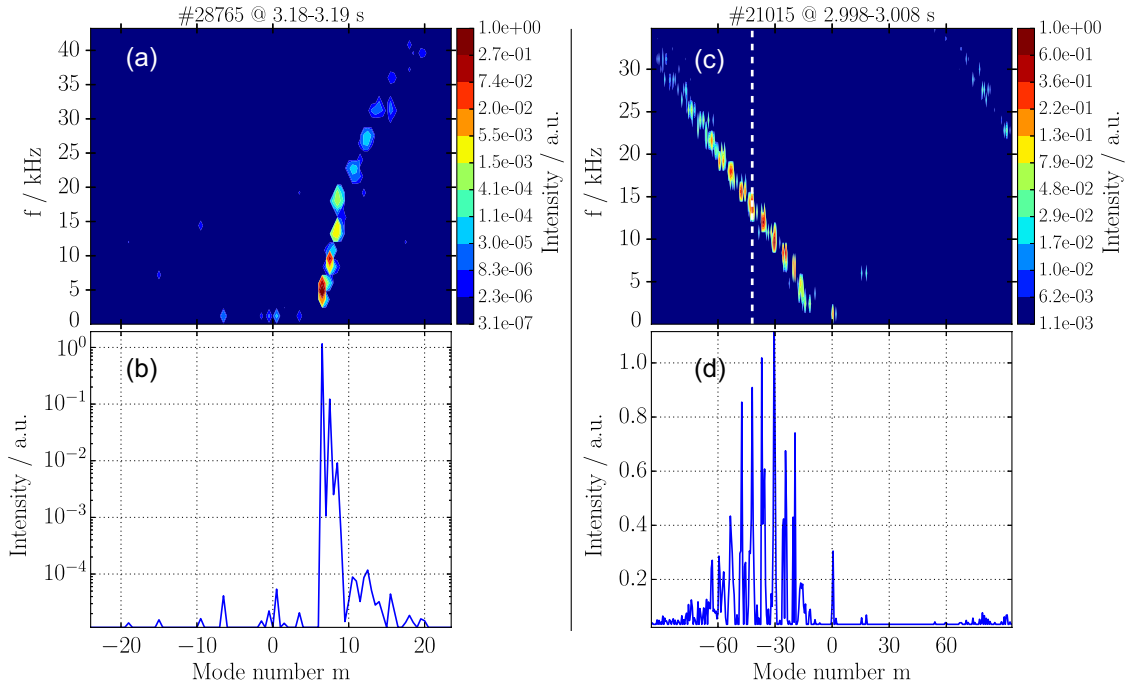


Figure 4.6.: f - m spectrum of (a) a (2,1) core mode and (c) a $q = 6$ edge snake and m spectrum of (b) core mode and (d) edge snake. The $m = 42$ value, fitting to $n = 7$, see figure 4.5, at $f \approx 13$ kHz of the edge snake is marked with a white dashed line.

probably rotating with the same velocity and are therefore at the same radial position in the plasma. Such concise lines are called mode *branches* in the following. The n spectrum shows sharp peaks at $n = 1-9$ but with an almost exponential decrease of intensity. The magnetic raw signal shows the characteristic structure of the $n = 1$ oscillation together with some deformation caused by the much weaker $n = 2$ component. The smaller structures are no longer visible in the magnetic signal because of their weak amplitude.

In figure 4.5, an example of a so-called edge snake [99] is evaluated. It has mode numbers $n = -(1-16)$ and rotates in electron-diamagnetic drift direction. It is located very close to the edge at $q = 6$. It appears on short time scales and is therefore only visible as a number of different frequencies in the spectrum between 2.995–3.025 s. During the presence of the edge snake the magnetic raw signal shows a kind of bursty behavior which is a result of superposed phase aligned oscillations with different frequencies with similar amplitudes. The f - n spectrum shows again very clear peaks with the highest intensity at $n = -7$. Again, all substructures appear on a straight line through the origin, indicating that they together form one structure placed at one radial position.

As it can be seen from the two examples the method of determining toroidal mode numbers works with a high precision for toroidal mode numbers of at least up to $n = 16$. In prin-

principle the highest possible mode number that can be calculated with this method is given by the smallest distance between two coils. In the case of ASDEX Upgrade this is the distance $\Delta\phi_{3,1} \approx 0.05$ rad between the coils B31-03 and B31-01, which would be equivalent to a mode number in the range of $n = \pm\pi/0.05 \approx \pm 62$. However, due to uncertainties in position and phase $n = 62$ cannot be detected. Nevertheless, it is possible to exclude the appearance of very high mode number fluctuations if the phase shift between these two closest coils is small.

4.3. Examples for Poloidal Mode Number Determination

Figure 4.6 shows the mode number spectra for both examples from the previous section, but with poloidal mode numbers (f - m spectrum).

For the (2,1) core mode, figures 4.6 (a,b), the analysis yields a wrong poloidal mode number of $m = 6$ for the $n = 1$ component. Only for high (m, n) combinations the fit results get to conclusive results. For the edge snake, figures 4.6 (c,d), poloidal mode numbers are by far better determined. According to *Sommer et al.* the here investigated edge snake should be in the region where $q = 6$ [99]. This fits perfectly to the obtained results, which are for example (30,5) or $m = 42$ (dashed line) for the $n = 7$ component.

These two examples demonstrate the limits of the poloidal mode number determination with the here used array of coils. Core fluctuations like the (2,1) mode cannot be accurately determined, whereas the method can give a good estimate of structures located very close to the edge. The reason for this is the difference between alignment of the coils and the direction of the magnetic fluctuations from the modes. The coils are aligned along their surface normal \vec{A} , making them most sensitive to the radial magnetic field \vec{B}_r , see Figure 4.7.

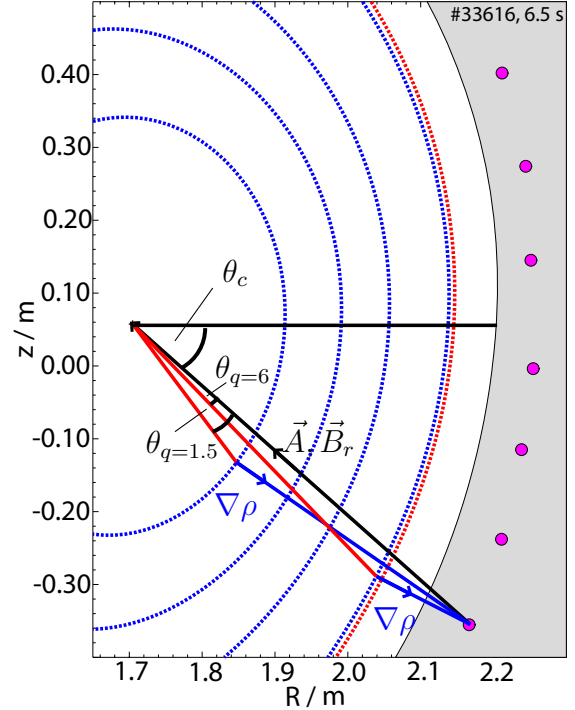


Figure 4.7.: Illustration of the difference between most sensitive angle θ_c of the poloidal array of magnetic pick-up coils (magenta) and angles θ_q from where maximum perturbation is expected (along $\nabla\rho$). The additional phase shift and thereby the m overestimation is stronger at the $q = 1.5$ than for the $q = 6$ surface.

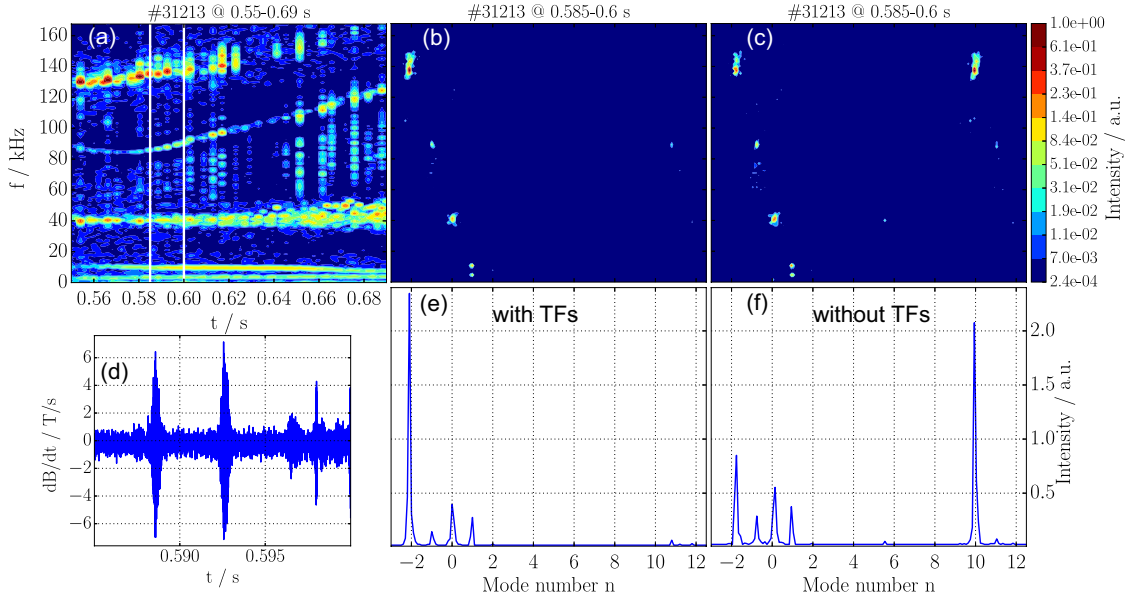


Figure 4.8.: (a) Frequency spectrum, f - n spectra calculated (b) with transfer functions (TFs) and (c) without, (d) signal of the B31-14 coil and n spectra calculated (e) with TFs and (f) without for $n = 1$ core modes, an $n = 0$ GAM, and $n = -1$ and $n = -2$ modes. Omission of TFs leads to significant misinterpretation of the $n = -2$ mode at 140 kHz.

However, perturbations of the field from modes should have their maximum amplitude perpendicular to the field lines (along $\nabla\rho$), which varies depending on the flux surface on which the mode is. The position of the coil is θ_c , while the angle θ_q is the angle from where the maximum amplitude is expected. Thereby, the origin of the phase measured by the coils is in between the direction of the maximum amplitude and maximum sensitivity, which is in between θ_c and $\theta_c + \theta_q$. This effect leads to an overestimation of poloidal mode numbers. The value of the shift is dependent on the flux surface where the mode is. It is smaller for modes further outside ($\theta_{q=6} < \theta_{q=1.5}$) and for higher m modes. This is the reason why core modes are strongly overestimated but correct results can be obtained for edge phenomena.

4.4. Influence of Intrinsic Coil Phases

As mentioned, one issue for the mode number determination is the imprecise knowledge of the measured phase. It was shown by *Horváth et al.* [98] that the installed coils experience intrinsic phase shifts. This can be due to induced eddy currents in the coil surrounding vessel structure or due to resonances in the probe or measuring circuit. The intrinsic phase shifts affect the mode number determination mostly for frequencies $f = 50$ – 250 kHz, where

they reach values of up to 1 radian. Therefore, it was proposed to include frequency dependent phase transfer functions $TF(\omega)$ for each coil to correct for this effect. This leads to a corrected phase $\varphi'(\omega) = \varphi_{meas}(\omega) + TF(\omega)$. These transfer functions can either be measured by externally applied magnetic fields [100] or by measuring the frequency dependent impedance of each coil [97].

Inclusion of the proposed transfer functions leads to a significant improvement of the determination of mode numbers especially in the mentioned frequency range. In figure 4.8 the toroidal mode numbers of several mode structures were determined with and without transfer functions. Again frequency and mode number spectra are plotted together with the magnetic raw signal. The mode number spectra including the transfer functions are shown in figures 4.8 (b) and (e). The ones without transfer functions are shown in figures 4.8 (c) and (f). Clearly visible are $n = 1$ core modes at $f = 5$ and 10 kHz, an $n = 0$ structure at around 40 kHz which can be identified as an geodesic acoustic mode (GAM) [101] and two modes with $n = -1$ and -2 at $f = 90$ and 140 kHz rotating in the electron diamagnetic direction. The magnetic raw signal (d) during the time frame marked in the spectrum (a) shows the bursty behavior of the dominant high frequency $n = -2$ mode.

Results of the mode numbers of low frequency fluctuations like the core mode or the GAM are very reasonable also when the transfer functions and therefore the intrinsic coil phases are omitted. Mode numbers for high frequency fluctuations like the $n = -2$ mode at $f = 140$ kHz can have large errors if the transfer functions are omitted, as in this case the $n = -2$ would be erroneously interpreted as an $n = +10$ mode. As ELM associated fluctuations have frequencies between 50–500 kHz mode numbers of these fluctuations can be determined reliably only when transfer functions are taken into account.

4.5. Summary

With the toroidal pick-up coil array installed on ASDEX Upgrade an accurate determination of the spatial structure of instabilities, i.e. the toroidal mode number, is reliable at least up to $n = 16$. The poloidal pick-up coil array is best suited for determining mode numbers of edge phenomena. Nevertheless, it is only reliable under the assumption that the equilibrium is well known and that modes follow the field lines, i.e. $q = m/n$. Furthermore, an overestimation of poloidal mode numbers especially of core modes is possible due to the geometry of the pick-up coils. The determination of mode numbers at high frequency modes is much improved by taking into account the intrinsic coil phases. Such high frequency modes appear for example between crashes of edge localized modes. These modes are characterized in the following chapter.

5. Mode Characteristics During the ELM Cycle

ELMs lead to a sudden release of the energy stored in the pedestal and thereby they might cause intolerably high heat fluxes onto the divertor target plates or the first wall in future fusion devices like ITER [26]. Therefore, it is necessary to gain a better understanding of the cyclic ELM behavior and especially what triggers the crash.

It has been reported from different tokamaks that in the phase between ELM crashes periodic MHD activities that might be connected to the ELM crash can be observed with defined toroidal mode numbers n in the strong gradient region [61, 102, 103]. As the toroidal mode number is a key parameter for the characterization of modes it is important to determine it for these phenomena to understand their connection to the ELM. Investigation of such mode structures in terms of n is usually done via a determination of the relative phase shift of the magnetic fluctuations collected by toroidally separated magnetic pick-up coils as explained in the previous chapter.

In this chapter a low ELM frequency discharge is used to identify toroidal mode numbers of such oscillations of different phases of an ASDEX Upgrade ELM cycle with the useful technique of ELM synchronization. Furthermore, an estimation of the position of these oscillations from the rotation velocity, poloidal mode numbers and radially localized diagnostics is given followed by an interpretation of the collected information. Parts of the results from this chapter are published in [57].

5.1. Mode Numbers During the ELM Cycle

To resolve different phases during the ELM cycle an ASDEX Upgrade discharge (#28767) with a stationary phase from 2.0 to 2.5s containing 25 ELMs with low ELM frequency of about $f_{\text{ELM}} = 50$ Hz was chosen. Other parameters are plasma current $I_{\text{P}} = 0.8$ MA, heating power $P_{\text{Heat}} = P_{\text{NBI}} + P_{\text{ECRH}} = 2.5 + 1.5$ MW, toroidal magnetic field $|B_{\text{t}}| = 2.5$ T, $q_{95} = 5.2$ and line averaged core electron density $n_{\text{e}} = 6.0 \cdot 10^{19} \text{m}^{-2}$. Figure 5.1 shows time traces of the magnetic pick-up coil signal, the inner divertor shunt current [104], the ELM frequency, the plasma stored energy and the line averaged density at the core and the edge.

5. Mode Characteristics During the ELM Cycle

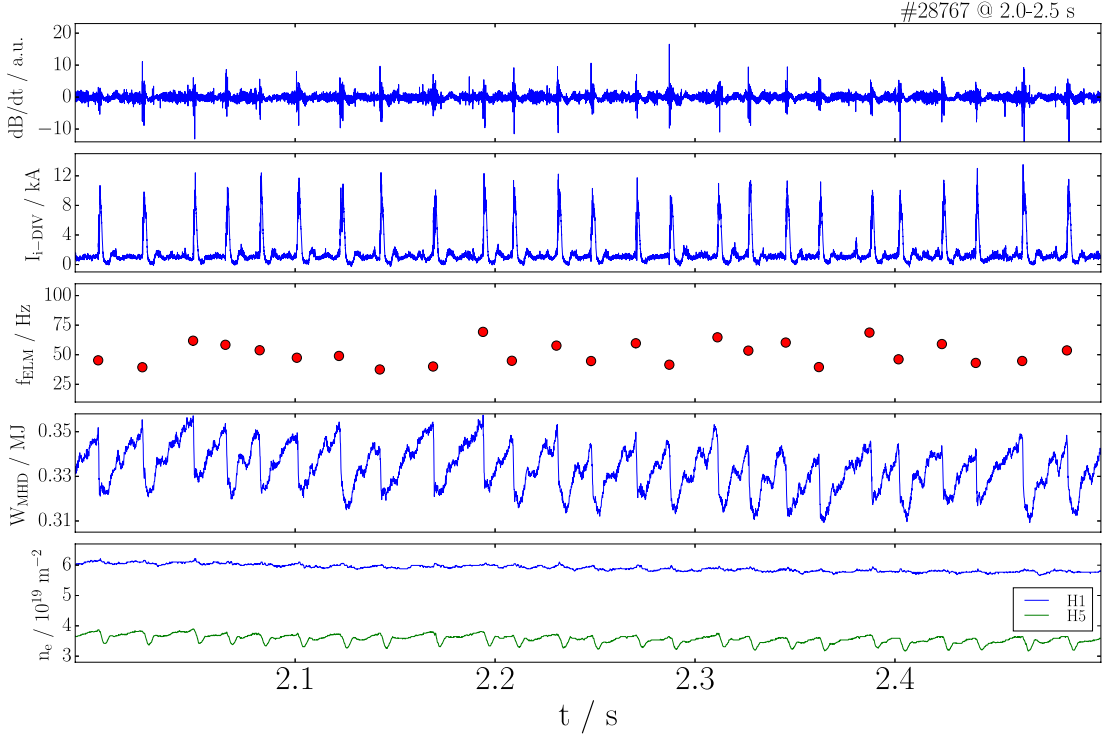


Figure 5.1.: Time traces of the analyzed discharge #28767. Shown are the signals of the magnetic pick-up coil B31-14, the inner divertor shunt current, the ELM frequency, the stored energy calculated from the equilibrium and the line averaged density measured from two interferometry channels through the core (H1) and the edge (H5).

For a discussion of mode numbers of ELM associated phenomena appearing during the chosen discharge magnetic signals and kinetic profiles were ELM synchronized to get enough statistical information. ELM synchronization was previously done with respect to the D_α light or the divertor shunt current signal [105–108]. For the determination of ELM synchronized magnetic coherent signals it was found to be more accurate to synchronize to the rising flank of one magnetic pick-up coil signal at the onset of the ELM crash.

Figure 5.2 presents ELM synchronized data points of the (a) electron temperature T_e and (b) density n_e at the pedestal top ($\rho = 0.965$ and $\rho = 0.98$) evaluated with IDA and (c) the inner divertor shunt current as a measure for the transport over the separatrix. The signals show all 25 ELM crashes synchronized to $t = t_{\text{ELM}}$. Also plotted are smoothed signals of all quantities. From these signals one can identify several phases in the ELM cycles marked by the black vertical lines. These phases will later be related to certain magnetic fluctuations. Further information on the connection between modes in the ELM cycle with pedestal profiles are given in [103, 107–109]. Here only a short description of the phases

in terms of profiles is presented.

The density recovery phase (I) is found right after the ELM crash. Although the recovery starts already a bit earlier and therefore overlaps with the here defined ELM phase, this is the phase during which the density almost recovers from the crash. Together with the density recovery the particle transport over the separatrix decreases. In this phase the electron temperature recovery is slow. As this phase has not yet reached strong gradients in the edge, the drive for modes in the edge is weak.

During the second phase after the ELM crash (II) the temperature recovery accelerates and density reaches its maximum. Also the divertor shunt current as measure for transport across the separatrix reaches its minimum first but starts to increase at the end of this phase.

In the third phase after the ELM crash (III) the temperature recovery slows down again. At the beginning of this phase the pedestal density drops slightly which goes hand in hand with an increased transport visible as an increase of the divertor currents. This increased transport is slightly reduced towards phase (IV) which then happens together with an increase of pedestal density.

Phase (IV) after the ELM crash resets the temperature very slowly to its maximum value. The transport reaches an equilibrium value, which is much higher than the minimum reached in phase (II).

The density at the pedestal top adjusts to similar values as in phase (III). It was shown

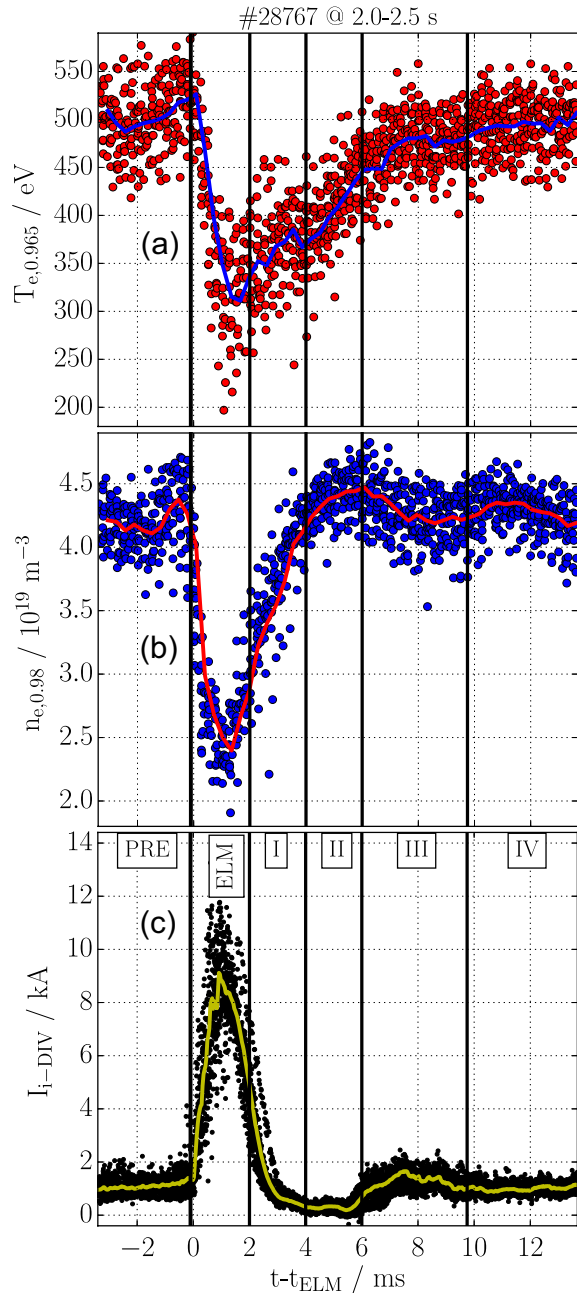


Figure 5.2.: ELM synchronized data points of (a) the electron temperature T_e and (b) density n_e at the pedestal top ($\rho = 0.965$ and $\rho = 0.98$) evaluated with IDA and (c) the inner divertor shunt current as a measure for the transport over the separatrix together with the smoothed signal of all quantities.

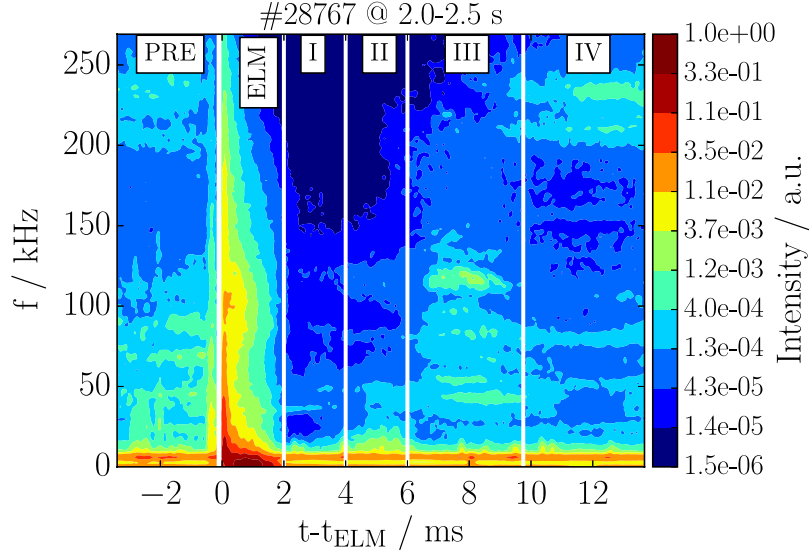


Figure 5.3.: ELM synchronized frequency spectrum measured from the toroidal magnetic pick-up coil array. Six distinct phases during the ELM cycle are characterized by the appearance of modes with different frequencies.

by *Laggner et al.* [107] that the gradients of both quantities electron temperature and density are clamped during this phase. This phase mainly determines the length of the ELM cycle. It lasts until the ELM crash and is therefore similar to the pre-ELM phase.

This last phase before the ELM crash, or pre-ELM phase (PRE), includes a last slight increase of density and temperature and ends with the ELM crash.

The ELM crash phase (ELM) is defined by strong losses of temperature and density which take place on a millisecond time scale. It is important to mention that in the here defined phase already the density and temperature recovery starts. Nevertheless, the divertor shunt current signal is still high also at the end of this phase representing either a high transport of particles or high recycling rates in the divertor region.

All these phases are slightly overlapping with each other and it is not easy to exactly determine an exact boundary. The phases defined here are a result of 25 averaged events which look different in detail. Nevertheless, the profile recovery after each ELM is very similar up to 12 ms after the ELM onset and the starting point of each phase varies only by about 0.5 ms for all 25 ELMs, which makes the ELM synchronization for the pedestal parameters a useful tool.

In the following the ELM synchronization of magnetic fluctuations is discussed. The synchronization of magnetic signals is done in the Fourier space to resolve participating frequencies and thereby different modes. Figure 5.3 shows an ELM synchronized frequency

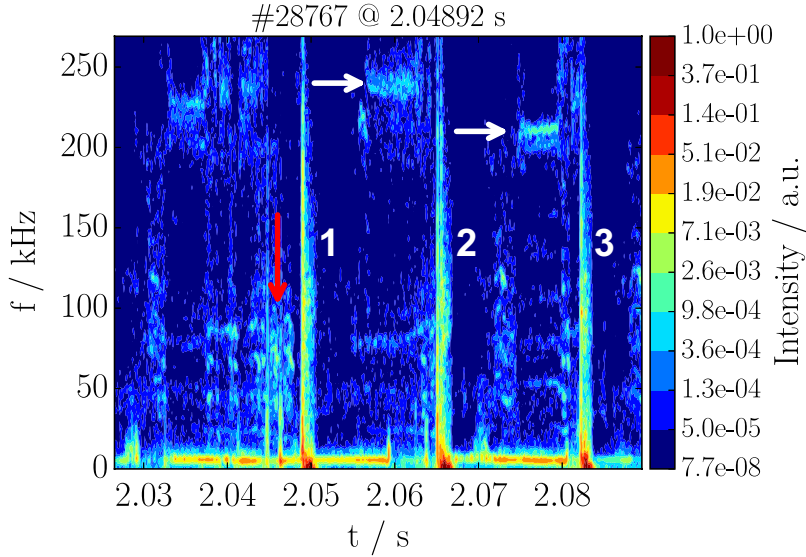


Figure 5.4.: Frequency spectrum of three single ELM events. The red arrow marks magnetic activity before the first ELM. White arrows mark different high frequency pre-ELM fluctuations at 240 kHz and 210 kHz before second and third ELM respectively.

spectrum. It is similar to the previously explained frequency spectra with the difference that each time window with respect to one ELM crash is evaluated by a Fourier analysis for all coils of the toroidal array and the amplitudes are summed for all ELMs and normalized to the maximum intensity. The windows have a distance of $25 \mu\text{s}$ and a length of 1 ms which creates an overlap of the time windows. The intensity of each participating frequency is again given by the Fourier coefficients of each time window. The resulting ELM synchronized frequency spectrum is an indicator for the probability of different coherent signals with certain frequencies to appear during the whole time trace with respect to the ELMs.

In the ELM synchronized spectrum of the present discharge, see figure 5.3, one can differentiate phases by the appearance of different characteristic frequency bands which indicate the existence of modes. These phases are again the pre-ELM phase with two distinct frequency regions of increased mode activity at 0–100 and 200–250 kHz, the ELM crash phase with strong broadly spread but low frequency dominated magnetic activity, and the time after the ELM. One can identify the same four sub-phases after the ELM crash as in figure 5.2, which are now characterized by their different magnetic activity. Phase (I) shows only weak magnetic activity besides the core MHD mode at 0–18 kHz. Phase (II) has magnetic activity in the frequency range up to 50 kHz and weaker activity at higher frequencies. Phase (III) has dominant magnetic activity in the frequency

range up to 150 kHz and phase (IV) includes dominant modes in the frequency range of 200–250 kHz.

The ELM synchronized spectrum contains little information about the mode structure that appears before or after one single ELM. This is shown in the spectrum of three single ELM events, figure 5.4. Similar frequency bands as in the ELM synchronized spectrum appear, but not all of them appear together like the ELM synchronized spectrum could suggest. The first ELM has much more pre-ELM activity below 100 kHz (red arrow). The second and third ELMs have slightly different high frequency pre-ELM fluctuations at 240 and 210 kHz respectively (white arrows). Therefore the ELM synchronized spectrum can only be used to detect prevalent features but for conclusions on the connection of modes to ELMs a single ELM analysis is always needed. This will also be discussed in detail for the most critical pre-ELM phase.

The onset of different phases correlates with changes in the previously discussed kinetic profiles, see figure 5.2. A toroidal mode number determination of phenomena during the ELM cycle was performed for all the phases separately. Therefore, time windows with the length of 2.0 ms were chosen and analyzed in the following.

The most intense coherent magnetic signal throughout the ELM cycle in this discharge is produced by an $n = +1$ core mode at frequency $f_{\text{core1}} = 6.5 \pm 2$ kHz and its $n = +2$ harmonic at $f_{\text{core2}} = 13 \pm 4$ kHz rotating in co-current direction. In the following discussion this core mode will be omitted if not explicitly mentioned. All other coherent magnetic features are propagating in the electron diamagnetic direction, evolve during the ELM cycle, and cause the frequency bands that are visible in figure 5.3. These oscillations between ELM crashes are phase-wise investigated in terms of toroidal mode number n in the next paragraphs. A poloidal mode number determination and thereby a position determination is presented for phase III together with other position determination techniques afterwards.

5.1.1. Phase I

The contour plot in figure 5.5 (a) shows an ELM synchronized frequency and toroidal mode number spectrum (f - n spectrum). It is similar to the previously mentioned f - n spectra. The only difference is that here the not normalized f - n spectra of all 25 2 ms time windows around 3.0 ms after an ELM crash in the time between 2.0 and 2.5 seconds of the discharge are summed and normalized to the maximum intensity. Also plotted are the mode number spectra obtained by integration over all frequencies (b) and over all frequencies higher than 18 kHz (c). By integrating over frequencies higher than 18 kHz the contribution to the spectrum of the core mode is suppressed.

Post-ELM phase I exhibits almost no magnetic activity besides the core mode at $n = 1$ and $f_{\text{core1}} = 6.5$ kHz in figure 5.5 (a) and (b). This is the phase where the edge temperature and density gradients are crashed so that there is no drive for strong mode activity in the edge, see figure 5.2. The only other magnetic activity is a weak coherent $n = 0$ structure with frequencies $f = 100$ – 160 kHz together with some noise, see figure 5.5 (c). As this $n = 0$ structure also appears in phase II and much more intense in the ELM phase itself it will be discussed later.

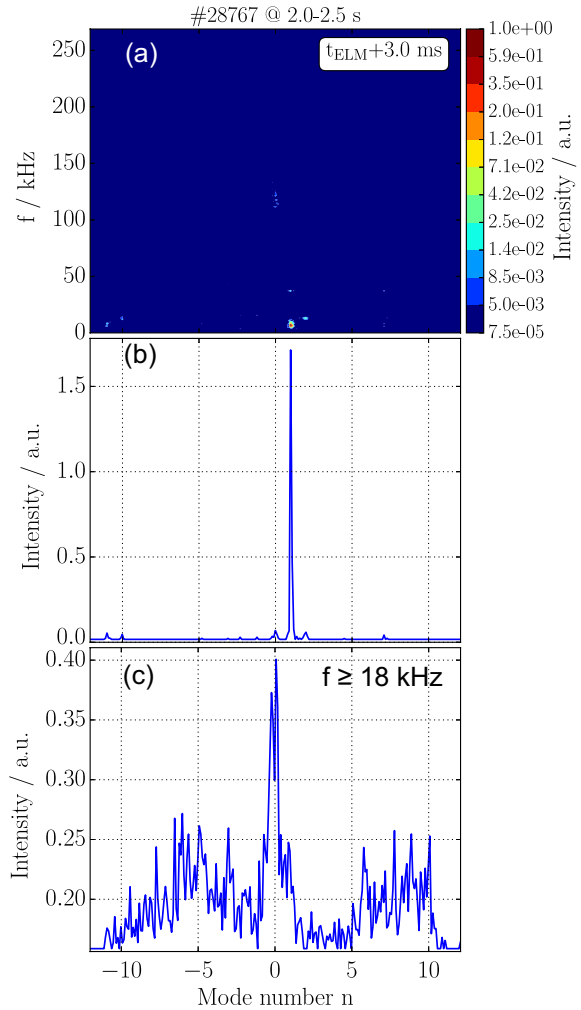


Figure 5.5.: Phase I: (a) ELM synchronized f - n spectrum and n spectrum from integration (b) over all frequencies and (c) over frequencies above 18 kHz of the 25 time windows around 3.0 ms after the ELMs.

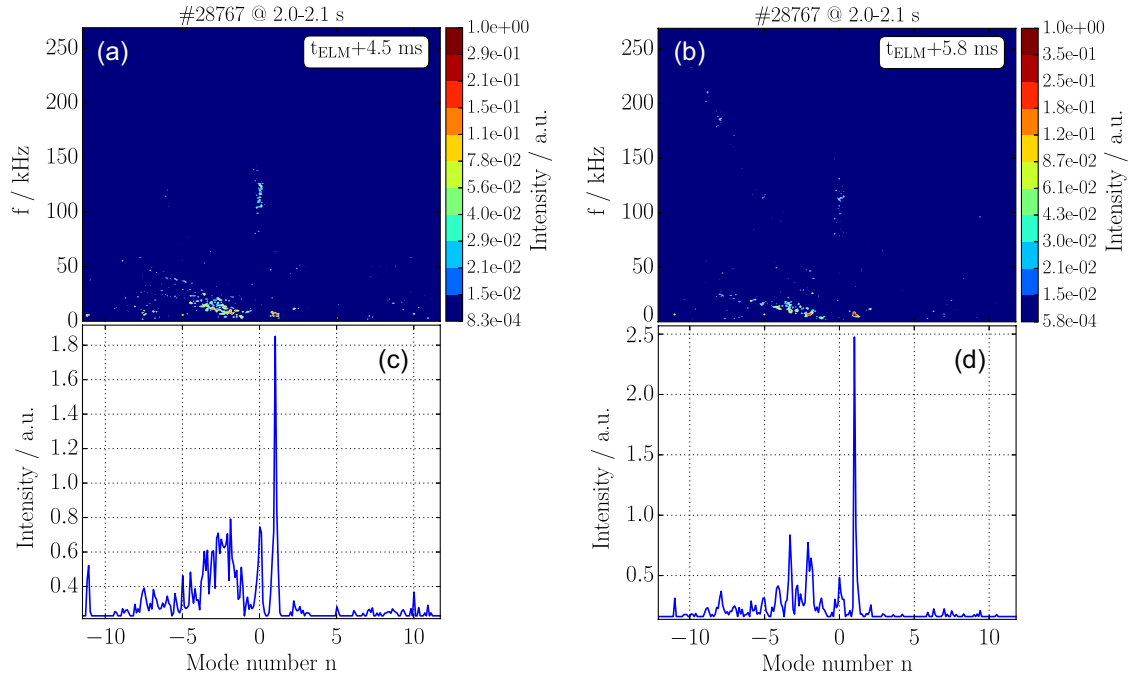


Figure 5.6.: Phase II: (a),(b) ELM synchronized f - n spectra and (c),(d) n spectra of the five time windows around 4.5 ms and 5.8 ms respectively after the five ELMs between 2.0-2.1 s.

5.1.2. Phase II

Figure 5.6 shows mode number spectra for two time windows during phase (II). They include only the five ELMs during 2.0–2.1 s of the discharge in order to reduce smearing of mode numbers. In this phase low frequency magnetic activity with not clearly defined negative mode numbers, see figures 5.6 (a) and (c), evolves into distinct modes in the range of $n = -(1-8)$, see figures 5.6 (b) and (d). The transition time varies by about 0.5 ms from ELM to ELM. This leads to a blur of both structures if evaluated for all 25 ELMs.

Together with the low frequency fluctuation again an $n = 0$ structure is visible in both time frames. Also a weak branch of mode numbers at high frequencies with $n = -7, -8$ ($f \approx 180, 210$ kHz) begins to form at the end of this phase and will evolve towards $n = -5$ and become dominant in phase (III). Even in a single ELM analysis both low and high frequency branches coexist at the end of this phase on the millisecond time scale given by the evaluated window length.

At the end of this phase the temperature at the pedestal top is still low whereas the density reaches its maximum. This is the time point of the formation of the discrete high and low frequency structure which goes hand in hand with the transport increase in figure 5.2 at

about 6 ms. As the rotation of the plasma in the edge is mainly given by $\nabla p_i / B n_e$ and ion temperature restores similarly as density, the rotation profile is from this point on restored and almost fixed [110]. Therefore, frequencies of modes will mainly change due to a change of mode numbers and not because of a variation of rotation.

5.1.3. Phase III

In phase III around 7.5 ms after the ELM crash three clear branches of modes are present. The onset of these modes coincides with an increased transport, inferred from an increase in the divertor shunt current signal, and a small drop in the pedestal density, see figure 5.2. The branches form three different straight lines in the f - n spectrum, figure 5.7 (a), with very sharply defined mode numbers in the n spectrum, figure 5.7 (b). All branches coexist on the 2 ms time scale and are not a result of the ELM synchronization which can be validated by single ELM analysis. The different slopes of the mode branches indicate again their different rotation velocities. Therefore the first branch (white dashed line) with mode numbers $n = -(1-7)$ with frequencies $f = 15-80$ kHz rotates with a comparatively low velocity, whereas the second (green dashed line) and most dominant branch ($n = -(1-9)$, $f = 15-200$ kHz) and the third (red dashed line) branch ($n = -8$, $f = 220$ kHz) have higher ones. These velocities will later be used for a rough estimation of the localization of the modes. This estimation is independent of any poloidal mode number determination, which will be discussed for the same case. As already mentioned the second branch starts with $n = -7, -8$ already in phase II whereas the other branches show up in this phase for the first time.

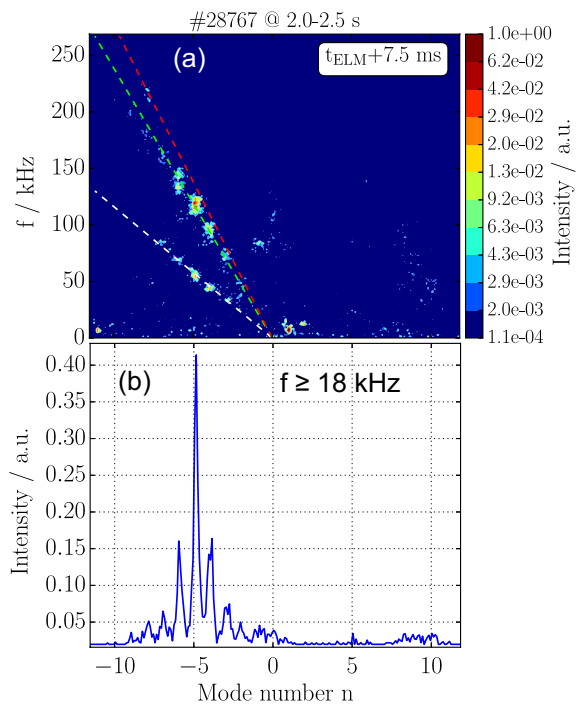


Figure 5.7.: Phase III: (a) ELM synchronized f - n spectrum and (b) n spectrum obtained from integration over frequencies above 18 kHz of the 25 time windows around 7.5 ms after the ELMs. Red, green and white dashed lines indicate mode branches with different f/n values.

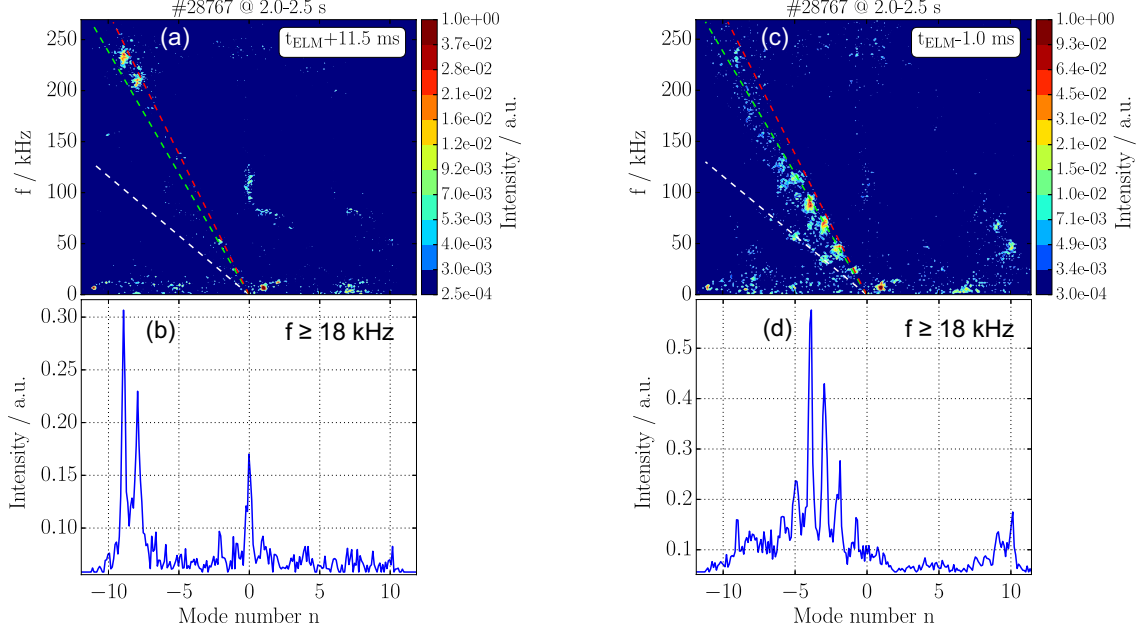


Figure 5.8.: Phase IV and pre-ELM phase: (a,c) ELM synchronized f - n spectra and (b,d) n spectra obtained from integration over frequencies above 18 kHz of the 25 time windows around (left) 11.5 ms after and (right) 1.0 ms before the ELMs. Red, green and white dashed lines have the same slopes as in figure 5.7 (a).

5.1.4. Phase IV

In phase IV around 11.5 ms after the ELM crash a transition from dominant medium to higher frequencies ($f = 200$ – 250 kHz) is observed, see figure 5.3.

The most dominant mode numbers during this phase are $n = -8, -9$, see figure 5.8 (a,b). In the f - n spectrum of this phase again the dashed lines with the same slope, i.e. same rotation velocity, as in phase III are included. No activity is found along the white dashed line whereas the dominant $n = -8, -9$ and also some weaker $n = -2$ still almost follow the previously defined red and green dashed lines. This shows that the measured frequency, given by equation 4.2, changes mostly due to a transition in dominant modes whereas rotation velocity is not changing very much from phase III onward. The onset of these $n = -8, -9$ modes coincides with the saturation of the electron temperature, a slight drop down of the pedestal density and the establishment of a transport equilibrium, see figure 5.2. As this phase has a stronger pressure gradient and the mode numbers are higher than in phase III it might be that these modes are more pressure driven than the dominant ones in phase III.

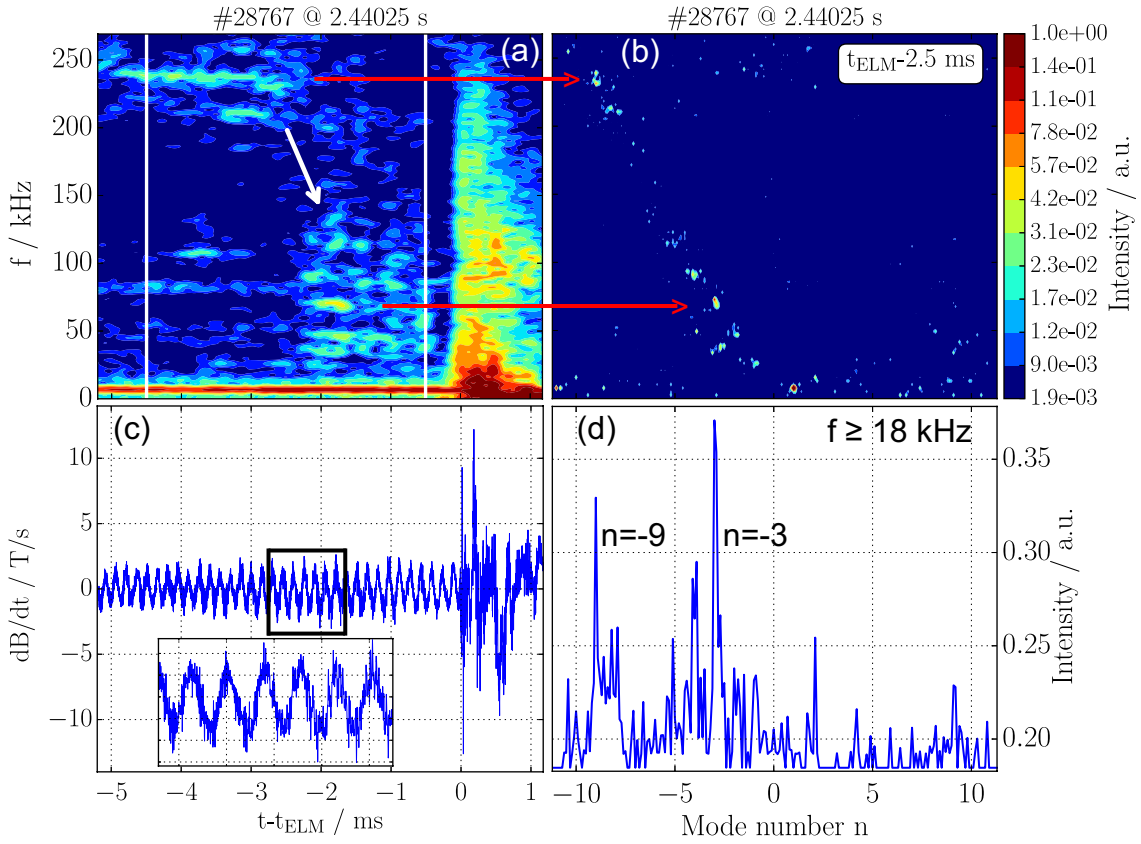


Figure 5.9.: (a) Spectrum relative to one single characteristic ELM at 2.44 s. The jump from high to low frequencies in the evaluated frame (marked with white stripes) is illustrated by the white arrow. (b) f - n spectrum and (d) n spectrum obtained from integration over frequencies above 18 kHz of a 4 ms time window around 2.5 ms before the ELM. (c) The magnetic raw signal of the analyzed time frame together with a zoom around 2.2 ms before the ELM.

5.1.5. Pre-ELM Phase

In the pre-ELM phase around 1.0 ms before the ELM crash the same modes as for the phases III and IV are present with similar rotation velocities, but most dominant mode numbers decrease to $n = -2, -3, -4$, which is visible in the ELM synchronized f - n spectrum in figure 5.8 (c). Such a jump of mode numbers and therefore frequencies takes place just before the ELM crash. To see this mechanism more clearly one characteristic ELM was chosen from the time trace and analyzed. Spectra of this single ELM are shown in figure 5.9 together with the magnetic raw signal. From the frequency spectrum it is visible that the

transition from higher to lower frequency takes place roughly 2.2 ms before the ELM and that the transition is such that the high frequencies stop abruptly and the 30–120 kHz fluctuations appear again. This is also visible in the zoomed part of the magnetic raw signal, where high frequency oscillations disappear around -2.2 ms. This effect of the jump of mode numbers before the ELM onset is for almost all ELMs in the whole time trace very pronounced. For a few cases mode numbers even jump back and forth ending with lower frequencies before the ELM. Only broadband activities (like before the first ELM in figure 5.4) can blur this effect. The n spectra are calculated for a 4.0 ms time window around 2.5 ms before the ELM crash to calculate mode numbers for both the high frequency and the low frequency domain. From the f - n spectrum it can be seen that the lower frequencies just before the ELM onset are not caused by a slowing down and therefore a decrease of the velocity but a jump in the mode numbers. In this case the dominant mode numbers go from $n = -9$ to $n = -3$. These results of a fast transition from high to low n are seen by the nonlinear MHD code JOREK as well, but usually only in the ELM crash phase, when modes grow exponentially [111, 112].

5.1.6. ELM Phase

The ELM phase is defined here as the 2 ms long phase starting at the ELM crash. The f - n spectrum in figure 5.10 shows that the dominant structure during this phase is continuous with negative n with frequencies less than 25 kHz. The structure peaks around $n = -3$, similar to the one in phase II after the crash. Although the structure does not occur with single isolated peaks in the n spectrum, it is clear that it is still coherent. The exact structure cannot be obtained for this discharge, neither from the ELM synchronized nor from single ELM calculations, because of the very short time intervals and the high noise. Nevertheless, it must be pointed out that this structure looks very much like the one that appears just before the ELM crash in the pre-ELM phase with dominant mode numbers $n = -(2-5)$ but smeared out due to the fast changes. Furthermore, the structure appears with strongly decreased velocity, which is mainly due to the radial electric field collapse during ELMs [113]. Further analysis of more recent data, evaluated with the extended toroidal array showed indeed that the ELM crash seems to conserve the structure of the modes visible before, which is presented in detail in the next chapters.

In addition to the continuous negative n , mode numbers around 80–130 kHz are visible which still exist in the phases I and II after the ELM. In the mode number spectrum including only frequencies higher than 50 kHz, see figure 5.10 (c), it is visible that mode numbers of this structure are $n = 0$ and $n = \pm 6$. It is not completely understood how to interpret these results. In order to explain this phenomenon, signals with an $n = -6$ and a broad frequency

spectrum were generated and evaluated with the same linear fitting algorithm considering the given geometry of the coils. These simulated $n = -6$ mode showed always weaker artifacts at $n = +6$ and $n = 0$. On the other hand a pure $n = 0$ mode structure was generated and it did not show any other structure besides $n = 0$ also when adding a high level of noise. In addition to the investigation of artificial modes a second evaluation of this phase with dropping one coil in the analysis and therefore changing the geometric arrangement was done. This evaluation still resulted in an $n = 0$ together with $n = -6$ but it changed the dominant positive mode numbers, which suggests that the positive value is an artifact. Therefore the interpretation points into the direction that there exists some structure with a mode number $n = -6$ and the dominant $n = 0$ structure while no structure rotating in the ion diamagnetic direction exists.

The broad spread in frequency is thought to be caused by a movement of the structure perpendicular to the field lines towards the B_r -coils, first of all by the movement itself and secondly because the structure crosses regions with different plasma rotation velocities yielding also different frequencies.

The origin of the mode with $n = 0$ and -6 stays unexplained. It might be that the strong nonlinear interaction during the crash triggers a mode, e.g. a GAM with $n = 0$, which would mean that the $n = -6$ is artificial. However, the frequency of a common geodesic acoustic mode is typically lower and only the $n = 0, m \neq 0$ branch called the geodesic Alfvénic mode fits to frequencies around 100 kHz [114]. Another explanation would be that the strong exhaust during the crash causes a shaking of the plasma, which could also appear as an $n = 0$ fluctuation. Another possible explanation would be the often described filaments that appear at the end of ELMs. Usually they are assumed as current carrying [115] field aligned structures which propagate in the scrape-off layer towards the B_r coils [116, 117]. This fits to the here detected broad spread in frequencies and to the appearance of a

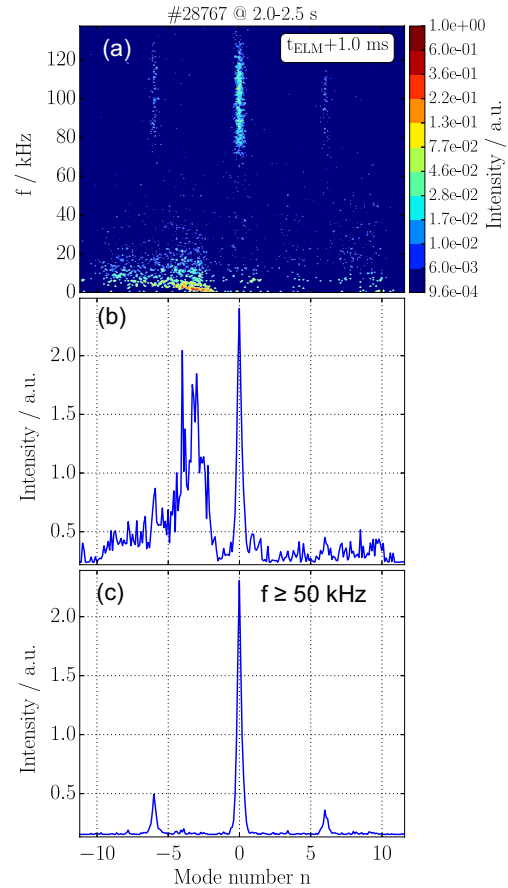


Figure 5.10.: ELM phase: (a) ELM synchronized f - n spectrum and (b) n spectrum obtained from integration over all frequencies and (c) over frequencies above 50 kHz of the 25 time windows around 1.0 ms after the ELMs.

nonzero toroidal structure. However, they usually propagate in ion diamagnetic direction in the scrape off layer, which does not fit to the negative $n = -6$.

5.2. Radial Position of Modes in the ELM Cycle

In order to further characterize the modes appearing in the ELM cycle the next step is to radially localize them. From the localization and the kinetic profiles one could determine the main drive of the mode on the one hand. On the other hand the velocity of the mode at that position can be compared to the plasma rotation and therefore the phase velocity of the mode could be identified, which is again characteristic for the type of the mode. There are various possibilities of localizing the modes. One approach is to calculate also the poloidal mode number m . Together with the assumption that $q = m/n$, modes can be localized if an equilibrium is well known. A second approach would be to compare the velocity with which they pass the pick-up coils to the plasma velocity measured by CXRS, which might even deliver the phase velocity of the modes. A last approach is to consider radially localized diagnostics such as ECE, the Li-beam or a reflectometer. This approach can only work if the quantities measured by these diagnostics are oscillating similarly as the magnetic properties of the modes. All these three approaches are explained in the following and positions of the modes that appear during phases III and IV of the previously shown ELM cycle are calculated. Other phases like the crash itself are not stationary enough for calculating any position as for example the equilibrium has high uncertainties.

5.2.1. Position from Velocity Estimation

As it was shown by *Laggner et al.* [107] the here discussed modes appearing between ELM crashes are located somewhere in the strong pressure gradient region close to the plasma boundary. Some of the following assumptions used for a more precise localization are only valid in this edge region. The mode velocity perpendicular to the magnetic field in the laboratory frame is given by the sum of $E \times B$ velocity and its intrinsic phase velocity¹:

$$\vec{v}_{\perp, \text{mode}} = \vec{v}_{E \times B} + \vec{v}_{ph}. \quad (5.1)$$

The measured frequency of the mode is given by the mode velocities and the toroidal and poloidal wavelength, see equations 4.1 and 4.2:

¹The intrinsic or phase velocity is the velocity with which a mode rotates relative to the plasma frame. It is characteristic for each type of mode or coherent phenomenon [118].

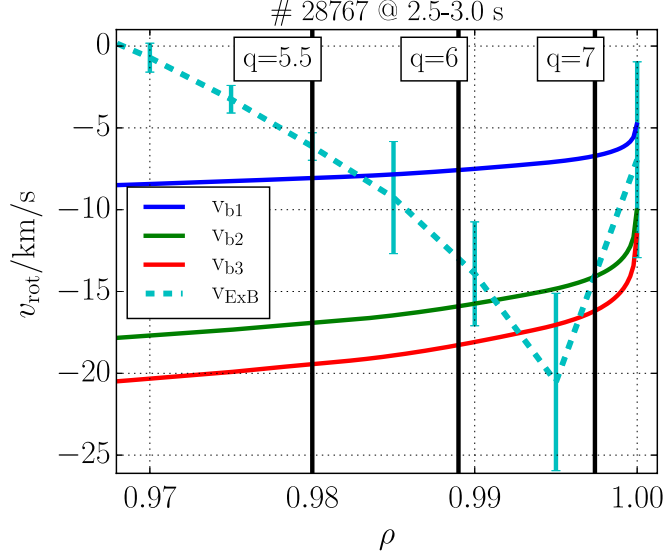


Figure 5.11.: Comparison of the velocities of the three mode branches appearing around 7.5 ms after the ELM crash of the previously described discharge and $v_{E \times B}$ measured by CXRS.

$$f = \frac{\vec{v}_{\perp, \text{mode}}}{\lambda_{\perp}} = \vec{v}_{\perp, \text{mode}} \sqrt{\left(\frac{n}{U_{\phi}}\right)^2 + \left(\frac{m}{U_{\theta^*}}\right)^2} \approx \vec{v}_{\perp, \text{mode}} \frac{m}{U_{\theta^*}} \quad (5.2)$$

with m, n and U_{θ^*}, U_{ϕ} the poloidal and toroidal mode numbers and circumferences. The toroidal term is negligible compared to the poloidal term at the edge, as m is in the order of $m = q_{\text{edge}} n \approx 5n$ and the toroidal circumference is much larger than the poloidal. This equation describes a straight line through the origin in the f/n plane under the assumption that $q = m/n$. In case modes are not on rational surfaces, e.g. $m = qn + \Delta m$, the frequency would have an offset

$$f = \frac{\vec{v}_{\perp, \text{mode}}}{U_{\theta^*}} (qn + \Delta m) \quad (5.3)$$

Therefore, the previously described mode branches forming straight lines through the origin of the f/n plane also show how precisely the modes are on rational surfaces. Assuming a mode is close to the plasma edge and placed on a rational surface $q = m/n$ its velocity can be determined from the measured frequency via $v_{\perp, \text{mode}} = U_{\theta^*} \frac{f}{qn}$, where the poloidal circumference can be obtained from the equilibrium.

The phase velocity can now be calculated from the mode velocity, given by the measured f/n values and the $E \times B$ velocity $v_{E \times B}(\rho) = \frac{\vec{E}(\rho) \times \vec{B}(\rho)}{B(\rho)^2}$ via equations 5.1 and 5.3, where the radial electric field E is measured with the charge exchange recombination spectroscopy

(CXRS) diagnostic, see chapter 3.6. Conversely, the mode can be localized with this equation if the phase velocity is known.

Figure 5.11 shows the comparison of both quantities, the mode velocity $v_{\perp, \text{mode}}$ and $v_{E \times B}$, depending on ρ_{pol} together with the position of the rational surfaces $q = 5.5, 6, 7$ for the previously analyzed discharge. For this comparison mode velocities of the three dominant branches with indices b1, b2, b3 appearing in phase III with values of $f/n \approx -11.2, -23.5$ and -27 kHz were chosen. These values are given by the slopes of the dashed lines in figure 5.7. From this velocity comparison different radial positions of the modes are possible. If the modes do not have any phase velocity (e.g. ideal peeling mode) they would be localized at the position where the mode velocity and $v_{E \times B}$ coincide. Within the measurement uncertainties of \vec{E} this could be the case for the faster branches at $q \geq 6$. For the slowest branch either at $q = 5.5-6.0$ or very close to the separatrix ($\rho = 1.0$) both velocities coincide.

If the phase velocities of the modes would be in the ion diamagnetic direction, $v_{ph} > 0$ (e.g. kinetic ballooning modes), the mode velocity would lie above $v_{E \times B}$. As the absolute values of diamagnetic and $E \times B$ velocities are almost the same near the $E \times B$ minimum [24], both quantities should even compensate and the mode velocity would vanish. Only the slowest mode branch shows in the region of the $v_{E \times B}$ minimum a strong positive offset which might be a possible location of modes with ion diamagnetic velocity. Furthermore, such modes can also not be excluded from the region very close to the separatrix due to the big velocity uncertainties there.

If the phase velocities of the modes would be in the electron diamagnetic direction, $v_{ph} < 0$ (e.g. micro tearing modes), the mode velocity would lie below $v_{E \times B}$ in figure 5.11. This is either the case at $q < 6$ or again very close to the separatrix, where uncertainties of $v_{E \times B}$ are so large that it is not possible to make a quantitative statement.

From this analysis the mode rotation velocity fits to the $E \times B$ velocity close to the maximum pressure gradient. However, it is not possible to determine an exact position or the exact phase velocity due to the uncertainties in the measurement of the radial electric field. Therefore, an analysis of the poloidal mode number m is necessary to clarify the $q = m/n$ position.

5.2.2. Position from m/n Determination

As previously mentioned the m determination is one possible tool for the localization of modes. The main drawback is that it relies on the assumption that $q = m/n$ and a precise equilibrium. For modes that are not placed on rational surfaces, the conversion of $\theta \rightarrow \theta^*$ cannot be done self-consistently.

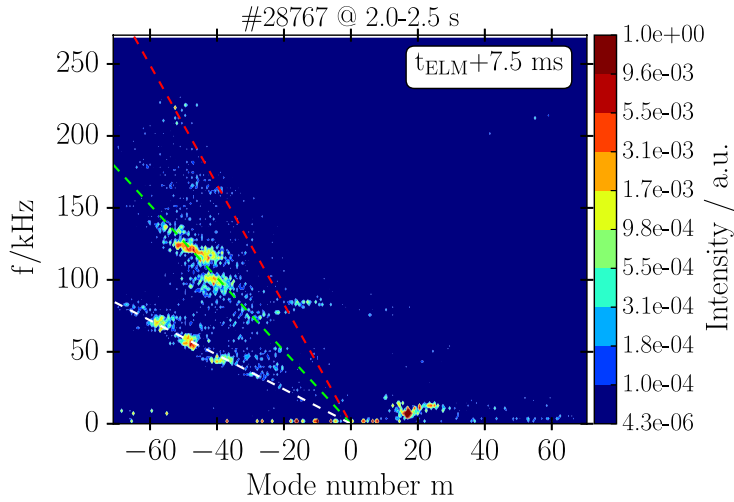


Figure 5.12.: ELM synchronized f - m spectrum of the 25 time windows around 7.5 ms after the ELMs. Red, green and white dashed lines indicate the mode branches with different f/m values, similar to Figure 5.7.

Figure 5.12 shows, analogously to Figure 5.7 for the n values, the poloidal mode number and frequency spectrum (f - m spectrum) appearing in phase III of the previously investigated ELM cycle. Here the intensities of the modes are taken from the poloidal array of pick-up coils and are therefore slightly different than the one from the toroidal array (used for the n determination). The equilibrium was taken at $\rho = 0.995$, equivalent to $q = 6.5$. According to the equilibrium the $d\theta^*/d\theta$ does not vary a lot for $q \geq 6.5$, therefore the same $\theta \rightarrow \theta^*$ conversion is also valid for mode positions further outwards. Similarly to the n determination, white, green and red dashed lines mark the three branches that appear at this time point of the ELM cycle. The slowest branch (white) has dominant poloidal mode numbers of $m \approx -39, -48$ and -58 . The corresponding n values are $n = -4, -5$ and -6 . This branch lines up on a straight line through the origin. On the one hand the straight line represents the precision of the phase fit. On the other hand the range $q = 9.5-10$ lies only within a mm wide region close to the separatrix. Such widths are comparable to the ion Larmor radius of about 1 mm, being a lower size limit for coherent phenomena in the typically used MHD framework [119]. Furthermore, as poloidal mode numbers are overestimated by trend, see section 4.3, this result might be questionable.

The most dominant branch is very broad in m . The slopes vary strongly dependent on which mode number m is considered to be true. For the most dominant $n = 5$ the m values are $m = -(38-53)$, with something like two dominant mode numbers of $m = -42$

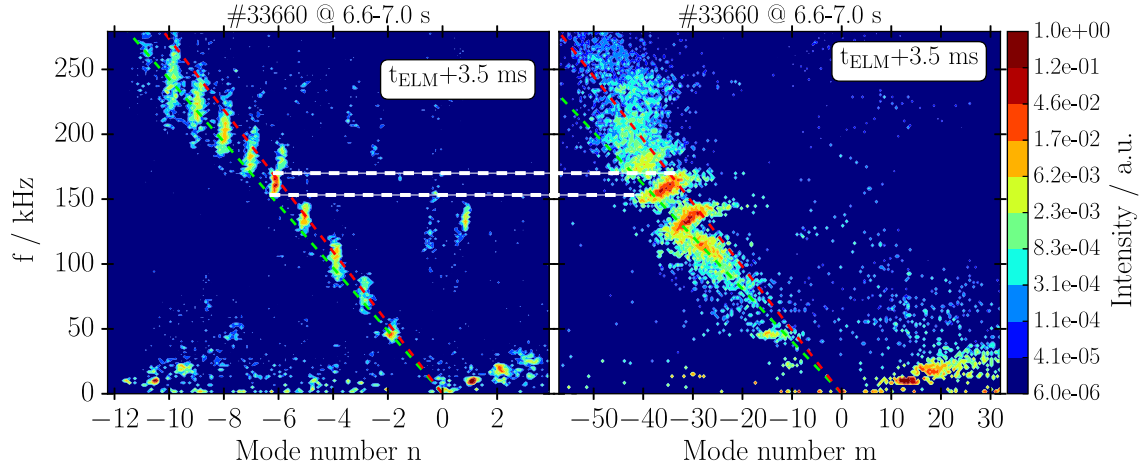


Figure 5.13.: ELM synchronized spectra for toroidal and poloidal mode number of the 20 time windows around 3.5 ms after the ELMs. Red and green dashed lines indicate the mode branches with different f/m values. The white dashed line indicates the range of m that is covered by the $n = 6$ mode.

and $m = -48$ between 110 and 130 kHz. This would be equivalent to $q = 8-10$. Similarly to the slow branch these values are formed within a few mm from the separatrix. The fastest branch has the dominant poloidal mode number of $m \approx 52$ at $f = 220$ kHz. This fits perfectly to the $n = 8$, $q = 6.5$, which is also the position where the equilibrium was taken from.

Another discharge with much lower $q_{95} = 3.0$ was investigated in order to check whether the q determination gives conclusive results here as well. Figure 5.13 shows n and m spectra for a similar phase of the ELM cycle for this low q discharge. The equilibrium was obtained from $q = 5$, which is at $\rho = 0.999$. Here the different mode branches in the n plot are not separated. It is not clear which mode number belongs to the faster branch and which to the slower one. However, in the m plot the modes with the same n number have deviating m and two branches are more separated. In this case the $n = 6$, marked with white dashed lines, spreads from $m = 30$ to $m = 40$, which would be equivalent to $q = 5-6.5$. Again the mode numbers with lower velocity (lower f) appear with higher m values and are therefore located further outwards.

All in all this method delivers m values of edge phenomena, that are consistent with the q positions. However, the interpretation depends on the $q = m/n$ assumption and a precise knowledge of the equilibrium. Due to the fact that the equilibrium always needs to be taken at very edge values $q > 5$, results are also questionable as the space there is on ion Larmor radius scales. An alternative interpretation might be that either m is

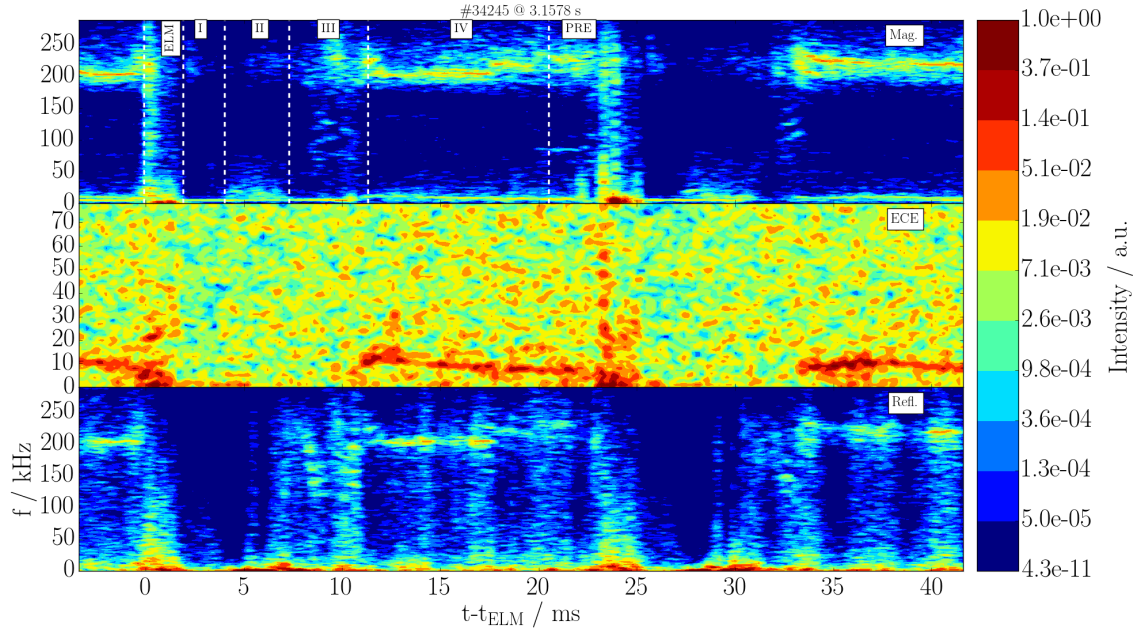


Figure 5.14.: Spectra calculated from a magnetic pick-up coil, the ECE channel 14 close to the pedestal top and the HFS reflectometer with incident frequency $f = 48$ GHz.

overestimated slightly or that $m > qn$, though unlikely as the mode branches do not appear with an offset in the f/n plane. However, the statement that low velocity branches tend to have higher m and are therefore further outwards seems to be robust and valid for various q profiles.

Taking the results of the poloidal mode number determination for granted, the fastest branch of the here investigate phase III of the ELM cycle is located in the $E \times B$ minimum, whereas slower branches are located even further outwards. In this case the phase velocity of the fast branch would be zero and modes might be associated with ideal ballooning or ideal peeling modes. Because of the high uncertainties in the $E \times B$ velocity close to the separatrix, the phase velocity cannot be clarified for lower velocity modes.

5.2.3. Position from Radially Localized Diagnostics

Figure 5.14 separately shows normalized spectra calculated from magnetic pick-up coil, ECE and reflectometer data during one AUG ELM cycle. Also for this discharge the previously defined phases of the ELM cycle are clearly visible in the magnetic spectrum

(top), although medium frequency fluctuations of phase III are less pronounced². The mid plot shows the spectrum taken from one ECE channel close to the pedestal top³. The ECE channel also detects a broad spread in frequency and a strong intensity increase during the ELM crash. Furthermore, a strong oscillation around 7–10 kHz is visible in phase III and dominantly in phase IV. It is temporally correlated with the appearance of the high frequency fluctuations in the magnetic pick-up coils. Channels further outwards up to the separatrix show a similar behavior, which is maybe due to the shine through effect [80]. The last spectrum is taken from a 48 GHz (equivalent to a density of $n_e = 2.8 \cdot 10^{19} \text{ m}^{-3}$) channel of a reflectometer on the HFS of the plasma. According to the density profile obtained from the LFS, the measurement position at $\rho = 0.985$ is slightly more inwards than the maximum of the $E \times B$ velocity. Nevertheless, the HFS density profiles are by trend steeper than LFS profiles [89] and thereby the measurement position might be further outside. Clearly visible are here also the high frequency fluctuations of phase IV. At the same time when the medium frequency fluctuations appear in the magnetics of phase III, also the fluctuations in the region of 100–200 kHz become stronger. Reflectometer measurements at 37 GHz show a similar behavior also at $\rho = 0.995$. Reflectometry measurements obtained with similar frequencies on the LFS do not see any coherent fluctuations either due to the strong noise level on the LFS or due to a different measurement position.

From these measurements it can be concluded that high frequency fluctuations during the ELM cycle are located in the strong gradient region. An exact position determination is again not possible as there might be a profile asymmetry between LFS and HFS. Furthermore, the fluctuations seen in ECE might be localized further inwards and strongly correlated with high frequency fluctuations in the magnetics, but not of the same nature as they appear in a very different frequency regime. It was suggested that these fluctuations are density fluctuations at the pedestal top, which is supported by Li-beam data [120]. Their connection to magnetic high frequency fluctuations remains an open question.

After this discussion of the radial localization, one also could ask the question whether such modes appear symmetrically on both sides of the plasma or whether they are stronger on any specific poloidal position, which is also an important property of modes. This question is tackled in the next section.

²The previously discussed discharge is not suitable for this localization method as it lacks reflectometry measurements. However, basic parameters such as heating, fueling and q profile are very similar.

³The ECE spectrum is only plotted up to 75 kHz, as higher frequencies are just governed by noise.

5.3. Poloidal Position of ELM Cycle Modes

Ballooning modes are by definition poloidally asymmetric. From the basic one fluid MHD picture the strongest amplitude of such modes is expected to appear in the bad curvature region of the plasma, i.e. the low field side. Although more advanced models propose also shifts of the maximum amplitude due to velocity shear [121], a comparison of pick-up coils from LFS and HFS should be enough for the purpose here. Figure 5.15 shows spectra during the same ELM cycle as for the radial localization, figure 5.14. Spectra are taken from magnetic pick-up coils that are installed on HFS and LFS and measuring poloidal and radial magnetic field components \dot{B}_θ and \dot{B}_r . Fluctuations of the poloidal magnetic field are a result of current fluctuations along the field lines, whereas the radial coils are measuring a displacement of the plasma column. The spectra are normalized to the overall maximum. Thereby comparisons between LFS and HFS coils of the same type are possible. Nevertheless surrounding structures and distances from the coils to the plasma are varying strongly between HFS and LFS, which makes the comparison only qualitatively but not quantitatively suited. However, the temporal behavior within one coil can be compared to the behavior of others in order to draw a qualitative statement. From the figure it can be seen that the medium frequency fluctuations of phase III at around $t - t_{\text{ELM}} = 10$ ms and the pre-ELM phase at around $t - t_{\text{ELM}} = 20$ ms are visible in all coils. However, a strong increase of the frequency bands below 100 kHz slightly before the next ELM is only observed on the low field side (marked with red arrows). Similarly, the high frequency fluctuations in the range 200–250 kHz are visible in all coils, but in the LFS B_r coils an increase of frequency before the ELM is connected with a decrease of intensity, whereas intensities rise in all other cases, especially in the HFS B_r (marked with white arrows). From these figure one might conclude that the low frequency modes that become stronger on the LFS before the ELM are more ballooned and thereby mainly pressure driven. On the other hand the pedestal clamping high frequency modes might get into a state of similar amplitude on LFS and HFS before the ELM crash indicating that they become more current driven and more symmetric at that point. Thereby the here shown cycle might be interpreted in the following way: As soon as the pedestal pressure gradient is strong enough to drive ballooning modes, the high frequency modes set it. They create enough transport for clamping the gradient but the pedestal might rise further and become wider. At a certain point the bootstrap current is strong enough and thereby modes become more current driven. Nevertheless, these modes cannot create enough transport which is why pedestal gradient steepens or broadens slightly and thereby enables bigger, i.e. lower n , ballooning modes, forming the ELM crash. As the low n create high transport the $E \times B$ velocity drops. Thereby the stabilizing shear drops, enabling further growth and further

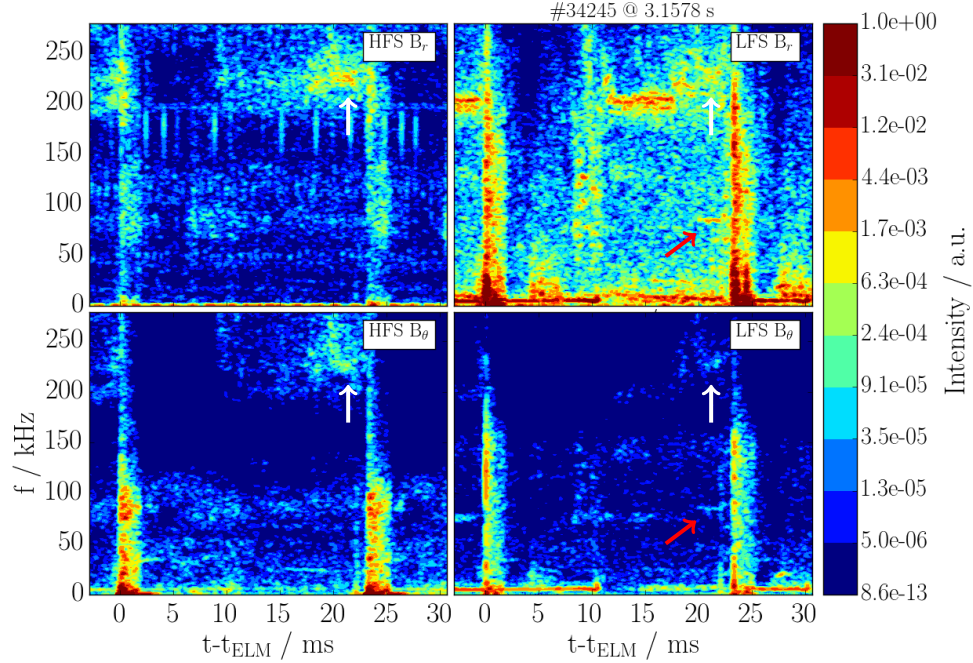


Figure 5.15.: Spectra during one ELM cycle of magnetic pick-up coils measuring the radial magnetic field B_r or the poloidal magnetic field B_θ fluctuations on HFS and LFS.

reduction of n . Within this speculative hypothesis modes of the ELM cycle are interpreted as ballooned modes but the coupling to current driven fluctuations enables the pedestal to reach its final ballooning unstable value in order to make the crash possible. However, the typical picture of high n ballooning modes does not fit to this hypothesis.

5.4. Summary and Discussion

Several magnetic activities with defined mode numbers could be identified at several radial positions during the cycles of edge localized modes (ELMs). From the evolution of the mode numbers together with the evolution of the pedestal profiles at least six clearly separated phases forming the cycle could be identified. These are four phases after the ELM crash, the pre-ELM phase and the ELM crash phase itself. These phases appear in a similar manner for each ELM cycle, which makes the method of ELM synchronization a valuable tool in order to get good statistics for mode number and profile determination. During the first phase after the ELM crash no electromagnetic signal from the edge is visible. In all other

phases around the ELM several branches with a variety of mode numbers with $n \leq 10$ but fixed f/n values and thereby velocities are present. This indicates that MHD modes with complex mode structure appear at distinct radial positions. From a comparison to the edge plasma rotation these modes could be located in the strong gradient region close to the plasma boundary, which is also supported by measurements from reflectometry. A further determination of the position in terms of the safety factor q confirms this localization, i.e. fast mode branches with frequencies $f = 200\text{--}250$ kHz are most probably at the minimum of the radial electric field and have no phase velocity. This is also in line with the fact that ballooning modes are stabilized by the velocity shear. This shear is zero in the minimum, i.e. $dE_r(r)/dr = 0$. Slower mode branches are likely to be further outwards close to the separatrix, where E_r values have too high uncertainties in order to pin down their phase velocity. The role of these fluctuations remains an open question. A speculative statement could be that high frequency modes are ideal ballooning modes, which provide enough transport for clamping the pressure gradient between ELM crashes. As in some cases they clearly decrease their amplitude when medium n fluctuations shortly before the crash set in, they might not be directly connected to the crash. Furthermore, as low n modes are expected to be more current driven, it might be that the current and thereby q profile changes shortly before the ELM crash, which might also influence high frequency ballooning modes, due to shear stabilization.

Determination of mode numbers during the ELM crash is difficult because of the very fast development, but the low frequencies that have been detected during the ELM fit to the drop of poloidal velocity in this phase and a continuous n structure around $n = 3$ in this phase looks very similar to the dominant structure in the pre-ELM phase. Therefore, the ELM crash is interpreted as the breakdown of the plasma rotation combined with the existence of a strong low n mode structure, which is confirmed in the next chapter with an upgraded pick-up coil system. The origin of the $n = 0$ and $n = -6$ mode structure that starts during the ELM phase and ends during the recovery phase remains unexplained, but it might be connected to the appearance of an $n = 0$ geodesic Alfvénic mode or filamentary structures. Any m determination is impossible during the crash because of the lack of a reliable equilibrium.

Although ELM synchronization displays common features with good statistics the results for mode numbers in different phases also need to be validated with single ELM evaluations as the ELM cycles are similar but still individual. Therefore, a single ELM mode number determination was performed for the phase just before the ELM crash showing, similar to the ELM synchronized picture, that dominant mode numbers jump from high to low n just before the crash. A more detailed analysis of the ELM crash and its precursor is given in the next chapter. Furthermore, these experimental results are compared to simulated

output from JOEKE in order to shed light into what is the ELM triggering mechanism. An analysis of a broader parameter space in terms of the edge current density j , pressure gradients α and the magnetic shear s and their influence on the ELM crash is presented in chapter 7.

6. Comparison of the ELM Crash Structure to Nonlinear Simulations

Relaxation events induced by nonlinear coupling are not only important for magnetically confined plasmas [63], but also for astrophysical plasmas [122–124] and even in daily life mechanical systems [125, 126].

As explained before, the onset criteria of ELMs is classically described by the linear peeling-ballooning boundary [38, 40, 43], see chapter 2.3. Nevertheless, linear models can only determine whether a certain mode can potentially grow. The development and the transport characteristics of modes are only accessible via nonlinear calculations, as suggested for instance by *Snyder et al.* [127]. Nonlinear models also open up the window to purely nonlinear phenomena like saturated modes, cyclic behavior or coupling of different modes [47, 128]. Furthermore, such nonlinear mode coupling is thought to be responsible for the fast increase of growth rates at the ELM onset [112, 118, 129].

In the first part of this chapter the ELM crash itself is thoroughly investigated in terms of mode number n derived from magnetic measurements. As n is an essential parameter which can be used to check validity of ELM models, a comparison of experimentally determined n numbers with ones obtained by the nonlinear MHD code JOREK is presented in the second part. Parts of the results from this chapter are published in [65].

6.1. Mode Numbers of the ELM Crash

As the spatial structure of ELMs is a desirable parameter in order to check the validity of ELM models, several authors have made efforts to determine structures appearing during or close to the ELM onset with different diagnostics and methods on various machines.

Among these methods are imaging techniques from fast cameras or from 2D electron cyclotron emission which usually observe high mode numbers in the range of $n = 10$ – 30 [49–54]. Those methods mainly rely on estimating the distance between several maxima of the modes. This is correct as long as there is only one dominant structure present. For other cases, these methods might not give access to the full mode spectrum since they neglect the interference of the different Fourier components [130]. Such an overlap of

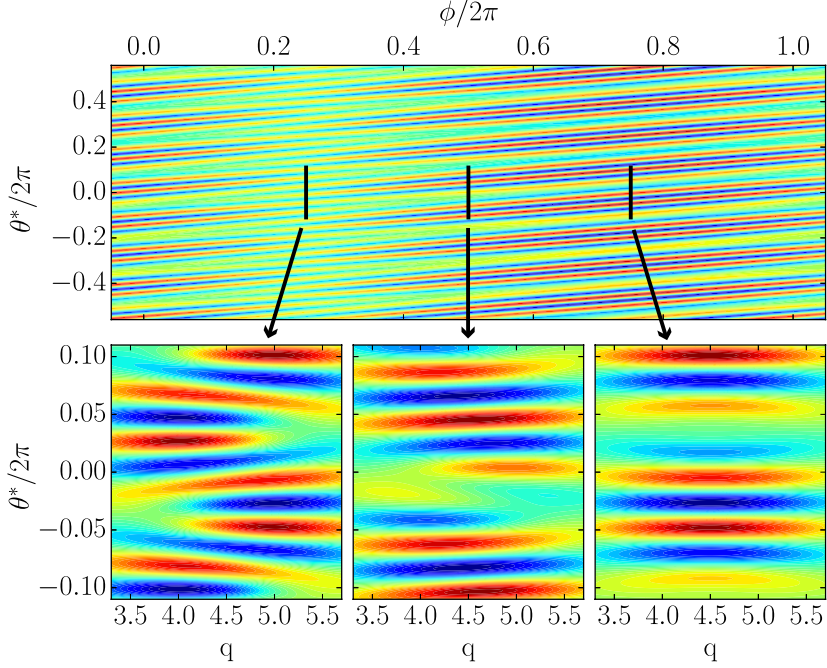


Figure 6.1.: Mode structure of three modes with $m/n = 20/4, 20/5$ and $27/6$ at $q = 5, 4$ and 4.5 . The modes have a Gaussian shape amplitude profile in q with a width of $\Delta q = 1$. The top plot shows the mode structure in the θ^*/ϕ plane. The bottom plots show the poloidal structure that would be seen in imaging diagnostics in the θ^*/q plane at the three positions marked in the top plot.

modes is visualized for artificial data in figure 6.1. The top plot shows the structure of three overlapping and thereby interfering modes with $n = 4, 5, 6$ at $q = 5, 4, 4.5$ in the θ^*/ϕ plane. Imaging techniques such as 2D ECE usually cover some range in the radial, i.e. $q(r)$, and poloidal plane. Such frames are shown in the bottom plots of figure 6.1. Estimating the distance between minima and maxima for example in the left bottom plot would yield only the mode number of the highest n mode, which is $m = qn = 6 \cdot 4.5 = 27$ ¹. The substructure of the lower m modes is not resolvable from this figure, due to interference. Similarly the other two bottom plots show varying distances between maxima and thereby cannot give any conclusive results without decomposing the image in Fourier components. Such an interference of modes is maybe also the reason why in most of these imaging cases quite high mode numbers in the range of $n = 10-30$ are observed during the ELM crash and a variety of propagation directions is proposed.

However, the most commonly used diagnostic for calculating the structure of modes close to the ELM crash are magnetic pick-up coils measuring either radial or poloidal magnetic

¹ 5.4 oscillation periods are countable in the here covered poloidal region of 0.4π . This gives a poloidal mode number $m = 5.4 \cdot 2\pi/0.4\pi = 27$.

field changes, as explained in chapter 4. Various types of modes are seen on different machines in the edge region that are thought to be important for the whole ELM cycle. They appear in a wide range of frequencies below 500 kHz.

Some of them are usually stationary for up to several milliseconds in a high frequency range of 100–500 kHz with several frequency bands of mode numbers around $n = 10$ and separated by $\Delta n = 1$ [55–58], similar to the ones of phase IV in section 5.1.4. They propagate in the lab frame in electron diamagnetic direction. Their phase velocity is controversially discussed in the listed references. They are also regarded as being responsible for clamping the gradient in between ELM crashes [103, 107], but not being directly connected to the ELM crash. The clamping of the gradient fits to the EPED model [43], which states that the transport induced by kinetic ballooning modes (KBM) is an important ingredient for the pedestal height and width in the ELM cycle. Nevertheless, only some of the important mode properties like stability characteristics or structure size were found to fit to KBMs. Others like rotation velocity or symmetry have large errors or even contradict KBMs.

Other modes investigated in the ELM cycle appear in magnetics in a lower frequency range of 0–150 kHz, similar to the ones of the pre-ELM phase, see section 5.1.5. They also appear with several frequency bands and usually with lower mode numbers $n = 1–7$. Their rotation direction in the lab frame seems to differ between machines. As they tend to appear and grow before the ELM crash, they are often called precursors. In which way they are linked to the crash is not yet clear [56–60].

The modes that appear during the crash itself are reliably studied with magnetics only in very rare cases [61, 62], but usually very low mode numbers of $n = 1–4$ are found dominantly during the crash.

In this chapter, we present measurements by magnetic pick-up coils on the ASDEX Upgrade tokamak which were able to decompose the slowly propagating, short-lived toroidal substructure of the ELM cycle including the ELM crash and the ELM precursor modes. Again the technique of ELM synchronization of temporal Fourier analysis is used, which allows to determine not only the structure but also rotation velocities of the ELM. The experimental findings in terms of mode numbers, velocities, growth rates and kinetic profiles during the crash are then compared to results from the nonlinear MHD code JOREK [63].

6.2. Experimental Investigations

The ASDEX Upgrade discharge #33616 was considered to determine the structure of the modes appearing before and during the ELM crash. In this discharge, a long constant

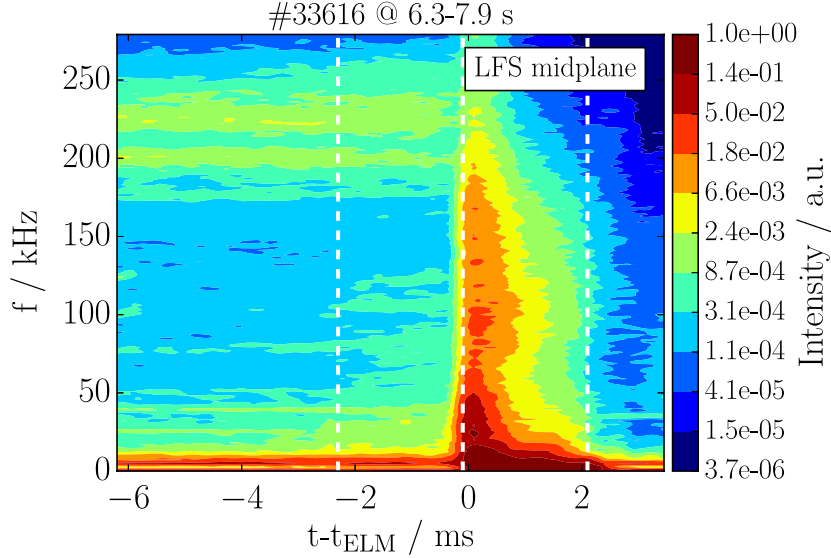


Figure 6.2.: Spectrum taken from a LFS midplane coil synchronized to the ELM onset at $t - t_{\text{ELM}} = 0$ ms of 52 ELMs. 10-125 kHz fluctuations increase about 2 ms before the crash, which itself is then dominated by low frequencies < 20 kHz.

phase from 6.3–7.9 s with a plasma current of 800 kA, magnetic field of 2.5 T, total heating power of 4 MW, edge safety factor $q_{95} = 5.2$ and with a low ELM frequency of around $f_{\text{ELM}} = 50$ Hz was obtained. ELM induced losses of thermal energy and particles were of about 6% and 8% respectively, during which the maximum pedestal pressure gradient drops by a factor of three. Discharge parameters were chosen to be similar to the discharge analyzed in the previous chapter, but an extension of the toroidal pick-up coil array enabled the precise determination of the n structure during the crash for this discharge.

Figure 6.2 shows a magnetic spectrum from a low field side (LFS) midplane radial magnetic pick-up coil, synchronized to the onset at $t - t_{\text{ELM}} = 0$ ms of 52 similar ELMs. Again the onset and end of the ELMs are defined from an amplitude threshold in the magnetics. This definition is similar to divertor signals like D_α or shunt current measurements, but reduces smearing of synchronized magnetic signals to ≤ 0.1 ms. Several milliseconds before the crash, saturated modes with frequencies around 200–250 kHz are visible. In addition, medium frequency fluctuations at 10–125 kHz are visible and their amplitude increases about 2 ms before the crash, which is why they are called precursors in the following.

During the ELM crash, $t - t_{\text{ELM}} = 0$ –2 ms, the spectrum is broad in frequency, but the low frequencies (< 20 kHz) are dominant. Growth rates of the magnetic amplitude $\gamma = \frac{dB/dt}{B}$ at the onset are of the order of $(5 \pm 2) \cdot 10^4 \text{ s}^{-1}$. This growth

rate was estimated from a sliding average with $150\ \mu\text{s}$ length and $15\ \mu\text{s}$ separation. Such filtering is necessary in order to reduce the effect of noise in the magnetics. Figure 6.3 shows two ELM synchronized mode number spectra. Again the negative sign of the most dominant mode numbers in the spectrum by convention indicates a rotation in the electron diamagnetic drift direction. In the following the sign is, however, omitted for readability. These mode number spectra are obtained by determining mode numbers that appear in a window of $2.2\ \text{ms}$ duration. The center of these windows are $1.2\ \text{ms}$ before and $1.0\ \text{ms}$ after the ELM onsets respectively for a) and b). The $2.2\ \text{ms}$ are needed in order to get a good frequency resolution. In that sense it is an average over the whole crash event and cannot resolve the detailed evolution during the crash. Evaluated time windows are also marked with white dashed lines in figure 6.2. The resulting mode numbers of all these windows around the 52 ELM onsets in the here investigated time trace are then binned together. Below $30\ \text{kHz}$ the spectrum is influenced by an $n = 1, m = 2$ core mode. As the core mode is not expected to have a strong impact on the edge, the mode number spectrum in Figure 6.3 a) is blue shaded below the grey dashed line at $f = 30\ \text{kHz}$ to guide the eye towards the ELM relevant medium to high frequency edge fluctuations. Before the ELM onset the spectrum is dominated by the high frequency fluctuations with $n = 8, 9$ and 10 . Then, closer to the ELM onset, precursor fluctuations with $n = 3-6$ with frequencies of $35-125\ \text{kHz}$ increase in intensity.

The total velocity, i.e. plasma and phase velocity, determines together with n the frequency of the modes, see equation 4.2. Thereby the n components of similar f/n rotate with the same velocity. Due to the strong shear of the edge rotation it is highly probable that the structures $n = 8, 9$ and 10 at frequencies of around $200, 225$ and $240\ \text{kHz}$ (green dashed arrow) before the onset are at the same position in the plasma, forming again a mode *branch*. The same holds for the $n = 4, 5, 6$ components with frequencies of $80, 100,$

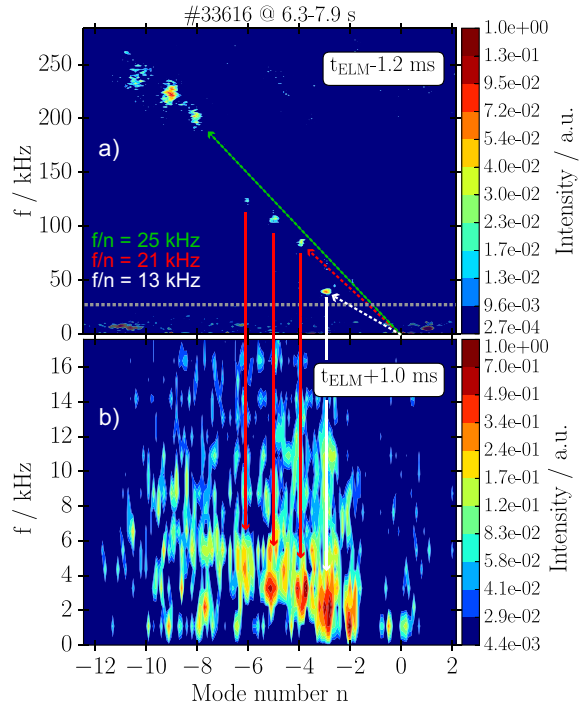


Figure 6.3.: Frequency resolved mode number spectra of a time window a) shortly before and b) during the ELM crash. The low n structure of the pre-ELM components below $125\ \text{kHz}$ appears with strongly reduced f/n but similar dominant $n = 2-5$ also during the crash.

120 kHz (red dashed arrow). The $n = 3$ component is the slowest one with $f/n = 13$ kHz (white dashed arrow). The n components in such a branch are prone to coupling as they have the same velocity and position. However, experimental evidence for coupling from bi-coherence analysis was not found in this quasi saturated phase [131].

The uncertainty of 1–2 kHz in f/n reflects a width below 5 mm of the mode branches in the strongly sheared edge rotation. Again, measurements of the poloidal mode numbers show for the $n = 4$ component of the slower branch $m \approx 32$, whereas $m = 50$ –60 for the $n = 9$ component of the faster branch. This suggests again that slower mode branches of the precursor modes have higher $q = m/n$ and are therefore located further outside close to the separatrix, whereas mode branches with high f/n have lower m/n and are placed further inwards close to the $E \times B$ minimum which is usually around $q = 6.5$ for this type of discharges.

During the crash, figure 6.3 b), the dominant mode numbers are $n = 2$ –5, which is very similar to the preexisting $n = 3$ –6 structure, highlighted with the vertical solid arrows. This low n structure during the crash is a general feature of many ASDEX Upgrade discharges, which only varies slightly with usual parameters like collisionality ν^* or plasma β , which will be shown in chapter 7. It appears with $f/n \leq 1$ kHz (note the different scaling of the frequency axis). This reduction of velocity compared to the precursor is a result of the E_r reduction at the ELM onset from typically 40 to 10 kV/m [46, 110]. Another ingredient for the velocity reduction might be an additional outwards propagation into the region of reduced absolute E_r and a possible coupling due to increased mode amplitude to external error fields leading to a braking of the rotation.

6.3. Nonlinear Simulation of the ELM Crash

The experimental results for the mode numbers during the ELM crash form an excellent basis for comparing simulations and experiments. With this in mind, an ELM simulation was done with the nonlinear MHD code JOEAK [63] based on a CLISTE [132] pre-ELM equilibrium reconstruction of the same discharge #33616 at $t = 7.2$ s which is peeling-ballooning unstable. The reconstructed equilibrium is based on kinetic profiles just before the ELM crash averaged over several ELM cycles from Thomson scattering, Li-beam and ECE diagnostics [72, 82, 133]. The computational domain covers main plasma, scrape off layer and private flux region including geometrically simplified divertor targets where Bohm boundary conditions apply (refer to [134, 135] for the model). Diamagnetic and neoclassical flows are included, background parallel flows inside the plasma are not considered for simplicity since they do not affect the ELM crash strongly due to the large parallel

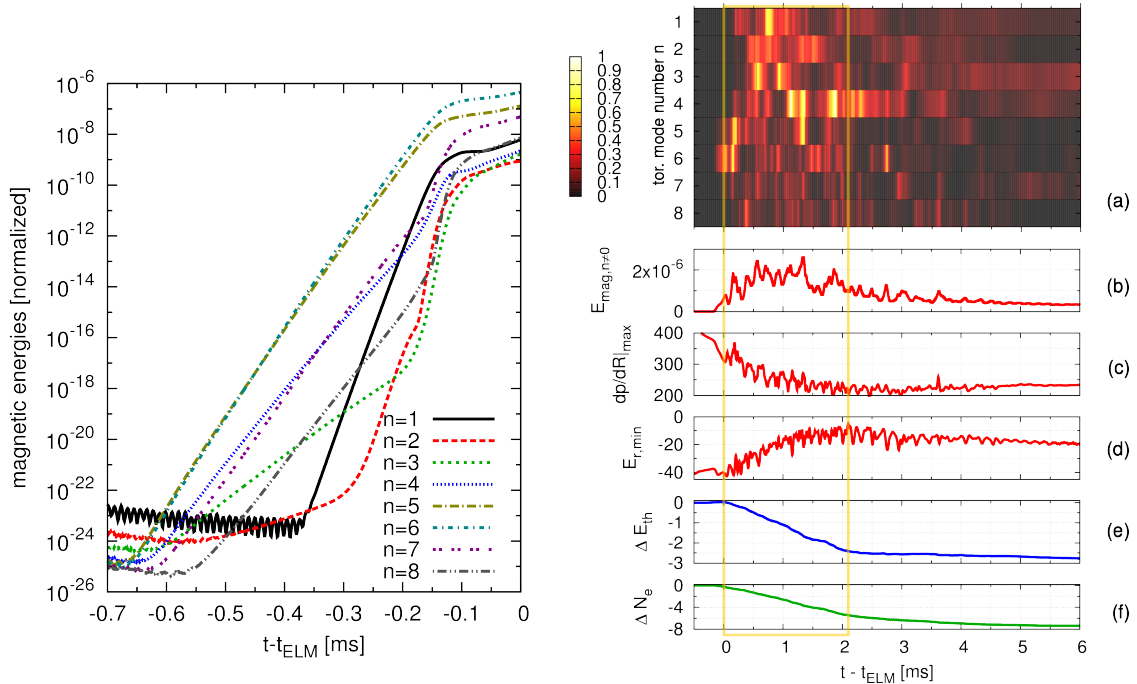


Figure 6.4.: **Left:** Time traces from the simulations of the magnetic energies of different modes on a logarithmic time scale for the onset of the ELM crash. **Right:** Time traces from the simulation of (a) magnetic energy (a.u.) for each toroidal mode number $n = 1$ –8, (b) sum of the magnetic energies for $n \neq 0$ (a.u.), (c) maximum pressure gradient in the midplane (kN/m^3), (d) minimum of E_r at the midplane (kV/m), (e) losses of thermal energy (%), and (f) particle losses (%). The vertical lines mark the beginning and end of the ELM crash.

wave length of the ELM structures. Plasma resistivity is significantly more realistic than in previous ELM simulations for ASDEX Upgrade [112, 136] but still a factor of eight larger than the experimental value. Such a simplification in the model is needed in order to reduce computational time. Note that these earlier simulations also did not account for diamagnetic drift effects such that much higher mode numbers had been obtained due to this missing two-fluid stabilization term acting dominantly on high mode numbers. Scans confirm that time step, resolution, hyper-resistivity and viscosity do not influence results. The parallel heat diffusion coefficient is chosen about two orders of magnitude smaller than the Spitzer-Härm values [137] to account for the so-called heat flux limit [138, 139]. Additional details regarding the simulation setup can be found in the appendix A. The simulation includes toroidal mode numbers $n = 0$ –8. Linear analysis and single simulations with mode numbers up to 16 showed that $n > 8$ modes are strongly sub-dominant and not needed to be considered in this case. Note that this is in contrast to the $n = 8, 9, 10$ modes observed in the phases between ELM crashes experimentally (however not during the ELM

crash itself). The stability of these modes in simulations can have two different reasons: Either the initial conditions do not reflect accurately enough the experimental state, or these modes cannot be described in the MHD picture.

Time traces of the most important quantities from the simulation around the ELM crash are shown in Figure 6.4. From a small initial perturbation (only visible on logarithmic scale, see left part of Figure 6.4), the peeling-ballooning instability starts to grow exponentially from time $t - t_{\text{ELM}} = -0.67$ ms. All times for the simulation are given relative to the ELM onset time t_{ELM} defined by the start of the rise of the outer divertor heat flux in the simulation due to the crash, which makes the timing comparable to the one in the experiment.

The $n = 6$ and 5 components are linearly dominant with a growth rate of about $5 \cdot 10^4 \text{ s}^{-1}$. Note that the growth rates in the simulations are determined by equilibrium reconstruction, physics parameters, and background flows such that a really self-consistent comparison will only be possible with full ELM cycle simulations at fully realistic parameters. Nevertheless, from -0.37 ms onward, nonlinear drive of sub-dominant mode numbers [112] (first $n = 1$ by a coupling of $n = 5, 6$) can be observed, and at about -0.1 ms nonlinear saturation starts to set in.

During the ELM crash itself (right part of Figure 6.4), from about 0 to 2 ms, thermal energy and particle losses are observed across the separatrix. About 2.5% of the thermal plasma energy and 7% of the particles are lost, figure 6.4 (e),(f). These thermal energy ELM losses are smaller than in the experiment by a factor of about two (2.5% versus $6 \pm 1\%$) whereas particle losses are almost identical (7% versus $8 \pm 1\%$). Accounting for time-varying background turbulence levels during the ELM cycle and treating the heat flux limit of parallel transport more accurately might allow to resolve this discrepancy. The divertor heat flux starts to rise at $t - t_{\text{ELM}} = 0.00$ ms for the outer and at 0.07 ms for the inner target. During the ELM crash, $n = 3-5$ modes are dominant while $n > 6$ modes remain strongly sub-dominant, figure 6.4 (a). The spatial structure of the instability simultaneously involves several rational surfaces rotating with different velocities corresponding to the different branches observed in the experiment². Figure 6.5 visualizes this spatial structure of the current perturbation at several ρ positions close to the plasma boundary. Additional simulations were carried out to identify key ingredients for obtaining the experimental mode spectrum. Restricting the mode numbers included in the simulation to even $n = 0, 2, 4, 6, 8$ or $n = 0, 3, 6, 9$ instead of the full spectrum ($n = 0-8$) leads to an almost pure $n = 6$ mode during the ELM crash and, when excluding diamagnetic flows, $n \geq 7$ modes dominate. This highlights that the spa-

²Note that in the here investigated case only one clear branch is recognizable during the crash. However, several cases also show multiple branches. One of these is shown in figure 8.3 (c).

tial structure of the ELM is reproduced in the simulations only when taking into account the diamagnetic drift term and accounting for nonlinear mode coupling involving $n = 1$. In particular, the toroidal mode structure differs significantly from the linear spectrum. The maximum pressure gradient in the outer midplane drops approximately by a factor of two during the crash, figure 6.4 (c), and the radial electric field (E_r) well is reduced from about -35 to -15 kV/m, figure 6.4 (d), leading to a much lower $E \times B$ rotation. After the crash, magnetic fluctuations drop significantly and energy and particle losses cease. Pressure gradient and E_r well slowly start to recover. Fluctuating modes dominated by $n = 4$ persist until about 4.0 ms. Then a slowly evolving $n = 3$ structure becomes dominant for more than 5 ms, figure 6.4 (a). Due to the ELM crash, 2/1 and 3/2 islands arise with a width of $w_{2/1} \approx 1$ cm, which decay away slowly such that they would clearly “survive” until the next ELM crash. The experimentally observed seeding of neoclassical tearing modes by ELMs [140, 141] could, thus, be a cumulative result of several ELM crashes. These magnetic fluctuations after the ELM crash are roughly a factor of five smaller than during the ELM crash in experiment as well as in modeling. This magnetic activity is correlated with fluctuations of density and temperature in the pedestal region which do not cause strong losses and are also observed experimentally in ECE imaging measurements in the phase between ELM crashes [120].

In the region $\rho_{\text{pol}} \gtrsim 0.85$, field lines become stochastic during the ELM and closed flux surfaces only recover slowly after the crash. Stochastization can be observed inwards up to $\rho_{\text{pol}} \approx 0.78$ in certain phases (Fig. 6.6 for simulation time $t = 0.987$ ms). Be aware that θ_{geo} is the real space coordinate, which causes a spread of the structures close to the outboard midplane ($\theta_{\text{geo}} = 0$). Stochastic fields are important for the ELM energy losses and thus

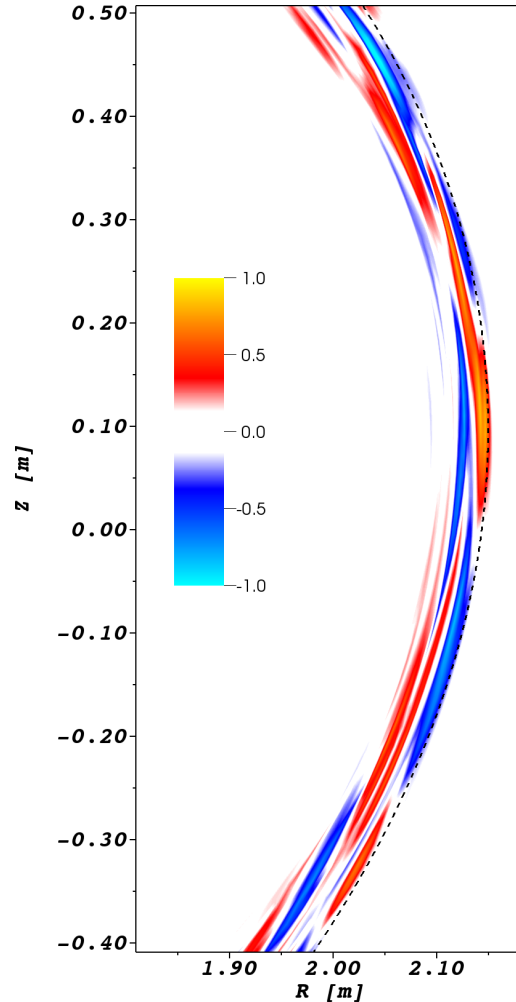


Figure 6.5.: Perturbation of the plasma current during the ELM crash at $t - t_{\text{ELM}} = 1.14$ ms of the JOEK simulation. Several rational surfaces close to the plasma boundary are involved simultaneously which corresponds to different rotation velocities as seen in the experiment.

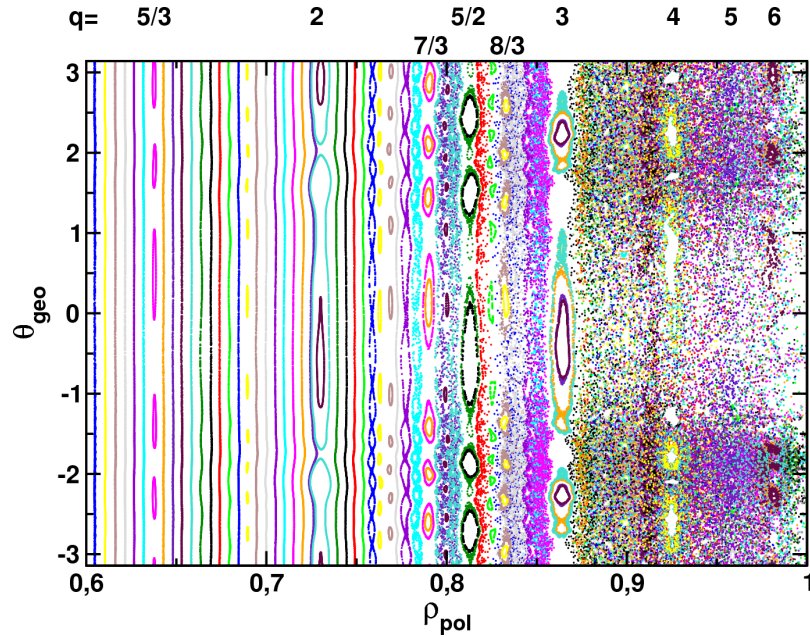


Figure 6.6.: A Poincaré plot is shown in radial and poloidal coordinates to illustrate the magnetic topology during the ELM crash obtained in the JOREK simulation ($t - t_{\text{ELM}} = 0.987$ ms). θ_{geo} corresponds to the poloidal real space coordinate. Safety factor values corresponding to some of the island chains are given at the top.

for the ELM dynamics. For the formation of the stochastic layer, the excitation of several toroidal mode numbers by nonlinear mode coupling is important since it modifies the edge magnetic topology and thus the connection from bulk plasma to the divertor.

6.4. Discussion and Outlook

The upgraded coil system at AUG allows the extraction of key information about ELM crash and activity between ELM crashes.

These experimental observations and the nonlinear ELM simulation show excellent agreement regarding key features such as the ELM duration of about 2 ms, growth rates in the order of $5 \cdot 10^4 \text{ s}^{-1}$ and the dominant toroidal mode numbers $n = 3-5$ during the crash. In both cases mode numbers larger than $n = 6$ are clearly sub-dominant, which is also in agreement with previous experimental investigations [61, 62]. Nonlinear mode coupling involving the $n = 1$ component as well as diamagnetic drift are key ingredients for obtaining this spectrum in simulations. In the simulation, thermal energy ELM losses are smaller than in the experiment by a factor of about two whereas particle losses are almost identical. According to the simulations edge stochasticization is responsible for the fast temperature

collapse in the plasma edge due to the fast parallel heat transport, highlighting the role of reconnection for this process during the ELM crash [142].

In the experimental analysis, figure 6.3 (b), a relatively broad frequency spectrum is observed during the ELM crash which can be explained by several effects observed in the simulation: Changing rotation during the crash, a radial mode structure spreading over several rational surfaces with different local rotation velocities, and fluctuating amplitudes within the analysis window. Furthermore, the important $n = 1$ component visible in the modeling might not be accessible to the temporal Fourier analysis due to its long wavelength and short life span which do not allow to measure a full oscillation period. A one-to-one comparison via virtual diagnostics is planned for the near future using the free-boundary extension JOREK-STARWALL [143].

Before the crash, a precursor mode with a similar mode structure as the crash is observed experimentally. Up to now this phase cannot be compared to the simulation which is started from an unstable equilibrium already. Simulations started from a stable state, where the plasma is crossing the stability boundary due to the build-up of pedestal profiles are planned for the near future as well. Those simulations might also show saturated modes when the equilibrium is only barely unstable and a sudden crash when the ideal ballooning stability boundary is reached.

Significant progress in the experimental analysis of ELM crashes has been obtained and strong evidence was shown that JOREK nonlinear simulations reproduce key aspects of ELM crashes. The following chapter will show how the experimentally obtained ELM crash characteristics vary with plasma parameters. This can open up the possibility for future comparisons to simulations and thereby a more detailed check of validity of JOREK output under parameter variation. Results for mode numbers of fast transient ELM-like events during advanced scenarios like the I-phase or ELM suppression scenarios are presented in the last chapter, which might be investigated with simulations in the future as well.

7. Influence of Plasma Parameters on the ELM Structure

In the previous chapters the mode numbers appearing in the ELM cycle and the ELM crash were investigated for a very narrow range of discharge parameters. The question that needs to be clarified in order to understand the ELM is how these findings vary within a greater parameter range and furthermore whether changes of the structure of the ELM is according to the predictions from basic theory. In this chapter a data base containing about 30 H-mode discharge phases¹ with more than 2500 ELMs is analyzed in terms of the toroidal mode numbers appearing during and slightly before ELM crashes.

7.1. Mode Numbers Before and During the Crash

As explained in the previous section the ELM crash appears with dominant low n mode structure. Furthermore, just before the ELM crash modes already appear with a comparable structure. In a series of 30 time traces the toroidal mode numbers that appear during the crash and in the precursing modes were identified. These precursing modes are always in a frequency range $f = 0\text{--}150\text{ kHz}$ and thereby are well separated from high frequency modes with $f \geq 200\text{ kHz}$. Furthermore, their amplitudes tend to rise before the crash, whereas high frequency modes usually stay constant on signals from the LFS radial field coils or even vanish before the crash. As shown in chapter 5.2 high frequency modes are placed in the $E \times B$ minimum, whereas $f = 0\text{--}150\text{ kHz}$ modes are closer to the separatrix. In order to get a comparable quantitative measure for the different mode number distributions, a weighted mean and standard deviation was introduced. Figure 7.1 visualizes the definition of both quantities for two representative discharge time traces. The figure shows two mode number spectra evaluated from 50 ELM crashes of both discharges (top plots). The two discharges have a different q_{95} of (a) 3.1 and (b) 6.9. The ELM crash is then dominated by different mode numbers, i.e. $n = 2\text{--}7$ for the low and $n = 1\text{--}6$ for the high q_{95} discharge.

¹In total 30 discharges were analyzed, but few of them do not have reliable kinetic profiles

The bottom plot (c) shows the mode number distribution obtained from both time traces together with two Gaussian distributions defined from the weighted mean μ and the standard deviation σ of the distributions. Although mode numbers are not necessarily following a Gaussian distribution both parameters form a quantitative measure for describing the difference in mode numbers. Therefore, an average toroidal mode number and its uncertainty, that are used in the following, are defined as $\langle n \rangle = \mu \pm \sigma$. In the here shown cases this yields $\langle n \rangle = 4.5 \pm 1.3$ and 3.1 ± 1.1 for the low and high q_{95} case.

Similarly to the here defined average toroidal structure of the crash, also the average toroidal structure of the precursing modes that appear before the crash can be defined from mean and standard deviation. Figure 7.2 shows the average mode number $\langle n \rangle_{\text{PRE}}$ of the modes appearing before the ELM crash plotted against the $\langle n \rangle_{\text{ELM}}$ obtained during the crash of 30 evaluated H-mode discharges covering a broad parameter range². Furthermore, the bisecting line, indicating the points where $\langle n \rangle_{\text{PRE}} = \langle n \rangle_{\text{ELM}}$, is shown in green. From this plot it can be concluded that precursing modes just before the crash have similar toroidal structure as the crash itself. It is not necessarily true that structures before and during the crash are exactly the same as some of the discharges show deviations from the bisecting line even within their errorbars, i.e. precursing modes

²Details of the parameter range will be clarified in the following sections.

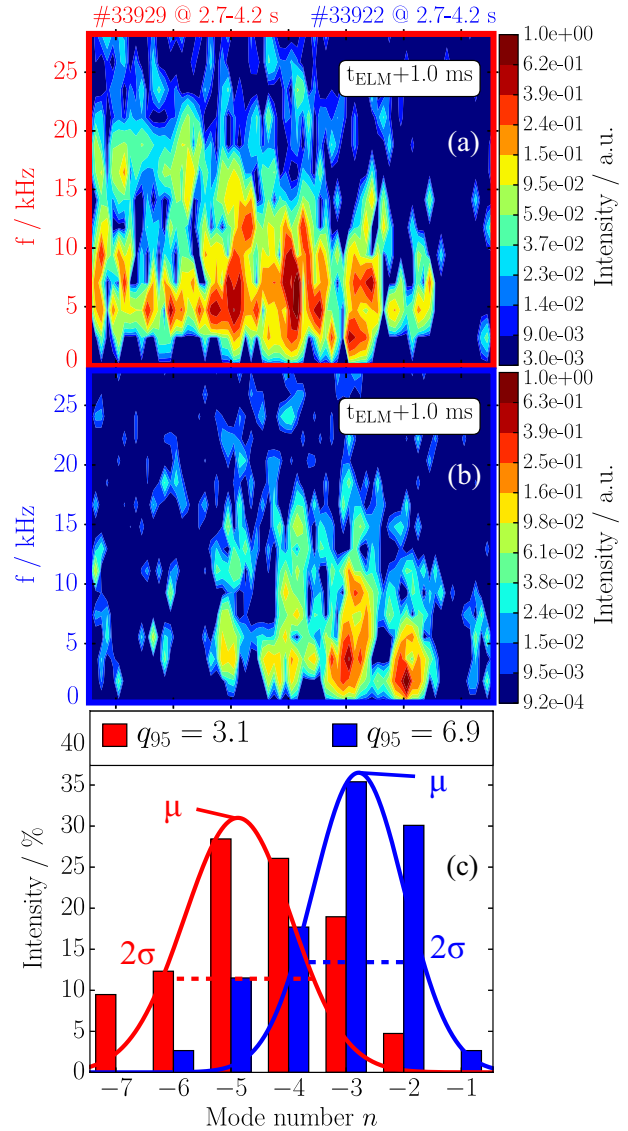


Figure 7.1.: Toroidal mode number distribution (c) and n spectra (a,b) of the ELM crash for two discharges with different q_{95} . Spectra are evaluated for both discharges for a 2 ms time window around 1 ms after 50 ELM crash onsets. The distributions are described by weighted mean μ and standard deviation σ , according to the fitted Gaussian lines.

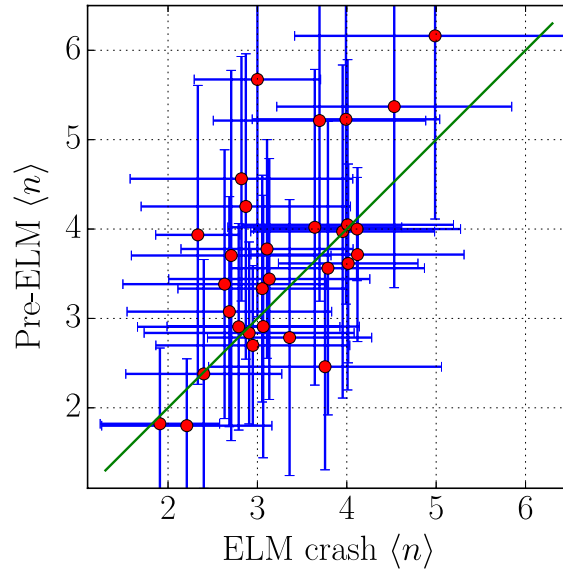


Figure 7.2.: Average toroidal mode numbers $\langle n \rangle$ of mode structures before ELM crash and during the crash. The bisecting line indicating $\langle n \rangle_{\text{PRE}} = \langle n \rangle_{\text{ELM}}$ is plotted in green.

have by trend slightly higher $\langle n \rangle$ values. Nevertheless, higher $\langle n \rangle_{\text{PRE}}$ also show higher $\langle n \rangle_{\text{ELM}}$ and low $\langle n \rangle$ accordingly. Furthermore, what can be concluded is that there are no cases where precursing medium frequency modes have high mode numbers like the high frequency oscillations of $n \approx 10$. Similarly also the crash does not have such high mode numbers even in a very broad parameter range of ASDEX Upgrade discharges. This fits to the results obtained in the previous chapter, that the ELM crash is always a result of nonlinear coupling yielding low n modes. Furthermore, the similarity of structures before and during the crash points in the direction that the mechanism that determines their n is similar. Both phenomena can maybe only exist due to the nonlinear coupling to low n . It remains an open question, however, whether their similar structure also imposes that their drive is the same. If this would be the case both phenomena would be technically the same thing and the structure before the crash might even determine the ELM crash structure.

7.2. Influence of Plasma Parameters on the Structure of the ELM Crash

From the very basic peeling-ballooning theory it is expected that the ELM is driven by edge current density and pressure gradient. Both parameters can cause modes to become unstable and the structure of the modes is thought to shrink in size (increase in n) and is more poloidally asymmetric if it is more pressure than current driven [28]. Furthermore,

both types of modes, i.e. high n pressure driven and low n current driven, also have stabilizing parameters like the magnetic shear s . Moreover, edge current density cannot be independent from the pressure gradient due to the neoclassic bootstrap current [144], see equation 2.22. This complexity makes it difficult to predict an easy rule of thumb stating for example that increasing the pressure gradient should increase mode numbers and poloidal asymmetry seen during the crash. However, nonlinear modeling should give conclusive results on how mode numbers change with plasma parameters, but this is computationally expensive. Therefore, discharges were done in a wide parameter range in order to investigate their influence on the structure and other properties of the ELM crash. This data base can then be used as a look up table for future comparisons to modeling.

The parameters and their range investigated in the database are:

- | | |
|-------------------|---------------------------------------------------------------------------------------------------------------------------------------------------------------------------------------------------------------------------------------------------------------------------------------------------------------------------------------------------------------------------------------------------------------------------------------------------------------------------------------------------------------------------------------------------------------------------------------------------------------------------------------------------------------------------------------------------------------------------------------------------------------------------------------------------------------------------------------------------------------------------------------------------------------------------------------------------------------------------------------------------------------------------------------------------------------------------------------------------------------------------------------------------------------------------------------------------------------------------------------------------------------|
| Plasma parameters | <ul style="list-style-type: none"> • pedestal top density $n_e \in [2.0, 7.5] \cdot 10^{19} \text{m}^{-3}$ • pedestal top temperature $T_e \in [230, 650] \text{eV}$ • maximum pressure gradient $\nabla p \in [100, 350] \text{kPa/m}$ • maximum normalized pressure gradient $\alpha = -\nabla p \frac{2\mu_0 R_0 q^2}{B^2} \in [2.0, 8.5]$ [30] • plasma current $I_p \in [0.6, 1.1] \text{MA}$ • toroidal magnetic field $B_t \in [1.8, 3.0] \text{T}$ • pedestal top plasma beta ("effectiveness") $\beta = \frac{2\mu_0 p}{B^2} \in [0.3, 2.8] \%$ • maximum bootstrap current density $j_{\text{BS}} \in [0.1, 1.0] \text{MA/m}^2$ [144] • edge safety factor $q_{95} \in [2.95, 7.68]$ • edge safety factor gradient (at $\rho = 0.975$) $\nabla q \in [40, 120] \text{m}^{-1}$ • normalized edge magnetic shear (at $\rho = 0.975$) $s = \frac{r}{q} \frac{dq}{dr} \in [5.6, 6.6]$ [30] • average triangularity $\delta = (\delta_{up} + \delta_{low})/2 \in [0.2, 0.4]$ |
| ELM parameters | <ul style="list-style-type: none"> • average ELM crash toroidal mode number as defined previously $\langle n \rangle_{\text{ELM}} \in [1.9, 5.0]$ • average Pre-ELM toroidal mode number as defined previously $\langle n \rangle_{\text{PRE}} \in [1.8, 6.2]$ • ELM balloonedness $\Theta = \dot{B}_{\text{LFS}}/\dot{B}_{\text{HFS}} \in [2.6, 18.4]$, defined as the ratio of magnetic fluctuation intensity measured during the ELM crash on LFS and HFS • intensity ratio expected during an ELM due to the plasma position $I_{\text{pos}} \in [0.3, 3.3]$ • ELM duration in the divertor shunt current $\tau_{\text{Div}} \in [1.0, 8.5] \text{ms}$ • maximum ELM intensity in the divertor shunt current $I_{\text{Div}}^{\text{ELM}} \in [4, 40] \text{kA}$ • absolute plasma energy losses during the ELM $\Delta W_{\text{MHD}} \in [1, 50] \text{kJ}$ • relative plasma energy losses during the ELM $\Delta W_{\text{MHD}}^{\text{rel}} = \frac{\Delta W_{\text{MHD}}}{W_{\text{MHD}}} \in [0.5, 12] \%$ |

All of the here discussed plasma parameters play a role in the basic linear MHD theory, i.e. whether they drive or hamper current or pressure driven modes. These effects will be discussed in the following. However, the main result of the database will be that these linear theoretical tendencies cannot describe the observed trends in the ELM crash at all. Density and temperature profiles are responsible for the pressure profile, whose edge gradient drives the ballooning modes. Plasma current and toroidal magnetic field produce the confinement via $\nabla p = \vec{j} \times \vec{B}$, however current also drives the current instabilities. The β value gives the ratio of kinetic and magnetic pressure and thereby is a measure for confinement effectiveness, which should also depend on transport due to modes. The bootstrap current density drives peeling modes. It is an additional current contribution that is important in the plasma edge as it is mainly proportional to the pressure gradient. The edge safety factor is not directly linked to the peeling-ballooning model, but it is a proxy for its gradient. The gradient and the normalized gradient of edge safety factor, i.e. the shear s , stabilize especially ballooning modes as they need to be located on several rational surfaces. These different rational surfaces are sheared apart by s and therefore the existence of ballooning modes is prevented. The triangularity δ as a measure for how strongly the plasma is following the shape of a "D" reduces the drive for ballooning modes, which is due to the fact that the driving bad curvature region gets shrunk from it. However, as it also allows higher pressure gradients it might also trigger ballooned modes.

The ELM parameters that might be affected by the plasma parameters are chosen such that they characterize the type of mode present. The average toroidal mode number $\langle n \rangle$ is expected to be higher for ballooning modes than for peeling modes and is therefore a measure for how much the modes are theoretically ballooned. Another measure for the ballooning is the here defined balloonednes Θ . It is given by the intensity ratio that is measured in magnetic pick-up coils on HFS and LFS. However, the magnetic intensity caused by a mode with poloidal mode number m drops with distance in a cylindrical approximation as $I(r) = I_0(r_m/r)^{m+1}$, with r_m the mode position. Therefore the balloonedness has two contributions. One from the intensity of the mode I_0 and one from the distance of the measuring coils on HFS and LFS to the structure. The second contribution is strongly dependent on the plasma position and can be estimated from [30, 107]:

$$I_{\text{pos}} = \left(\frac{R_{\text{out}} - R_0}{R_{\text{coil,LFS}} - R_0} / \frac{R_0 - R_{\text{in}}}{R_0 - R_{\text{coil,HFS}}} \right)^{q_{95} \langle n \rangle_{\text{ELM}}} \quad (7.1)$$

with R_0 the plasma center position and under the assumption that the mode is close to the separatrix at R_{out} and R_{in} at LFS and HFS, respectively and that the ELM poloidal mode number m can be estimated from $m = q_{95} \langle n \rangle_{\text{ELM}}$. Both contributions vary with plasma parameters but only the first one is of physical interest, which is why the second

7. Influence of Plasma Parameters on the ELM Structure

Table 7.1.: Pearson correlation coefficients c_P of discharge parameters: electron density n_e , temperature T_e , maximum pressure gradient ∇p , maximum normalized pressure gradient α , balloonedness Θ , expected intensity ratio due to plasma position I_{pos} , maximum current during ELM crash and precursing the ELM, the balloonedness Θ , expected intensity ratio due to plasma position I_{pos} , maximum current during the ELM crash in the divertor I_{div}^{ELM} , absolute and relative ELM losses ΔW_{MHD} , trianguarity δ , duration of ELM in the divertor τ_{div} , toroidal magnetic field B_t , edge safety factor q_{95} and its derivative in the pedestal ∇q and pedestal shear s .

Parameters	n_e	T_e	∇p	α	I_p	β	j_{BS}	$\langle n \rangle_{ELM}$	$\langle n \rangle_{PRE}$	Θ	I_{pos}	I_{div}^{ELM}	ΔW_{MHD}	ΔW_{MHD}^{rel}	δ	τ_{div}	B_t	q_{95}	∇q	s
n_e	1.00	0.05	0.62	-0.39	0.91	0.86	0.29	0.85	0.64	0.37	0.25	0.66	0.41	-0.13	-0.22	-0.46	-0.61	-0.94	-0.94	0.31
T_e	0.05	1.00	0.63	0.65	0.03	0.45	0.85	-0.05	0.02	0.55	0.06	0.14	0.42	0.01	0.40	-0.22	0.07	-0.09	-0.94	-0.20
∇p	0.62	0.63	1.00	0.34	0.63	0.80	0.78	0.48	0.26	0.71	0.22	0.67	0.55	0.17	0.10	-0.48	-0.35	-0.67	-0.61	0.08
α	-0.39	0.65	0.34	1.00	-0.47	-0.02	0.64	-0.52	0.63	0.36	-0.02	-0.12	0.19	0.09	0.57	0.11	0.18	0.41	0.47	-0.21
I_p	0.91	0.03	0.63	-0.47	1.00	0.76	0.25	0.85	0.58	0.36	0.08	0.74	0.45	0.26	0.32	-0.56	-0.51	-0.95	-0.96	0.13
β	0.86	0.45	0.80	-0.02	0.76	1.00	0.63	0.74	0.63	0.57	0.18	0.71	0.50	0.18	0.17	-0.69	-0.83	-0.81	0.17	0.17
j_{BS}	0.29	0.85	0.78	0.64	0.25	0.63	1.00	0.03	0.19	0.63	-0.03	0.51	0.78	0.35	0.68	0.13	0.63	-0.83	-0.81	-0.11
$\langle n \rangle_{ELM}$	0.85	-0.05	0.48	-0.52	0.85	0.74	0.03	1.00	0.63	0.31	0.26	0.68	0.10	-0.39	-0.46	-0.49	-0.64	-0.89	-0.90	0.19
$\langle n \rangle_{PRE}$	0.64	0.02	0.26	-0.34	0.58	0.63	0.19	0.63	1.00	0.21	-0.04	0.52	0.35	0.05	0.57	-0.31	-0.64	-0.62	-0.64	0.12
Θ	0.37	0.55	0.71	0.36	0.36	0.57	0.63	0.31	0.21	1.00	0.35	0.55	0.44	0.24	0.44	0.07	-0.08	-0.17	-0.17	0.25
I_{pos}	0.25	0.06	0.22	-0.02	0.08	0.18	-0.03	0.26	-0.04	0.35	1.00	0.11	-0.18	-0.29	-0.05	0.07	-0.08	-0.25	-0.17	0.47
I_{div}^{ELM}	0.66	0.14	0.67	-0.12	0.74	0.71	0.51	0.68	0.52	0.55	0.11	1.00	0.56	0.01	0.56	-0.54	-0.67	-0.77	-0.76	0.12
ΔW_{MHD}	0.41	0.42	0.55	0.19	0.45	0.50	0.78	0.10	0.35	0.44	-0.18	0.56	1.00	0.59	0.57	-0.26	-0.17	-0.38	-0.30	-0.05
ΔW_{MHD}^{rel}	-0.13	0.01	-0.17	0.09	-0.15	-0.10	0.32	-0.39	0.05	-0.24	-0.29	-0.02	0.59	1.00	0.57	0.09	0.21	0.26	0.15	-0.22
δ	-0.22	0.40	0.10	0.57	-0.32	-0.03	0.55	-0.46	-0.08	0.21	-0.05	0.01	0.57	0.57	1.00	0.13	0.09	0.29	0.28	-0.12
τ_{div}	-0.46	-0.22	-0.48	0.11	-0.56	-0.57	-0.33	-0.49	-0.31	-0.22	0.07	-0.54	-0.26	0.09	1.00	0.45	0.63	0.62	0.62	0.31
B_t	-0.61	0.07	-0.35	0.18	-0.51	-0.69	-0.13	-0.64	-0.64	-0.35	-0.08	-0.67	-0.17	0.21	0.09	1.00	1.00	1.00	0.60	-0.30
q_{95}	-0.94	-0.09	-0.67	0.41	-0.95	-0.83	-0.27	-0.89	-0.62	-0.48	-0.25	-0.77	-0.38	0.26	0.55	0.63	1.00	0.98	0.98	-0.29
∇q	-0.94	-0.05	-0.61	0.47	-0.96	-0.81	-0.24	-0.90	-0.64	-0.36	-0.17	-0.76	-0.40	0.15	0.62	0.60	0.98	1.00	1.00	-0.15
s	0.31	-0.20	0.08	-0.21	0.13	0.17	-0.11	0.19	0.12	0.25	0.47	0.12	-0.05	-0.22	-0.12	0.31	-0.29	-0.15	1.00	1.00

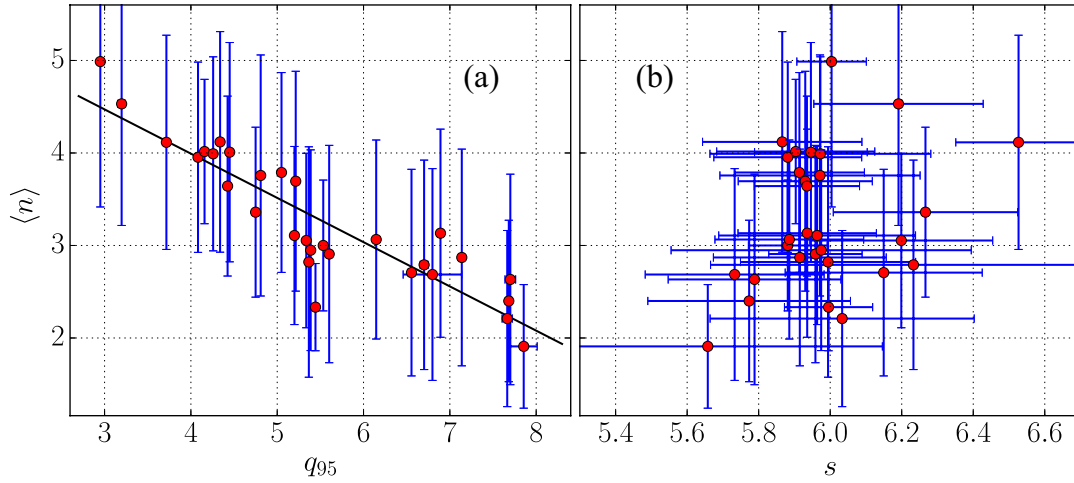


Figure 7.3.: Average toroidal mode numbers $\langle n \rangle$ of mode structures during the crash against (a) edge safety factor q_{95} and (b) normalized magnetic shear s in the pedestal.

contribution needs to be taken into account as well.

Further ELM parameters investigated here are the ELM duration and maximum intensity measured in the divertor shunt current as well as absolute and relative ELM energy losses. The linear MHD theory cannot make any predictive statement on them. However, they are all relevant parameters for characterizing the high divertor heat loads caused by ELMs, which makes it interesting to investigate how they change with plasma parameters.

Table 7.1 shows a matrix containing the Pearson correlation coefficients c_P [145] of all the previously described parameters. The color stands for the strength of correlation, where red shows a linear relation with positive slope and blue with negative. Nonlinear relations cannot be detected by the Pearson correlation and appear with vanishing coefficient (white), so do noncorrelated data.

In the following subsections the toroidal and poloidal structure measures $\langle n \rangle$ and Θ of the ELM crash are discussed in terms of their correlation with other parameters, whereas losses, length and height of ELMs are discussed in section 7.3.

7.2.1. Toroidal Structure of the ELM Crash

As discussed in the previous section the n appearing before and during the ELM are always in a similar range. This is on the one hand reflected by their positive correlation to each other of $c_P = 0.63$ and on the other hand by their correlations with respect to all other parameters being in the same range. As the precursing $\langle n \rangle_{\text{PRE}}$ seem to scatter a bit stronger (lower c_P values), the following discussion will only include the ELM crash struc-

ture $\langle n \rangle_{\text{ELM}}$. Therefore, the index will be omitted for readability ($\langle n \rangle_{\text{ELM}} = \langle n \rangle$). However, similar conclusions as for the $\langle n \rangle$ during the crash can be drawn for the precursing $\langle n \rangle_{\text{PRE}}$. The strongest correlation of $c_P = -0.9$ of $\langle n \rangle$ is found for the gradient of the safety factor ∇q in the pedestal, which is also strongly correlated with the edge safety factor itself ($c_P = 0.98$). This linear dependence of the toroidal structure $\langle n \rangle$ on q_{95} is also shown in Figure 7.3 (a). From basic ballooning theory it would be expected that the normalized magnetic shear $s = \frac{r}{q} \frac{dq}{dr}$ is stabilizing ballooning modes and would therefore cause smaller peeling n during the ELM crash. However, from the experimental investigation shown in Figure 7.3 (b) no clear trend can be observed for s , which is maybe due to the fact that the shear variation in this data base is just about 10%.

As the edge safety factor is mainly determined by plasma current and toroidal magnetic field the question arises whether also one of these parameters could be responsible for determining $\langle n \rangle$. The correlation coefficients suggest a linear dependence of $\langle n \rangle$ on the plasma current, which is in this set of discharges strongly coupled to pedestal top density. This increase of $\langle n \rangle$ with pedestal top density n_e is shown in figure 7.4 (a). Furthermore, figure 7.4 (b) shows q_{95} against the density with $\langle n \rangle$ color coded, going from blue to red with increasing mode number. From the previous plots and the relations shown here it is not clear whether it is the q_{95} or the density and thereby the current that is influencing $\langle n \rangle$. There are discharge pairs with similar q_{95} but varying $\langle n \rangle$ as well as with similar density n_e and varying $\langle n \rangle$. Dedicated experiments would therefore be necessary in order to scan q_{95} with the magnetic field B_t and not via the current. This might disentangle the influence of q_{95} and n_e on the crash structure.

Other parameters that are thought to influence the $\langle n \rangle$ values according to basic peeling ballooning theory seem to play either a minor role or influence the crash either nonlinearly or in a manifold way, which makes correlation analysis useless. Two examples for

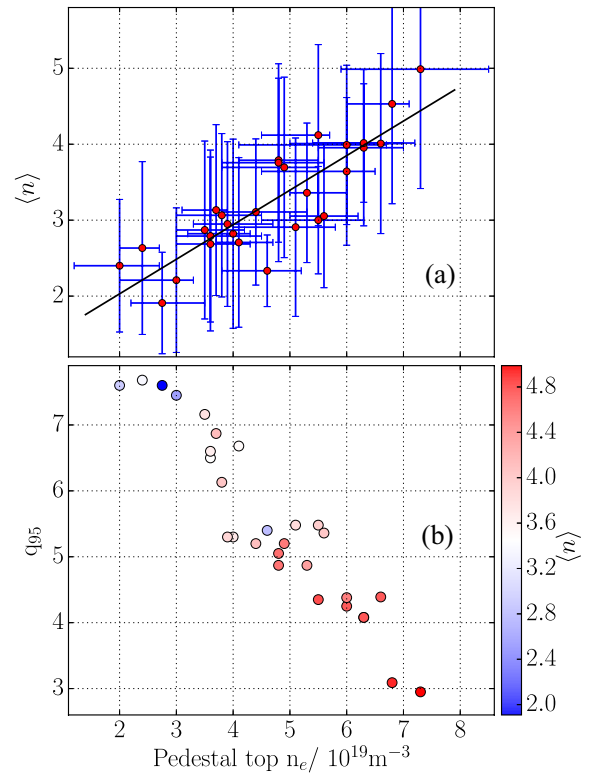


Figure 7.4.: Averaged toroidal mode number dependence on (a) density alone and (b) together with q_{95} , where the blue to red color range stands for low to high n .

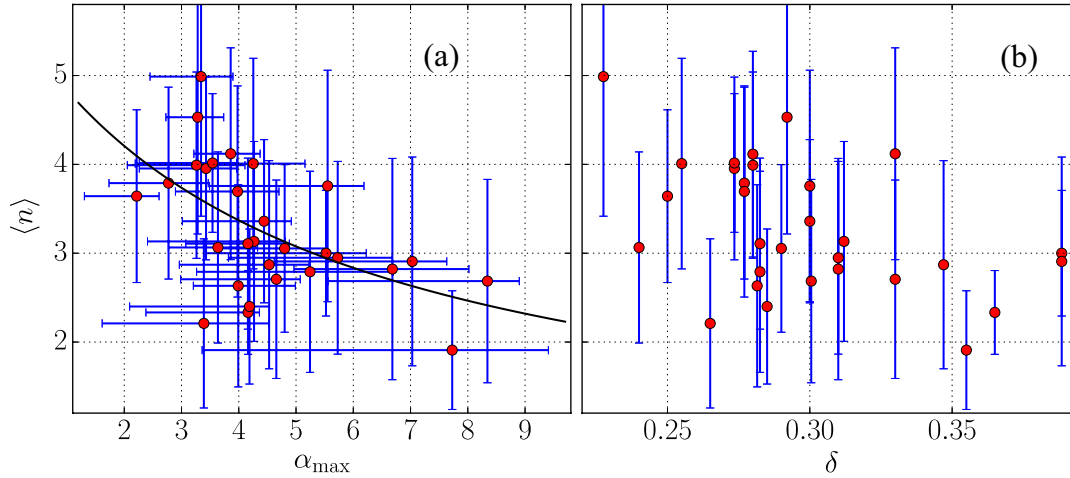


Figure 7.5.: Average toroidal mode numbers $\langle n \rangle$ of mode structures during the crash against (a) the normalized pressure maximum gradient α together with a $1/\alpha$ -fit to guide the eye and against (b) the average triangularity δ .

parameters with such a behavior are the normalized pressure gradient and triangularity. Figure 7.5 (a) shows $\langle n \rangle$ against the maximum normalized pressure gradient α . As pointed out before the ballooning part should play a bigger role if the gradient is increased. On the other hand also the bootstrap current j_{BS} increases which drives the peeling modes more unstable. At the same time the j_{BS} peak changes the local shear giving access to the second stability regime of ballooning modes [146]. It is therefore not straight forward to determine what is expected. The experimental evaluation, however, shows a slight tendency going to lower mode numbers for higher normalized pressure gradient α . The line fitted into the data has a $1/\alpha$ -dependence which follows this tendency. The maximum absolute pressure gradient, on the other hand, has positive correlation with $\langle n \rangle$.

Figure 7.5 (b) shows $\langle n \rangle$ against the average triangularity δ . As pointed out before on the one hand the ballooning modes should be reduced by δ as the bad curvature area is reduced. On the other hand it also allows higher pressure gradient which could then again trigger ballooning modes with higher n . However, from the experimental data investigated here no clear trend can be found, which is also reflected by the small correlation coefficient $c_P = -0.46$.

As a last correlation with $\langle n \rangle$ the parameter space of maximum electron pressure gradient ∇p and bootstrap current density j_{BS} was investigated simultaneously. From the correlation matrix, it can be seen that there exists no correlation of j_{BS} with the toroidal structure $\langle n \rangle$. Nevertheless, effects might overlap and thereby the real influence of j_{BS} on the structure might be hidden. Figure 7.6 (a) shows the bootstrap current density j_{BS} and the maximum electron pressure gradient ∇p with $\langle n \rangle$ color coded. First of all it is clear

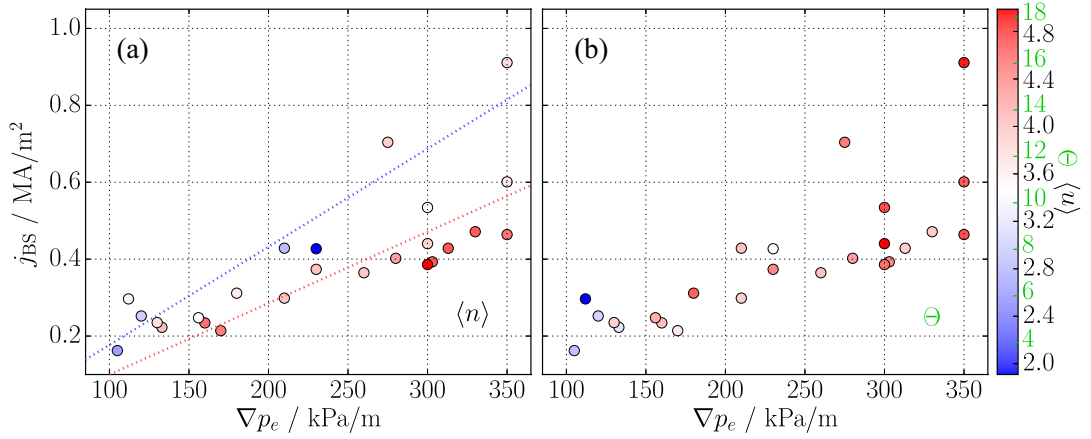


Figure 7.6.: Bootstrap current density maximum j_{BS} against the pressure gradient maximum ∇p . Color coded are from blue to red (a) the average $\langle n \rangle$ during the ELM crash and (b) the balloonedness Θ .

that higher pressure gradients cause higher $\langle n \rangle$ and higher bootstrap current. Nevertheless, bluish points are by trend more on the upper part, whereas reddish points are in the lower, as suggested by the dashed lines that guide the eye. From there it could be stated that bootstrap current indeed reduces $\langle n \rangle$ but as higher bootstrap current is connected with higher pressure gradient, the gradient effect dominates.

Up to now only the effects of parameters on $\langle n \rangle$ were investigated. As ballooning modes should also be poloidally asymmetric such an asymmetry parameter should also scale with the previously discussed parameters q_{95} , ∇q , s , n_e and ∇p , which is investigated in the following.

7.2.2. Poloidal Structure of the ELM Crash

The exact poloidal structure in terms of mode numbers m is not accessible during the ELM crash from magnetics as the equilibrium has high uncertainties. However, an easily determinable measure for the poloidal structure is the here defined balloonedness Θ , measuring the ratio of magnetic intensity on LFS to HFS during the crash. Its origin is twofold. The first possibility is that a mode intensity is stronger on the LFS compared to the HFS, i.e. it is ballooned. The second possibility is that the mode has a longer distance to the HFS coils compared to LFS, as the magnetic fluctuation amplitude drops with distance. Therefore, the value of the previously defined intensity ratio due to plasma position I_{pos} needs to be taken into account in this discussion as well.

As a connection to the last subsection, figure 7.6 (b) shows the maximum bootstrap current density j_{BS} against the maximum electron pressure gradient ∇p . Now the color coded

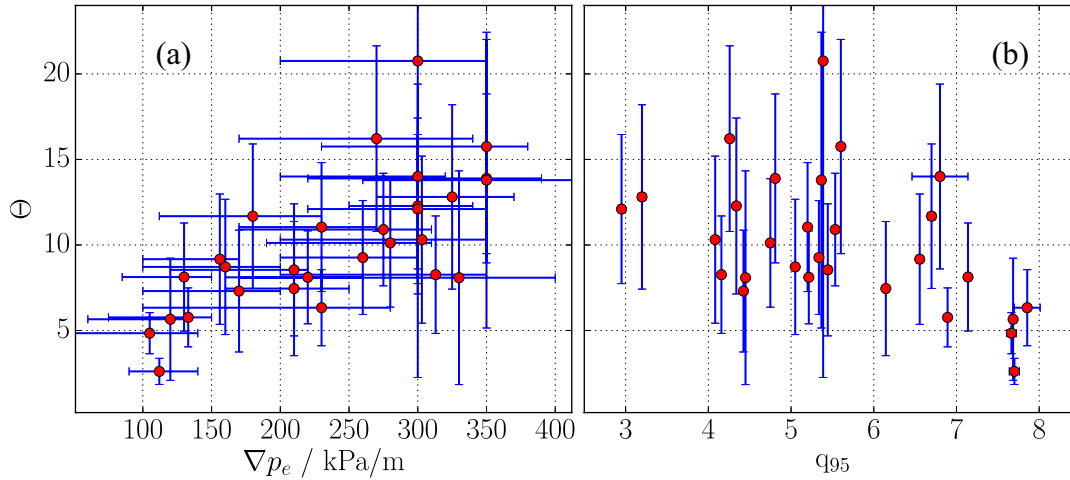


Figure 7.7.: Balloonedness Θ against (a) the maximum pressure gradient and (b) the edge safety factor q_{95} .

quantity is the balloonedness Θ . The plot shows again that j and ∇p are strongly coupled but now no additional influence of j on the balloonedness can be seen. The plot suggests that the asymmetry increases with the gradient but the current plays only a minor role. This behavior of the balloonedness is also shown in more detail in figure 7.7. Here the balloonedness is plotted against (a) the maximum pressure gradient and (b) the edge safety factor. Both parameters seem to influence the measured balloonedness during the crash contrarily. This is also reflected by the correlation coefficients $c_P = 0.71$ and $c_P = -0.48$, respectively. It is seen that Θ and thereby the magnetic intensity measured on the LFS during the ELM crash increases with maximum pressure gradient. As the pressure gradient is the driving parameter for ballooning modes, this is in line with expectations from linear peeling-ballooning theory. On the other hand, ballooning modes are stabilized by magnetic shear and therefore the ELM crash should be less asymmetric for higher edge safety factors, which is also supported by the experimental investigations, although the correlation is again weak.

After finding a positive correlation of Θ with ∇p a further investigation of I_{pos} is especially important as higher pressure gradients also shift the plasma center further out due to the Shafranov shift [28]. While the position control system of AUG keeps the separatrix position R_{out} nearly constant on the LFS, the plasma HFS separatrix position R_{in} is moved. From there it is obvious that the balloonedness increases with pressure gradient, because of increasing I_{pos} , which is shown in Figure 7.8 (a). The question is whether then the dominant influence on the balloonedness parameter is that modes are more ballooned with pressure gradient or that the plasma is moved radially. Figure 7.8 (b) shows both

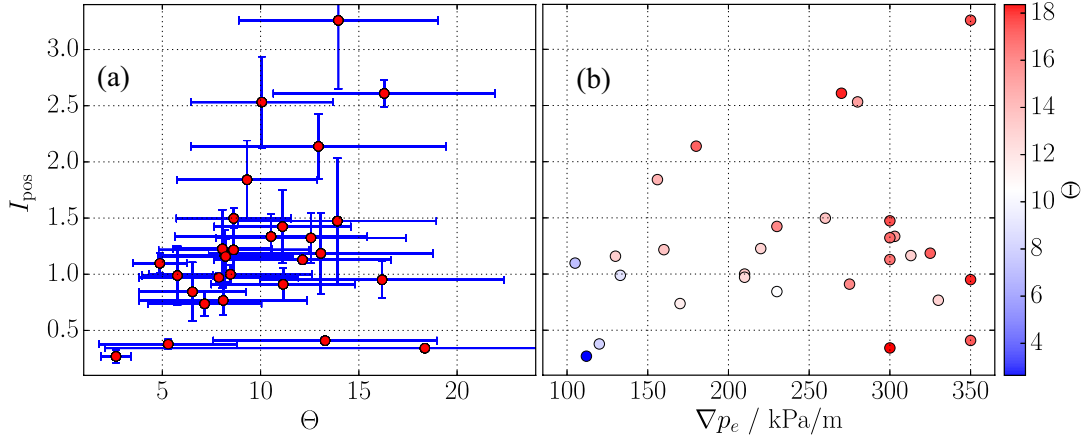


Figure 7.8.: Relative expected intensity due to plasma position against (a) the balloonedness Θ and (b) the maximum electron pressure gradient ∇p with Θ color coded increasing from blue to red.

parameters with Θ increasing from blue to red. Indeed it can be seen that both parameters influence the balloonedness. Lowest Θ values are found on the lower left corner of the plot with low I_{pos} and low pressure gradient, whereas high values appear in the upper right. Nevertheless, investigating groups of discharges with similar I_{pos} can still vary strongly in Θ , which is mainly due to the pressure gradient. From there the conclusion can be drawn that the balloonedness parameter is influenced by the position and not only the ballooning of modes, but the dominating parameter is the pressure gradient which causes a asymmetric mode.

The only other two parameter that also show some correlation to balloonedness is pedestal top temperature T_e and β with $c_P = 0.55$ and 0.57 . Both of the correlations, however, go in line with the maximum pressure gradient.

Summarizing the obtained results for the structure of the ELM crash yields that the peeling-ballooning relevant parameters such as α , s , δ or j_{BS} barely influence the structure of the ELM crash. However, the result that $\langle n \rangle$ varies strongly with edge safety factor and ∇q is very robust. In the following an intuitive geometrical explanation for this behavior is given. The basic idea of the model is that the ELM crash as a mixture of peeling and ballooning modes is driven in the whole region of the pedestal gradients, but a strong ∇q hampers the existence of a broad (low n) pedestal filling structure.

Figure 7.9 visualizes the effect of edge safety factor and magnetic shear on mode structures. The bottom plots show realistic artificial q profiles and according ∇q and s profiles in arbitrary units. The two types of profiles visualized here have (a,b) low $q_{95} = 3.2$ and (d,e) high $q_{95} = 7.0$, similar to the experimental cases shown in figure 7.1. From the bottom

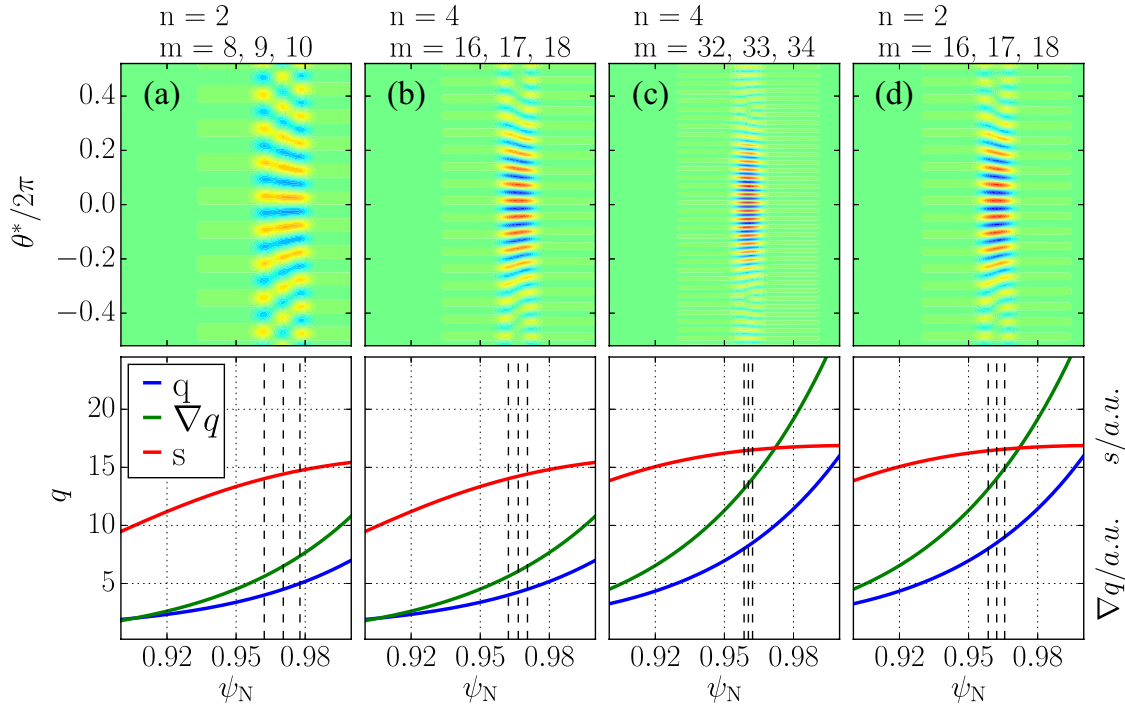


Figure 7.9.: (Top) Artificial mode structures in the θ^*/ψ_N plane for (bottom) two different q , ∇q and s profiles: (a,b) weak shear with $q_{95} = 3.2$ and (c,d) stronger shear with $q_{95} = 7.0$

plots it can be seen that the s parameter does not vary a lot although q and ∇q are about doubled, similar as in the previously presented data set. The top plots show compositions of artificial mode structures in the θ^*/ψ_N plane of the edge region³. Each composition consists of three modes on rational surfaces $q = m/n$ with one n but different m values, given on the top of the plots. The different positions of the mode compositions are sketched with black dashed lines in the profile plots.

Ballooning modes can be interpreted as an overlap of several close by mode structures that interfere such that they have an increased amplitude in the bad curvature region. Figure 7.9 (a) shows a composition of such modes with $n = 2$ at the $q = 4, 4.5$ and 5 surface⁴. Due to the low q shear they are too far apart in order to interact. Furthermore, such a broad structure might be torn apart by the $E \times B$ velocity shear. Therefore, it is unlikely that such a low n composition exists in this region for a low q profile. The first idea of the geometrical model is therefore that the modes need to be close enough to interfere. Figure 7.9 (b) shows $n = 4$ modes, which lead to a ballooned structure in the

³Here the normalized flux $\psi_N = \rho^2$ is used as q_{95} refers to 95% of the flux.

⁴In this region there are no closer rational surfaces for $n = 2$ as Δm of the modes cannot be smaller than $\Delta m = 1$.

LFS region. The interaction of modes is possible because the rational surfaces are close enough together at $q = 4, 4.25$ and 4.5 . Figure 7.9 (c) also shows $n = 4$ modes but in the steeper q profile. The modes in the same plasma region now have higher q values of $q = 8, 8.25$ and 8.5 and are closer together as also ∇q is higher, which leads to narrower ballooning mode. However, with the steeper q profile also $n = 2$ modes, figure 7.9 (d)⁵, can be close enough to interfere at $q = 8, 8.5$ and 9.0 . From there it is clear that there are two possibilities in order to obtain ballooned modes. Either n or ∇q is high enough. However, the experiments showed that no high n appeared at all during the ELM crash. Similarly, also the nonlinear modeling showed that modes couple to form low n structures. From this observation it seems that the ELM crash modes are most unstable with minimized n , meaning larger structures. In the context of plasma turbulence this effect of a transition to larger structure sizes is known as inverse cascading [147–149]. In the frame of MHD this is explained by the mode minimizing the energy of the system by influencing the broadest possible region of the pedestal gradients. Assuming now that the crash modes show such an inverse cascading and minimize n , the mode in figure 7.9 (c) would not exist, because also the $n = 2$ components are close enough to interact within the steep q profile, but have lower n . This is exactly what is seen in the experiment. If q_{95} and thereby ∇q is high, lower n are observed, whereas higher n are found at low q_{95} . This concept of minimizing n can also be formulated such that the ELM crash modes always show up with the same dominant m structures regardless of the q profile, which is exactly the case in figures 7.9 (b) and (d). Summarizing the basic concepts of the geometrical model yields:

- ELM crash modes need several harmonics in order to be ballooned
- Harmonics need to be close enough in order to interact
- Modes minimize n and thereby keep $m = nq$ about constant

In the next section it is shown, that these findings on the ELM crash structure scaling with q_{95} might even also determine the duration of the ELM crash.

7.3. Influence of Plasma Parameters on the ELM Duration and Intensity

As the heat load of the ELM on the divertor plates might be a critical issue for future fusion devices, it is also interesting to characterize the ELMs in terms of energy losses, duration and intensity. As the obtained data base delivers a big variation of plasma

⁵The mode composition of figure 7.9 (d) is also shown on the cover page in the torus geometry.

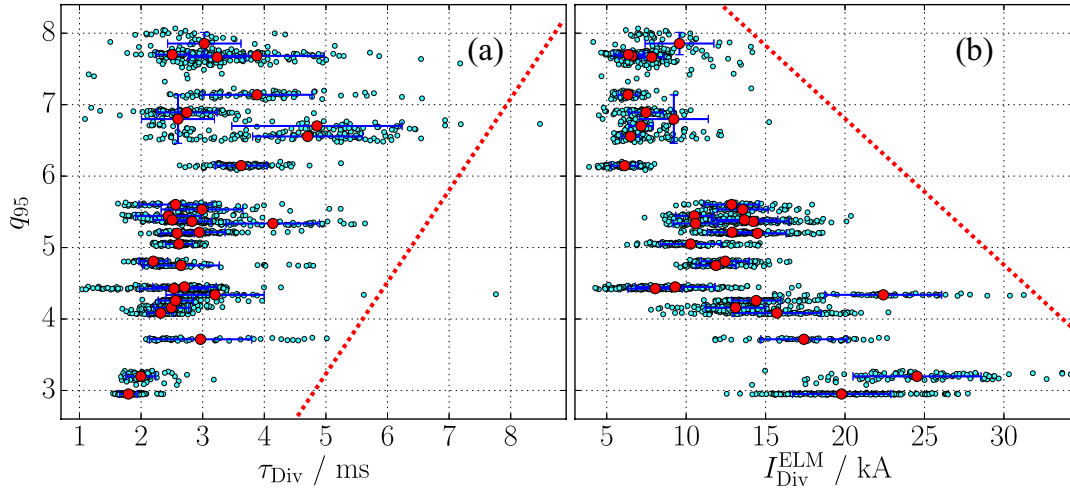


Figure 7.10.: Edge safety factor q_{95} against (a) the duration of the ELM and (b) the maximum intensity of the ELM. Both quantities duration and intensity are measured from divertor shunt current. Red dashed lines mark the parameter space beyond which almost none of the ELMs appear.

parameters on AUG, it can also be investigated what influences these ELM losses.

From table 7.1 it can be concluded that the ELM intensity $I_{\text{Div}}^{\text{ELM}}$ and absolute ELM energy losses ΔW_{MHD} scale with the pedestal parameters such as density, temperature, pressure gradient and thereby also with plasma current and the balloonedness. On the other hand they inversely scale with toroidal magnetic field and ∇q . The duration τ_{Div} and relative ELM losses ΔW_{MHD} , meaning the ratio of losses to the total stored energy, scale basically the other way round. They decrease with pedestal parameters and increase with safety factor.

Figure 7.10 shows how (a) the ELM duration and (b) the ELM intensity measured in the divertor shunt current scale with edge safety factor for the investigated 30 discharges. Shown are not only the mean and the standard deviation with red dots and blue error bars, respectively, but also data for all ELMs (cyan). This is necessary as the data for ELM length and intensity in some cases do not at all follow Gaussian distributions within a discharge. For example there can be discharges containing a group of very short ELMs and a group of very long ELMs. From the data it can be seen that the q_{95} sets an upper boundary for ELM duration and intensity. At high q_{95} ELM durations cover a wide range up to 7 ms, but they then appear with low intensities in the divertor. Similarly, at low q_{95} the intensity can appear in a wide range but then the duration is very limited.

Similar investigations on the JET tokamak found that the ELM length scales inversely with the pedestal parameters, namely the pedestal energy [150]. On the other hand it was stated that pedestal collisionality influences the ELM length in a sense that a higher

collisionality increases the ELM length. Triangularity did not show a strong impact on ELM duration or ELM losses. Furthermore, investigations on different machines found that the peak energy fluence, which is comparable to the here defined intensity, scaled with pedestal density and temperature [151]. This result fits to the here found scaling with q_{95} as the low q_{95} discharges have usually higher pedestal top pressures.

The correlations of ELM length with pedestal parameters such as density and pressure gradient are indeed similar in the here investigated data base. The correlation with temperature (and thereby collisionality) is very weak. The trend, however, is the other way round. A higher pedestal temperature is connected to longer ELM crashes. Furthermore no correlation and no clear trend with triangularity is found for the ELM duration. An explanation why the transport events are shorter or longer was not found in previous publications. Therefore, the finding that the edge safety factor might play a major role, is a big step forward in the understanding of the ELM. From this observation one possible explanation for the ELM length could be that ELMs of high q_{95} plasmas just influence broader regions of the plasma. This would also be in line with the fact that a strong ∇q reduces $\langle n \rangle$ and thereby increases the structure size, as seen in the previous sections. This influence of broader regions of the ELM with higher edge safety factor is also experimentally observed in the propagation distance of cold pulses which are induced by ELM crashes [152].

Another approach for explaining the ELM duration could be drawn from the pedestal parameters, namely ∇p . Previous studies showed that the radial electric field being responsible for the edge rotation and thereby the edge transport barrier in H-Mode is mainly neoclassically driven and therefore proportional to the ion pressure gradient divided by density $\nabla p_i/n_e$ [24]. Furthermore, a certain radial electric field of about 15 kV/m is needed in order to maintain the H-mode. Recent findings showed that the radial electric field drops down to similar values and below during the ELM crash [110]. From there the speculative hypothesis is that the crash length is due to the plasma going into L-mode, during which the transport is high, and taking several milliseconds until going back to H-mode by restoring ∇p_i and thereby electric field and edge rotation. If now the plasma has a higher pressure gradient, the radial electric field might not drop drastically below the 15 kV/m and therefore gets faster back into the H-mode, which makes the crash shorter.

In order to clarify whether the mode structure or the pedestal parameters determine the ELM duration further investigations taking into account also the ion pressure gradient are needed. The ELM intensity, on the other hand, seems to be only a result of how much energy was stored in the pedestal prior to the crash.

7.4. Summary and Outlook

The influence of plasma parameters on toroidal and poloidal structure as well as duration and intensity of the ELM crash was investigated with a data base of 30 discharges with more than 2500 ELMs.

The toroidal structure of the ELM crash is strongly influenced by the edge safety factor q_{95} , i.e. higher average toroidal mode numbers $\langle n \rangle$ appear during the crash for lower q and thereby lower ∇q cases. This effect can, however, not be separated from the influence of the plasma current which increases $\langle n \rangle$ accordingly. To entangle both effects future experiments which vary the toroidal magnetic field would be necessary. Nevertheless, an intuitive geometrical model was proposed that shows that lower ∇q values need higher toroidal mode numbers in order to have close enough structures for interaction. This sets a lower boundary for the n numbers that are in general minimized during the crash in order to influence a broader region.

Other parameters such as pressure gradient, bootstrap current density or triangularity have a weaker influence on the toroidal geometry. All investigated parameters also influence the n number of low frequency ELM precursors in a very similar way as the n number during the crash. Therefore both phenomena (crash and precursor) appear with similar n .

The influence of parameters on the here defined balloonedness of the crash is manifold, but the pressure gradient and edge safety factor show the strongest correlation, which is in line with linear peeling-ballooning theory.

ELM duration and intensity are influenced in opposite ways. Higher pedestal energy results in stronger ELMs and thereby higher intensities in divertor shunt current measurements. On the other hand discharges with higher pedestal energy by trend have higher current and thereby reduced q_{95} values. A reduced q_{95} and thereby ∇q decreases structure size (increases n) and penetration depth which might be responsible for the shorter ELMs.

8. Toroidal Mode Numbers of Various Operation Scenarios

Previous chapters discussed mainly the structure of ELMs in various H-mode scenarios of AUG plasmas. In this chapter different other scenarios containing either ELM-like events or ELMs under different conditions are investigated, i.e. ELM-like bursts of the intermediate phase (I-phase), a plasma containing nitrogen, a plasma perturbed by additional magnetic error fields and an ELMy H-mode scenario at the JET tokamak.

8.1. I-phase Bursts

Increasing heating power in low confinement (L-mode) discharges leads to transitions to the H-mode with higher confinement and strong regular bursts from edge localized modes. However, various experiments also reported on an intermediate regime that appears close to the L-H-transition [153–155]. This regime carries properties of both H- and L-mode plasma, which is why it is called intermediate phase (I-phase). The I-phase has, similar to H-mode, increased particle and energy confinement, increased edge flow and a pronounced pedestal, although weaker than H-mode pedestals. Furthermore, bursts that govern the edge plasma region appear during the I-phase. These bursts appear with much higher frequency (1–4 kHz) than typical ELM bursts [156]. As these bursts do not show a sinusoidal pulse shape the I-phase had been associated with limit cycle oscillations, likewise to oscillations obtained from predator-prey type oscillations [157]. However, it is not yet fully clarified whether a phase shift, characteristic for limit cycle oscillations, between different quantities such as poloidal flow and density can be detected [158, 159]. In addition to that, it was reported that increasing heating power during I-phases leads to a continuous transition of these burst to type-III edge localized modes [153].

Figure 8.1 shows the signal of a magnetic pick-up coil and its spectrum. The coil measures the radial magnetic field fluctuations at the outboard midplane during such an I-phase on ASDEX Upgrade, with constant ECRH power of $P_{\text{ECRH}} = 0.5 \text{ MW}$, a line averaged core and edge electron density of 4.8 and $2.8 \cdot 10^{19} \text{ m}^{-3}$, respectively, plasma current $I_p = 0.8 \text{ MA}$,

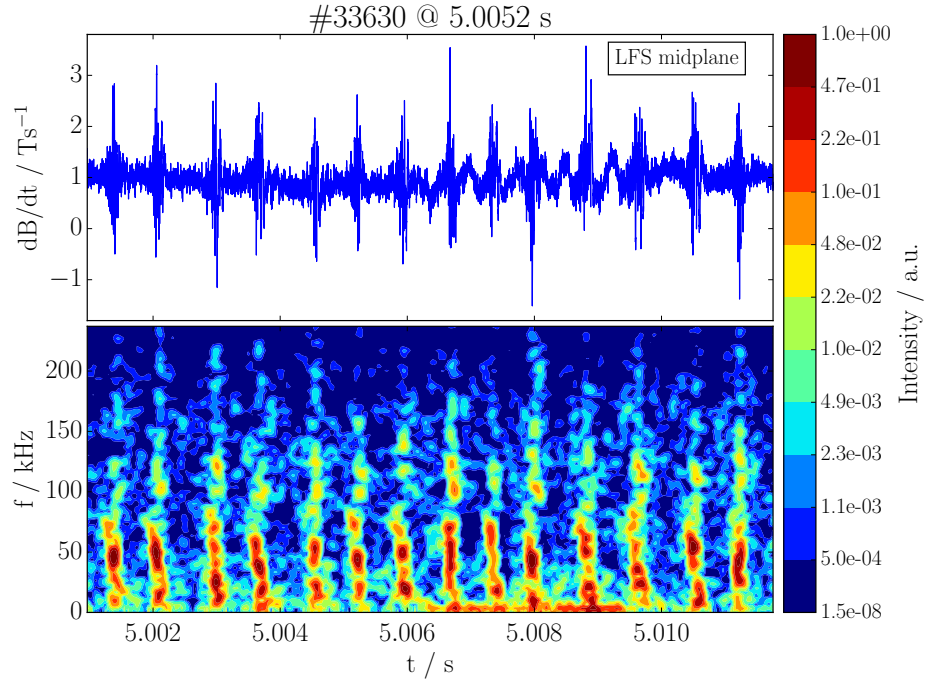


Figure 8.1.: Signal (top) of a magnetic pick-up coil at LFS midplane during an I-phase and its spectrum (bottom). Both show the I-phase characteristic bursts.

toroidal magnetic field $B_t = 2.5 \text{ T}$, edge safety factor $q_{95} = 4.8$ and plasma stored energy $W_{\text{MHD}} = 130 \text{ kJ}$. Clearly visible in the figure are the described bursts with a repetition rate of about 1.4 kHz . These bursts are not only visible in magnetics but also in temperature or density probing diagnostics. The similarity of these bursts to the crashes of edge localized modes triggers the question, whether also the magnetic structure visible at the LFS midplane is similar to the ones seen during ELMs. Figure 8.2 (a) shows a spectrum of a LFS midplane coil signal but now synchronized to the onsets of 20 such edge localized I-phase bursts. From this figure it can only be stated that the bursts appear similarly to ELM crashes with a broad spread in frequency but with dominant frequencies up to 75 kHz , which is much higher than the dominant frequencies during ELM crashes. However the higher frequencies of $30\text{--}75 \text{ kHz}$ seem to appear a bit earlier and are therefore often considered as precursors.

Figure 8.2 (b) shows a mode number spectrum calculated from the 20 time windows during the I-phase burst. All windows have a 0.7 ms duration in order to have enough frequency

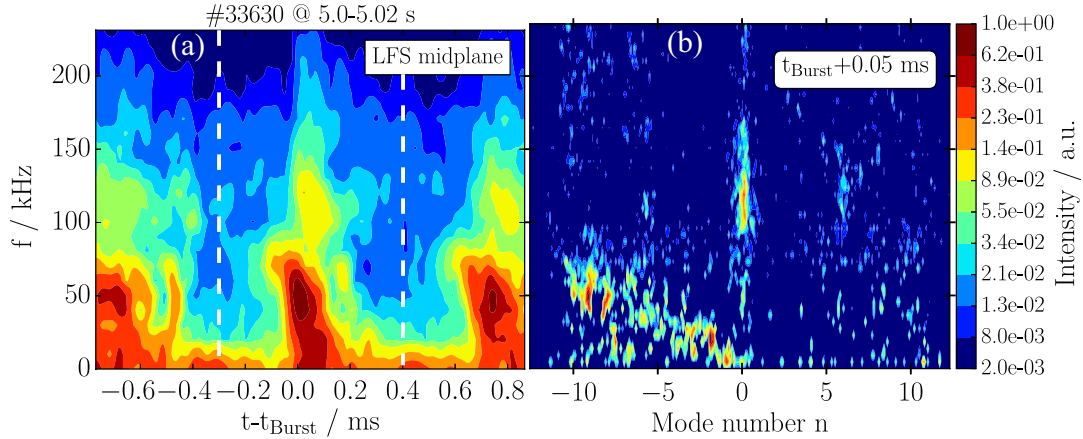


Figure 8.2.: (a) Frequency spectrum synchronized to the onset of 20 I-phase bursts and (b) mode number spectrum evaluated during the 20 I-phase bursts in the 0.7 ms window marked by white dashed lines in (a).

resolution. The investigated frame is also marked in (a) with white dashed lines. From the mode number spectrum it can be clearly seen that the structure during the crash has three dominant contributions. In the low frequency range $n = -2$ and $n = -8, -9$ contributions rotating in electron diamagnetic drift direction are dominant, whereas at higher frequencies an $n = 0$ oscillation is present. This mode number spectrum looks almost the same as the ones obtained during the ELM crash, see section 5.1.6 and 6.2. The main difference for the I-phase bursts is that additional high $n = 8, 9$ contributions also exist during the burst even for this comparatively high edge safety factor $q_{95} = 4.8$, which typically cause only $n = 2-5$ structures during edge localized modes in H-modes, see section 7.2. However, as the $n = 8, 9$ components set in slightly earlier, they might also be interpreted as a precursor and not as a part of the crash itself. The additional $n = 0$ component with higher frequencies $f = 90-130$ kHz is comparable to the ones appearing during ELMs and its origin still remains an open question. However, appearance of $n = 0$ geodesic acoustic modes (GAMs) during such limit cycle oscillations is sometimes considered as one of their main features [154]. Usually these GAMs appear with low frequency around 10 kHz. Nevertheless as proposed by *Manz et al.* there should also exist an $n = 0, m \neq 0$ geodesic branch called the geodesic Alfvénic mode which might appear with such high frequencies, although only studied in plasmas diverted in the plasma top region [114]. From these results it can be seen that the I-phase bursts have a decent magnetic structure which is practically the same as the one of type-I ELMs. This opens up the question whether I-mode bursts are only small type-III edge localized mode crashes as concluded in [156].

8.2. Nitrogen Seeded ELMs

Injection of impurities into tokamak plasmas is a common strategy to avoid high heat loads onto divertor target plates by radiative cooling, which might be necessary for future fusion devices [160]. One typically used impurity is nitrogen. Although counter intuitive, as radiative losses increase, nitrogen has the advantage that it even improves the confinement [150, 161]. It was found that an increased edge stability due to the inward shift of the edge pressure profile [44] leads to higher pedestal temperature and via stiff temperature profiles to improved plasma performance. However, nitrogen seeding also influences the ELM crash quite dramatically in terms of ELM duration and ELM losses, i.e. relative ELM losses are reduced and ELMs become shorter [150, 162]. From these findings it was concluded that the ELM crash itself consists of several phases or events. Later phases are then suppressed by the nitrogen.

As presented in the previous chapter, the ELM duration and losses are influenced by the edge safety factor. Furthermore, the edge safety factor is linked to the toroidal structure of the ELM. From this linkage of duration to toroidal structure the question arises whether the toroidal structure of the ELM also changes when the plasma is nitrogen seeded.

Figure 8.3 shows time traces of radial magnetic fluctuations measured at the outboard midplane, divertor shunt current, ELM frequency, plasma stored energy and core and edge density with and without nitrogen seeding. Furthermore, the n spectra for both cases calculated from 70 and 65 ELM crashes, respectively. From the time traces one can see that the intensity of the crashes in both cases are similar in magnetics and divertor shunt current. However, the duration of the crashes is shorter in the nitrogen seeded scenario. The ELM frequency is on average the same in both cases, but has higher fluctuations in the nitrogen case. ELM losses are also similar, but as the plasma stored energy is slightly higher in the nitrogen seeded case, the relative losses reduce slightly. Furthermore, the line integrated density is comparable in both cases.

The mode numbers of the ELM crashes obtained from averaging over all ELMs within the two discharge phases give very similar results. Both types of crashes are dominated by $n = 3-5$ modes. Nevertheless, for the unseeded case additional weaker $n = 2$ and $n = 7$ components are detectable. Furthermore, the unseeded case has a slightly visible second mode branch during the crash (white dashed line). Such a second branch seems to be not present in the nitrogen seed case.

From the here investigated mode numbers present during the crash no conclusive statement could be drawn on the origin of the ELM shortening by nitrogen, as the toroidal ELM structure does not change strongly with nitrogen seeding. This again supports the statement made in the previous chapter that the ELM structure is mainly a result of the edge safety

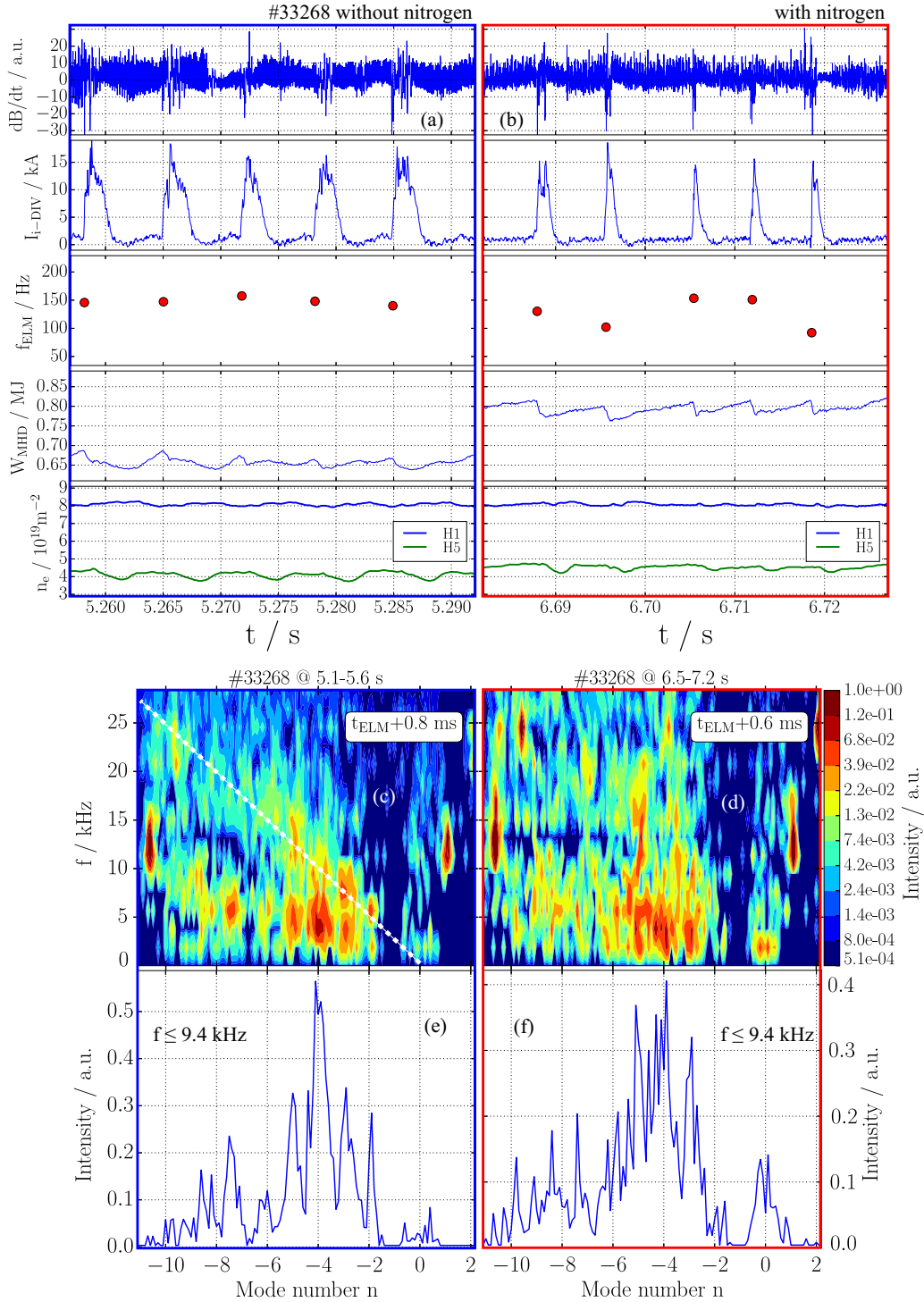


Figure 8.3.: Time traces of (top to bottom) magnetic fluctuations, divertor shunt current, ELM frequency, plasma stored energy, line averaged density in the core (H1) and the edge (H5) for discharge phases (a) without nitrogen seeding (b) with nitrogen seeding. $f-n$ spectra of (c) 65 ELM crashes without nitrogen seeding and (d) 70 ELM crashes with nitrogen seeding taken within one discharge and (e) and (f) the according n spectra.

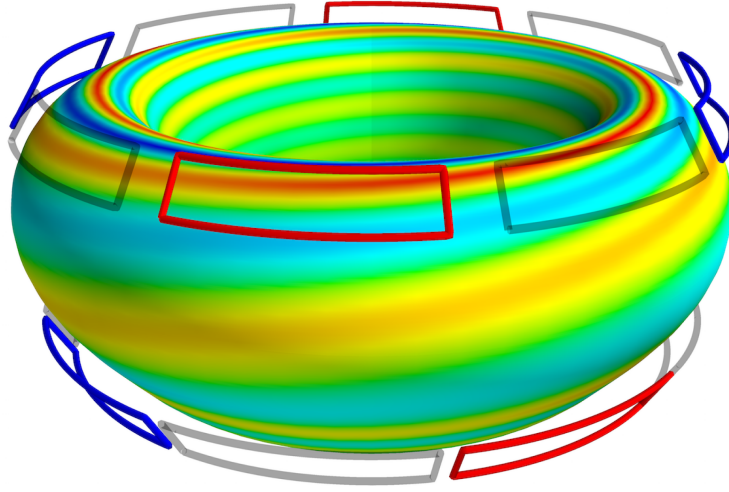


Figure 8.4.: Plasma displacement ξ due to a field aligned kink mode on ASDEX Upgrade excited by the the perturbation fields from the sketched magnetic perturbation coils [166]. Colors of the coils indicate the different possible direction of the generated radial magnetic perturbation, i.e. outwards (red), inwards (blue) or zero (grey).

factor, which is about $q_{95} = 4.0$ in both cases, fitting again very well to the data shown in figure 7.3. However, as a second mode branch appears in the case without nitrogen, the reason for having longer ELMs might be that a wider area of the pedestal is ergodized from the ELM, which might be investigated in more detail in further experiments.

8.3. ELMs with Magnetic Perturbations

Various worldwide tokamaks investigate the effects of externally applied non-axisymmetric magnetic error fields onto the plasma [163–165]. These radial error fields are created by additional coils, which are (in case of ASDEX Upgrade) mounted close to the plasma. As they perturb the field geometry of the plasma they are called magnetic perturbation (MP) coils.

Figure 8.4 shows the radial plasma displacement ξ due to a field aligned kink mode in AUG that is excited by the perturbation fields from the sketched MP coils. The MP coils are arranged in two rows containing eight coils each. The colors of the coils indicate that the current direction in the coils can be chosen such that the plasma gets perturbed radially inwards or outwards with variable amplitude. Thereby a sinusoidal perturbation structure can be applied to the plasma characterized by a toroidal periodicity n_{MP} . Such a perturbation might then be aligned to the unperturbed field geometry at a certain position in the plasma, i.e. they are in resonance.

The reason for inducing such a perturbation is that ELMs can be mitigated or even suppressed [163, 165]. The theories supporting such an ELM suppression or mitigation are manifold but partially incomplete [167, 168]. Therefore, it is only investigated here whether there are changes in the toroidal geometry of edge localized modes when external error fields are applied. The further interpretation of these results and their implications can only be speculative.

Figure 8.5 shows time traces within one discharge of radial magnetic fluctuations measured at the outboard midplane, divertor shunt current, ELM frequency, plasma stored energy and core and edge density with and without (right and left) slowly rotating $n_{\text{MP}} = 2$ error fields from MP coils. Furthermore, the mode number spectra for both cases calculated from 15 ELM crashes are shown. From the time traces one can see that the intensity of the ELM crashes in the MP coil case is reduced in magnetics and divertor shunt current, i.e. the ELMs are mitigated. Also the ELM frequency is strongly reduced. The energy losses on the other hand are similar. Also the line integrated densities are comparable in both cases, which is typically not the case for ELM suppressed scenarios, where a strong pump out of density occurs.

The mode numbers of the ELM crashes obtained from averaging over all ELMs within the two discharge phases are slightly different. In both cases the crashes are dominated by modes with $n = 2, 3$. The case without MP coils has additional weaker activity at $n = 4$ and maybe higher n . The ELM crashes during $n_{\text{MP}} = 2$ magnetic perturbations do not have this weaker higher n activity. This reduction of average mode numbers raises the question whether the q values are changed. This is indeed the case, i.e. $q_{95,0} = 4.8$ and $q_{95,\text{MP}} = 4.85$, but not as strong as it would be required for having a change in mode numbers of about $\Delta n = 1$. Another possibility could be that the $n_{\text{MP}} = 2$ perturbation imprints its structure more directly onto the crash. For the here presented case this might be an explanation. Other scenarios with $n_{\text{MP}} = 1$ perturbations, however, also enhanced the $n = 2$ component of the crash and not the $n = 1$ component, which weakens this hypothesis.

All in all the few cases investigated in this frame show that the MP coils indeed influence the crash in terms of toroidal structure. Whether the impact of the coils is of a direct nature or whether other plasma parameters are varied first and then the ELM crashes change cannot be concluded. Therefore, an extension of a data base containing various MP coil configurations and the mode number distributions during the crash might be a way to go for future investigations. Another investigation could aim for studying the high frequency fluctuations appearing between ELMs, which might also be influenced by MPs, although a direct influence is unlikely as they rotate too fast for intense coupling to the error fields.

8. Toroidal Mode Numbers of Various Operation Scenarios

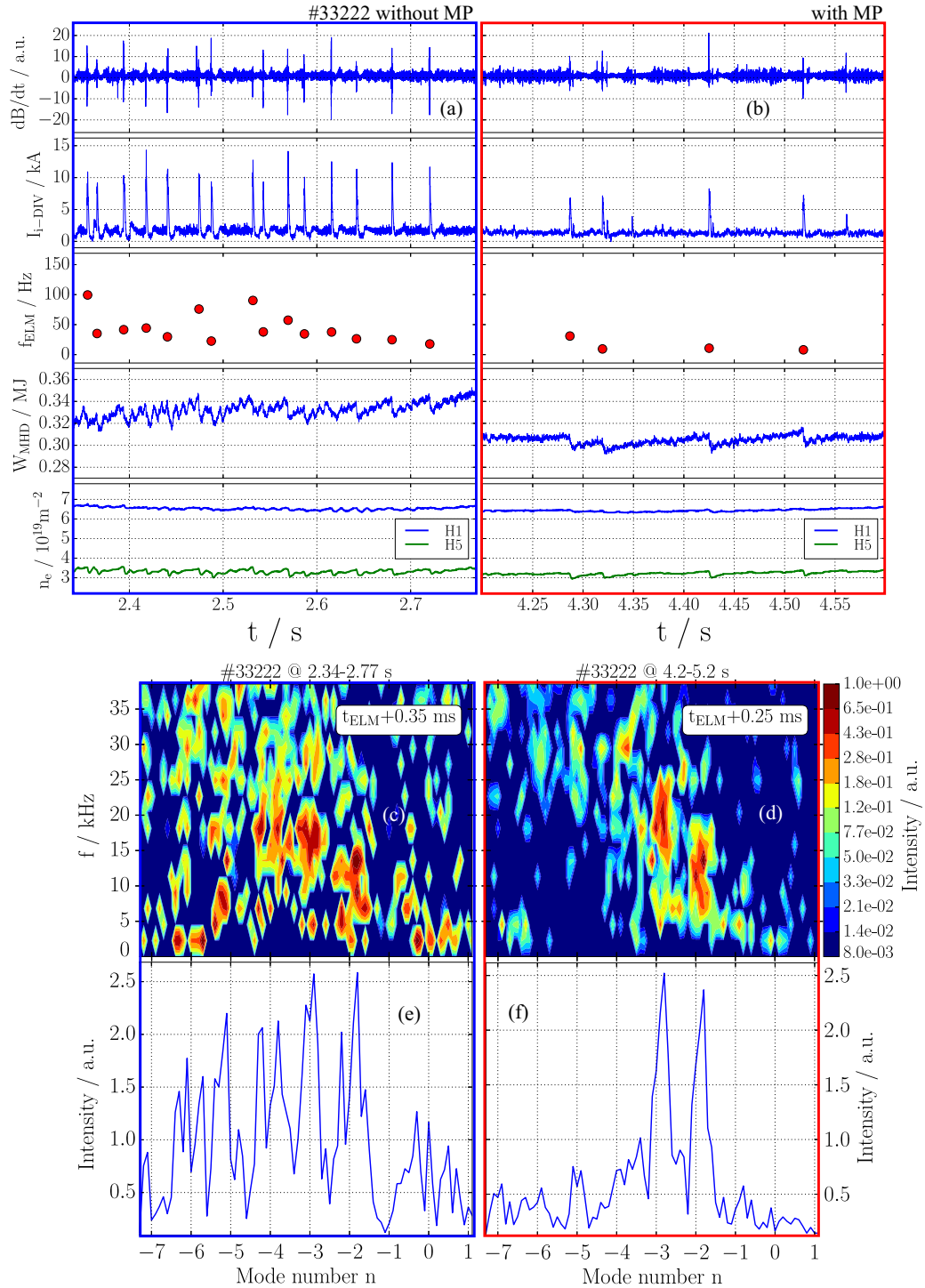


Figure 8.5.: Time traces of (top to bottom) magnetic fluctuations, divertor shunt current, ELM frequency, plasma stored energy, line averaged density in the core (H1) and the edge (H5) for discharge phases (a) without MP coils (b) with MP coils. f - n spectra of (c) 15 ELM crashes without MP coils and (d) 15 ELM crashes with MP coils and (e) and (f) the according n spectra.

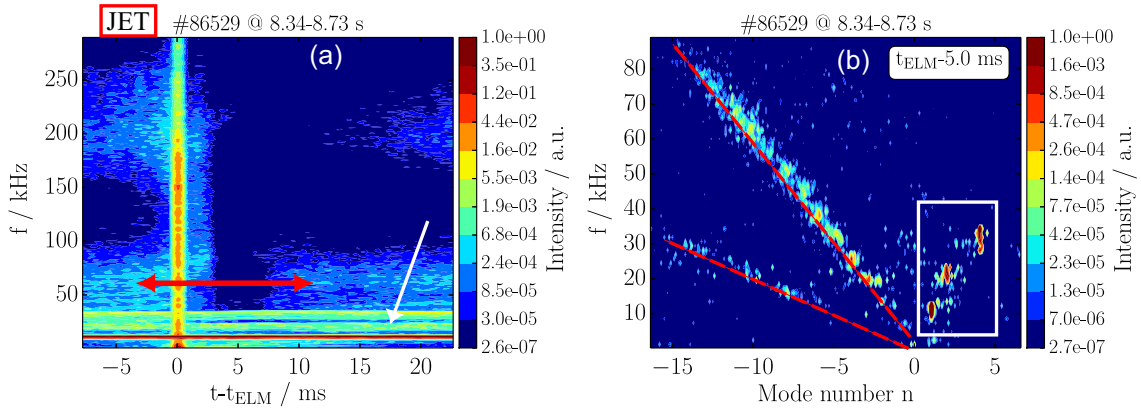


Figure 8.6.: (a) Frequency spectrum synchronized to the onset of 8 ELMs measured in a JET plasma and (b) n spectrum evaluated during the phases 5 ms before the 8 ELM in a 2.0 ms window. Mode numbers in the white box and mode numbers following red dashed lines correspond to core modes and ELM Cycle relevant edge oscillation marked by white and red arrow in (a).

8.4. ELMs at the JET Tokamak

The Joint European Torus (JET) is the up to now largest tokamak with a major radius of 3.0 m and minor radius of 0.9 m situated in Culham, United Kingdom. It is operated with a tungsten divertor and beryllium wall. The installed heating systems are 34 MW NBI and 17 MW wave heating. Furthermore, magnetic field and plasma current can be up to 4 T and 5 MA, respectively [169].

As JET has a unique size and the opportunity of tritium operation it is best suited for scenario development for future fusion devices like ITER. As ITER will operate in H-mode, ELMs are one substantial field of research in JET. The here investigated scenario is an example of several ELM cycles within one discharge on JET. The obtained results are then compared to the results obtained on AUG ELM cycles.

Figure 8.6 (a) shows a spectrum obtained from poloidal magnetic pick-up coils at the JET tokamak. The spectrum is synchronized to the onset of eight ELMs within a discharge phase with 17 MW NBI heating power, a plasma current of 2 MA, a magnetic field of 1.95 T, line integrated core and edge densities of about 14 and $4.5 \cdot 10^{19} \text{ m}^{-2}$, respectively, a plasma stored energy around 3.8 MJ and an edge safety factor of $q_{95} = 2.9$. Furthermore, figure 8.6 (b) shows an n spectrum of a time interval 5 ms before the ELM onsets. At that time, clear mode structures are visible in three frequency ranges similar to the phases III and IV presented in section 5.1 on AUG. These are first of all core mode structures with

$n = 1, 2$ and 4 and frequencies of $f = 10, 20$ and 32 kHz. Secondly, a high frequency branch with frequencies $f = 150$ – 250 kHz is present. The mode numbers of these fluctuations are too high to be determined, which is also due to the fact that the spacing of JET pick-up coils for determining mode numbers is larger than in AUG. Finally, medium frequency fluctuations with $f = 10$ – 80 kHz are present. The mode number spectrum shows, similar to the AUG fluctuations between ELM crashes, that several branches of modes appear. Mode numbers are, however, slightly higher for this JET case than for usual AUG discharges, i.e. $n = -(3-12)$, but they also propagate in electron diamagnetic drift direction. Another feature of these modes that was also discovered on AUG discharges is that they disappear completely after the ELM crash. Then the low frequency branch appears first, followed by the high frequencies, which underlines their different origin. During the ELM crash no mode number analysis for the dominant low frequencies is possible with the magnetic pick-up coil system installed at JET. Only the oscillations visible in the spectrum with $f = 90$ – 180 kHz can be determined to be $n = 0$, which could be again interpreted as a geodesic Alfvénic mode.

These obtained results can serve as a starting point for further MHD analysis of the ELM cycle at JET. They show similar features as many ASDEX Upgrade ELM cycles investigated in this thesis, but in order to make a quantitative comparisons between both machines regarding the ELM cycle fluctuations an investigation of all properties such as rotation velocities, position and parameter dependence would be necessary.

8.5. Summary and Conclusion

Various plasma scenarios containing either ELM-like events or ELMs under different conditions were investigated. Properties of these events are very similar to usual type-I ELMs on AUG, i.e. they all have a distinct magnetic mode structure and rotate in electron diamagnetic drift direction. However, the limited number of discharges analyzed within this framework can only show the ability of the magnetics to contribute also to various other fields of research besides ELMs. Nevertheless, results obtained for the I-phase showed that the I-phase bursts are governed by a distinct magnetic mode structure, which is similar to the one obtained during type-I ELM crashes.

9. Summary and Outlook

In this thesis, periodic edge localized modes that appear in high confinement regimes of magnetically confined fusion plasmas were investigated. The main results of chapters 4–8 are summarized and discussed below. An outlook on future perspectives finalizes the thesis.

9.1. Summary and Discussion

Edge localized modes (ELMs) are magnetohydrodynamic (MHD) instabilities. ELMs occur as periodic releases of particles and energy on a millisecond time scale. This periodic behavior defines the ELM cycle including the fast crash event and the comparatively slow recovery of the energy of the plasma edge pedestal. Due to the fast energy releases ELM crashes might cause intolerably high heat fluxes onto the divertor target plates or the first wall in future fusion devices. Therefore, it is necessary to understand the underlying process responsible for ELMs and especially their nonlinear development during the crashes. In this thesis, different phases of the ELM cycle were investigated on the ASDEX Upgrade tokamak (AUG) with special attention on the appearing modes and their spatial magnetic structure as one of the main characterizing parameters.

For the determination of the spatial structure of modes, i.e. the poloidal and toroidal mode numbers m and n as defined in chapter 2.2, recently upgraded poloidal and toroidal arrays of magnetic pick-up coils were used. With the toroidal pick-up coil array installed on ASDEX Upgrade a determination of the toroidal mode number n is reliable at least up to $n = 16$. The poloidal pick-up coil array is best suited to determine poloidal mode numbers m but mainly of edge phenomena. However, it is only reliable under the assumption that the plasma equilibrium is well known and that modes are aligned to the magnetic field lines, i.e. $q = m/n$. The determination of mode numbers at high frequencies is much improved by taking into account the frequency dependent phase response of the coils.

From the co-occurrence of modes with varying spatial structure and changes in the edge profiles at least six clearly separated phases of the ELM cycle could be identified. These are four phases after the ELM crash, the pre-ELM phase and the ELM crash phase itself. These phases appear in a similar manner for each ELM cycle, which makes the method of ELM synchronization a valuable tool in order to get good statistics for mode number

and profile determination. During the first phase after the ELM crash no electromagnetic signal from the edge is visible. In all other phases around the ELM several branches with a variety of mode numbers with $n \leq 13$ but fixed f/n values and thereby propagation velocity are present. This indicates that MHD modes with a complex structure appear at distinct radial positions in the strong velocity gradient region. From a comparison to the edge plasma rotation, from reflectometry measurements and from an estimation of the rational surface $q = m/n$ a localization of the modes was achieved. Fast mode branches with frequencies $f = 200\text{--}250$ kHz and $n = 7\text{--}13$ could be located at position of maximum edge poloidal rotation, where they do not show a phase velocity. These high frequency oscillations vanish in some cases before the ELM crash, indicating that they do not play a direct role for the crash. Slower mode branches with $f \leq 150$ kHz and $n \leq 7$ are likely to be further outwards close to the separatrix, where rotation measurements have too high uncertainties in order to pin down their phase velocity. These modes always precede the ELM crash and clearly increase their intensity in some cases slightly before the crash. It remains unexplained whether they are more directly connected to the crash and maybe even trigger it.

Determination of mode numbers during the ELM crash showed that the dominantly detected low frequency modes have a precise spatial low n structure of typically $n = 2\text{--}7$, similar to the fluctuations preceding the crash. The low frequency during the crash fits to the drop of the poloidal velocity in this phase. Therefore, the ELM crash is interpreted as the breakdown of the plasma rotation combined with the existence of a strong low n mode structure. Furthermore, an $n = 0$ mode structure that starts during the ELM crash and ends during the recovery phase remains unexplained, but it might be connected to the appearance of an $n = 0$ geodesic Alfvénic mode. Any m determination is impossible during the crash because of the lack of a reliable plasma equilibrium.

The structure and other parameters of the crash such as energy losses and duration were compared to results from modeling with the nonlinear MHD code JOREK. In the investigated case the $n = 6$ component is linearly dominant, but nonlinear coupling in which the $n = 1$ component is particularly important leads to the dominance of low $n = 3\text{--}5$ modes during the ELM crash which is in excellent agreement with experimental observations. However, the $n = 1$ component is visible in the experiment only in very rare cases, due to its long wavelength and short life span. Edge stochastization in the modeling is responsible for the fast temperature collapse in the plasma edge due to the fast parallel heat transport, highlighting the role of reconnection for this process during the ELM crash. The connection of the modes preceding the crash to the crash itself could not be discovered by modeling as it starts from unstable conditions, which directly lead to the crash.

The influence of plasma parameters on the toroidal and poloidal structure as well as the

duration and intensity of the ELM crash was investigated with a data base from 30 discharges with more than 2500 ELMs. The toroidal structure of the ELM crash is strongly influenced by the edge safety factor q_{95} , i.e. higher average toroidal mode numbers $\langle n \rangle$ appear during the crash at lower q_{95} and thereby lower ∇q . This effect can, however, not be separated from the influence of the plasma current with which $\langle n \rangle$ increases. However, a simple geometrical model was proposed which shows that lower ∇q need higher toroidal mode numbers in order to maintain similar poloidal structures. This sets a lower boundary for the n numbers that are in general minimized during the crash in order to influence a broader region.. Other parameters such as pressure gradient, bootstrap current density or triangularity, that should have, according to linear peeling-ballooning theory, an impact on the dominant n values, do now show any clear trend. These results might be interpreted in a way that the nonlinear coupling of modes always maximizes the spatial structure of the ELM crash. i.e. minimizes n , and that therefore one certain m structure is dominant regardless of q_{95} .

ELM duration and intensity are influenced in opposite ways. Higher pedestal energy results in more intense ELM crashes. On the other hand discharges with higher pedestal energy are typically at higher plasma current and therefore lower q_{95} . A reduced q_{95} decreases structure size (increases n) and penetration depth which might shorten the ELMs.

Various plasma scenarios containing either ELM like events or ELMs under different conditions were investigated. All of these events have a distinct magnetic mode structure rotating in the electron diamagnetic drift direction. In particular, results obtained for an I-phase showed that I-phase bursts are governed by a explicit magnetic structure, which is similar to the one obtained during type-I ELM crashes. This is consistent with I-phase bursts not being a separated phenomenon, but rather small ELM crashes with a high repetition rate.

9.2. Outlook

In the following, five points that were beyond the scope of this thesis, although being closely related, are brought up for possible future studies.

Comparison to Other Diagnostics

Modes appearing during the ELM cycle or other operation scenarios have been investigated with various types of diagnostics besides magnetics. However, comparing the results on structure, position and rotation in detail with for example reflectometry measurements might yield new insights in the role of these edge modes for the ELM crash.

Nonlinear Modeling with JOREK

As shown in chapter 6, the nonlinear modeling of the ELM crash gives comparable results to what is seen in the experiment. However, the complete ELM cycle including preceding and potentially triggering modes of the crash could not be modeled within this thesis. This is one possible future field of research as well as one-to-one comparisons to diagnostic measurements with a free-boundary extension of JOREK. Furthermore, the role of the q profile for the ELM crash structure, found in chapter 7, could be investigated with modeling.

Other H-mode Similar Scenarios

In chapter 8 various other plasma scenarios besides ELMy H-mode at AUG were investigated, but with a small amount of discharges. Such studies could be further extended in order to confirm the here drawn tendencies. Also the edge modes appearing in scenarios such as the quiescent H-mode without ELMs but improved confinement are well suited to be investigated further with the here presented methods.

L-Mode Transition and Ion Data

In chapter 7 one possible explanation for the duration of the ELM crash was drawn from the hypothesis that the crash causes a transition to the low confinement regime. Investigating this hypothesis further would need an inclusion of ion pressure and temperature data in the provided data base. This was, however, beyond the scope of this thesis, but should be done in the future.

Disentanglement of q and n_e Scaling

The average toroidal structure size of the ELM crash increases with edge safety factor q , as shown in chapter 7. However, as q decreases with current and thereby electron density n_e , the influence of both parameters on the toroidal mode number n could not be disentangled in this thesis. Therefore, discharges with varying q profiles by a variation of the toroidal magnetic field are proposed.

Bibliography

- [1] L. Prados de la Escosura, *Review of Income and Wealth* **61**, 220 (2015). **URL**
- [2] Human Development Report 2016, <http://hdr.undp.org/en/2016-report> (2016), accessed: 2017-10-31.
- [3] P. D. United Nations, *World Population Prospects 2017*, <https://esa.un.org/unpd/wpp/>, accessed: 2017-10-31.
- [4] National Nuclear Data Center, <http://www.nndc.bnl.gov/>, accessed: 2005-07-01.
- [5] H.-S. Bosch and G. Hale, *Nuclear Fusion* **32**, 611 (1992). **URL**
- [6] L. Meitner, O. Hahn, and F. Strassmann, *Zeitschrift für Physik* **106**, 249 (1937). **URL**
- [7] H. A. Bethe, *Phys. Rev.* **55**, 103 (1939). **URL**
- [8] E. G. Adelberger *et al.*, *Rev. Mod. Phys.* **70**, 1265 (1998). **URL**
- [9] S. Atzeni and J. Meyer-ter Vehn, *The Physics of Inertial Fusion* (Clarendon Press, 2004).
- [10] M. Keilhacker *et al.*, *Nuclear Fusion* **39**, 209 (1999). **URL**
- [11] J. Wesson and D. Campbell, *Tokamaks, International series of monographs on physics* (Clarendon Press, 2004).
- [12] ITER web page, <https://www.iter.org/>, accessed: 2017-10-31.
- [13] H. Zohm *et al.*, *Nuclear Fusion* **57**, 086002 (2017). **URL**
- [14] U. Stroth and the ASDEX Upgrade Team, *Nuclear Fusion* **53**, 104003 (2013). **URL**
- [15] H. Zohm for the ASDEX Upgrade Team and the EUROfusion MST1 Team, *Nuclear Fusion* **55**, 104010 (2015). **URL**
- [16] A. Kallenbach and AUG Team, *Nuclear Fusion* **57**, 102015 (2017). **URL**

- [17] H. Zohm and AUG Team, *Nuclear Fusion* **49**, 104009 (2009). **URL**
- [18] J.-M. Noterdaeme et al., *16th IAEA Conference Proceedings Montreal, Canada* (1996), pp. 335–342.
- [19] F. Wagner et al., *Phys. Rev. Lett.* **49**, 1408 (1982). **URL**
- [20] Y. R. Martin and T. Takizuka and the CDBM H-mode Threshold Database Working Group ITPA, *Journal of Physics: Conference Series* **123**, 012033 (2008). **URL**
- [21] F. Ryter et al., *Nuclear Fusion* **49**, 062003 (2009). **URL**
- [22] M. Cavedon, Phd thesis, Technische Universität München, 2016.
- [23] J. W. Connor and H. R. Wilson, *Plasma Physics and Controlled Fusion* **42**, R1 (2000). **URL**
- [24] E. Viezzer et al., *Nuclear Fusion* **54**, 012003 (2014). **URL**
- [25] J. Linke et al., *Nuclear Fusion* **51**, 073017 (2011). **URL**
- [26] A. Herrmann et al., *Journal of nuclear materials* **313**, 759 (2003). **URL**
- [27] G. Federici, A. Loarte, and G. Strohmayer, *Plasma Physics and Controlled Fusion* **45**, 1523 (2003). **URL**
- [28] J. Freidberg, *Ideal magnetohydrodynamics, Modern Perspectives in Energy Series* (Plenum Publishing Company Limited, 1987).
- [29] D. Schnack, *Lectures in Magnetohydrodynamics: With an Appendix on Extended MHD, Lecture Notes in Physics* (Springer Berlin Heidelberg, 2009).
- [30] H. Zohm, *Magnetohydrodynamic Stability of Tokamaks* (Wiley, 2014).
- [31] H. Alfven, *Nature* **150**, 405 (1942). **URL**
- [32] J. W. S. Rayleigh, *Proceedings of the London Mathematical Society* **s1-14**, 170 (1882). **URL**
- [33] G. I. Taylor, **201**, 192 (1950). **URL**
- [34] A. G. Peeters, *Plasma Physics and Controlled Fusion* **42**, B231 (2000). **URL**
- [35] M. Keilhacker et al., *Plasma Physics and Controlled Fusion* **26**, 49 (1984). **URL**
- [36] H. Zohm, *Plasma Phys.Control.Fusion* **38**, 105 (1996). **URL**

- [37] E. J. Doyle *et al.*, *Physics of Fluids B: Plasma Physics* **3**, 2300 (1991). [URL](#)
- [38] P. Gohil *et al.*, *Phys. Rev. Lett.* **61**, 1603 (1988). [URL](#)
- [39] S.-I. Itoh, K. Itoh, and A. Fukuyama, *Nuclear Fusion* **33**, 1445 (1993). [URL](#)
- [40] J. Connor, R. Hastie, H. Wilson, and R. Miller, *Physics of plasmas* **5**, 2687 (1998). [URL](#)
- [41] J. W. Connor, *Plasma Physics and Controlled Fusion* **40**, 531 (1998). [URL](#)
- [42] H. Zohm *et al.*, *Nuclear Fusion* **35**, 543 (1995). [URL](#)
- [43] P. B. Snyder *et al.*, *Phys. Plasmas* **16**, 056118 (2009). [URL](#)
- [44] M. G. Dunne *et al.*, *Plasma Physics and Controlled Fusion* **59**, 025010 (2017). [URL](#)
- [45] A. Y. Aydemir, *Physics of Plasmas* **14**, 056118 (2007). [URL](#)
- [46] J. A. Morales *et al.*, *Physics of Plasmas* **23**, 042513 (2016). [URL](#)
- [47] F. Orain *et al.*, *Phys. Rev. Lett.* **114**, 035001 (2015). [URL](#)
- [48] A. Kirk *et al.*, *Nuclear Fusion* **54**, 114012 (2014). [URL](#)
- [49] T. Eich, A. Herrmann, and J. Neuhauser, *Phys. Rev. Lett.* **91**, 195003 (2003). [URL](#)
- [50] T. Eich *et al.*, *Plasma Physics and Controlled Fusion* **47**, 815 (2005). [URL](#)
- [51] A. Kirk *et al.*, *Phys. Rev. Lett.* **96**, 185001 (2006). [URL](#)
- [52] J. H. Yu *et al.*, *Physics of Plasmas* **15**, 032504 (2008). [URL](#)
- [53] J. Boom *et al.*, *Nuclear Fusion* **51**, 103039 (2011). [URL](#)
- [54] J. E. Lee *et al.*, *Scientific Reports* 45075 (2017). [URL](#)
- [55] W. L. Zhong *et al.*, *Plasma Physics and Controlled Fusion* **58**, 065001 (2016). [URL](#)
- [56] H. Wang *et al.*, *Nuclear Fusion* **54**, 043014 (2014). [URL](#)
- [57] F. Mink *et al.*, *Plasma Physics and Controlled Fusion* **58**, 125013 (2016). [URL](#)
- [58] J. Terry *et al.*, *Journal of Nuclear Materials* **363 - 365**, 994 (2007). [URL](#)
- [59] R. Maingi *et al.*, *Nuclear Fusion* **45**, 1066 (2005). [URL](#)
- [60] C. Perez *et al.*, *Nuclear Fusion* **44**, 609 (2004). [URL](#)

-
- [61] F. M. Poli, S. E. Sharapov, and S. C. Chapman, *Plasma Physics and Controlled Fusion* **50**, 095009 (2008). **URL**
- [62] R. Wenninger, H. Reimerdes, O. Sauter, and H. Zohm, *Nuclear Fusion* **53**, 113004 (2013). **URL**
- [63] G. Huysmans and O. Czarny, *Nuclear Fusion* **47**, 659 (2007). **URL**
- [64] O. Czarny and G. Huysmans, *Journal of Computational Physics* **227**, 7423 (2008). **URL**
- [65] A. F. Mink *et al.*, *Nuclear Fusion* **58**, 026011 (2018). **URL**
- [66] M. Hölzl *et al.*, *Journal of Physics: Conference Series* **401**, 012010 (2012). **URL**
- [67] F. Orain, Thesis, Aix-Marseille Université ; CEA IRFM, 2014.
- [68] JOREK web page, <https://www.jorek.eu/>, accessed: 2017-11-23.
- [69] I. H. Hutchinson, *Principles of Plasma Diagnostics*, 2nd ed. ed. (Cambridge Univ.Press, 2002).
- [70] R. Pasqualotto *et al.*, *Review of Scientific Instruments* **75**, 3891 (2004). **URL**
- [71] F. Glass *et al.*, *Review of Scientific Instruments* **87**, 11E508 (2016). **URL**
- [72] B. Kurzan and H. D. Murmann, *Review of Scientific Instruments* **82**, 103501 (2011). **URL**
- [73] J. Schweinzer *et al.*, *Plasma Physics and Controlled Fusion* **34**, 1173 (1992). **URL**
- [74] H. Stoschus *et al.*, *Review of Scientific Instruments* **83**, 10D508 (2012). **URL**
- [75] M. Brix *et al.*, *Review of Scientific Instruments* **83**, 10D533 (2012). **URL**
- [76] M. Willensdorfer *et al.*, *Plasma Physics and Controlled Fusion* **56**, 025008 (2014). **URL**
- [77] S. Schmuck *et al.*, *Review of Scientific Instruments* **83**, 125101 (2012). **URL**
- [78] D. D. Truong and M. E. Austin, *Review of Scientific Instruments* **85**, 11D814 (2014). **URL**
- [79] H. J. Hartfuss, T. Geist, and M. Hirsch, *Plasma Physics and Controlled Fusion* **39**, 1693 (1997). **URL**

- [80] S. S. Denk *et al.*, *Proceedings of the 44th EPS Plasma Physics Conference* (2017).
- [81] S. S. Denk *et al.*, EPJ Web Conf. **147**, 02002 (2017). **URL**
- [82] S. K. Rathgeber *et al.*, Plasma Physics and Controlled Fusion **55**, 025004 (2013). **URL**
- [83] A. C. C. Sips and G. J. Kramer, Plasma Physics and Controlled Fusion **35**, 743 (1993). **URL**
- [84] L. Zeng *et al.*, Nuclear Fusion **46**, S677 (2006). **URL**
- [85] A. Medvedeva *et al.*, *Proceedings of the 44th EPS Plasma Physics Conference* (2017).
- [86] D. Prisiazhniuk *et al.*, Plasma Physics and Controlled Fusion **59**, 025013 (2017). **URL**
- [87] A. Silva *et al.*, Review of Scientific Instruments **67**, 4138 (1996). **URL**
- [88] M. Manso *et al.*, Plasma Physics and Controlled Fusion **40**, 747 (1998). **URL**
- [89] L. Guimaraes *et al.*, Nuclear Fusion (2017). **URL**
- [90] A. Mlynek *et al.*, Review of Scientific Instruments **81**, 033507 (2010). **URL**
- [91] R. C. Isler, Physica Scripta **35**, 650 (1987). **URL**
- [92] E. Viezzer *et al.*, Review of Scientific Instruments **83**, 103501 (2012). **URL**
- [93] M. Cavedon *et al.*, Review of Scientific Instruments **88**, 043103 (2017). **URL**
- [94] R. Fischer *et al.*, Fusion Science and Technology **58**, 675 (2010). **URL**
- [95] E. J. Strait, E. D. Fredrickson, J.-M. Moret, and M. Takechi, Fusion Science and Technology **53**, 304 (2008). **URL**
- [96] M. Brusati *et al.*, Computer Physics Reports **1**, 345 (1984). **URL**
- [97] F. Klossek, Bachelor thesis, LMU München, 2017.
- [98] L. Horváth *et al.*, Plasma Physics and Controlled Fusion **57**, 125005 (2015). **URL**
- [99] F. Sommer *et al.*, Plasma Physics and Controlled Fusion **53**, 085012 (2011). **URL**
- [100] A. Schmid, Diplomarbeit, Technische Universität München, 1997.

- [101] N. Winsor, J. Johnson, and J. Dawson, *Physics of fluids* **11**, 2448 (1968). **URL**
- [102] C. Perez *et al.*, *Plasma Physics and Controlled Fusion* **46**, 61 (2004). **URL**
- [103] A. Diallo *et al.*, *Physics of Plasmas* **22**, (2015). **URL**
- [104] A. Kallenbach *et al.*, *Journal of Nuclear Materials* **290-293**, 639 (2001), 14th Int. Conf. on Plasma-Surface Interactions in Controlled Fusion Devices. **URL**
- [105] M. Beurskens *et al.*, *Nuclear Fusion* **48**, 095004 (2008). **URL**
- [106] M. Dunne *et al.*, *Nuclear Fusion* **52**, 123014 (2012). **URL**
- [107] F. M. Laggner *et al.*, *Plasma Physics and Controlled Fusion* **58**, 065005 (2016). **URL**
- [108] A. Burckhart *et al.*, *Plasma Physics and Controlled Fusion* **52**, 105010 (2010). **URL**
- [109] D. R. Hatch *et al.*, *Nuclear fusion* **55**, 063028 (2015). **URL**
- [110] M. Cavedon *et al.*, *Plasma Physics and Controlled Fusion* **59**, 105007 (2017). **URL**
- [111] M. Hoelz, S. Guenter, and R. P. Wenninger, *Physics of plasmas* **19**, (2012). **URL**
- [112] I. Krebs, M. Hoelzl, K. Lackner, and S. Guenter, *Physics of plasmas* **20**, (2013). **URL**
- [113] E. Viezzer *et al.*, *Nuclear fusion* **53**, 053005 (2013). **URL**
- [114] P. Manz *et al.*, *Nuclear Fusion* **55**, 083004 (2015). **URL**
- [115] C. Maszl *et al.*, *Journal of Nuclear Materials* **415**, S451 (2011), proceedings of the 19th International Conference on Plasma-Surface Interactions in Controlled Fusion. **URL**
- [116] A. Kirk *et al.*, *Plasma Physics and Controlled Fusion* **53**, 035003 (2011). **URL**
- [117] P. Manz *et al.*, *Physics of Plasmas (1994-present)* **20**, (2013). **URL**
- [118] P. Manz, J. E. Boom, E. Wolfrum, and G. Birkenmeier, *Plasma Physics and Controlled Fusion* **56**, 035010 (2014). **URL**
- [119] K. V. Roberts and J. B. Taylor, *Phys. Rev. Lett.* **8**, 197 (1962). **URL**
- [120] B. Vanovac *et al.*, *Proceedings of the 44th EPS Plasma Physics Conference* (2017).

- [121] R. L. Miller, F. L. Waelbroeck, A. B. Hassam, and R. E. Waltz, *Physics of Plasmas* **2**, 3676 (1995). **URL**
- [122] S. C. Cowley, H. Wilson, O. Hurricane, and B. Fong, *Plasma Physics and Controlled Fusion* **45**, A31 (2003). **URL**
- [123] W. Fundamenski *et al.*, *Plasma Physics and Controlled Fusion* **49**, R43 (2007). **URL**
- [124] P. Diamond, *Relaxation Dynamics in Laboratory and Astrophysical Plasmas, Biennial reviews of the theory of magnetized plasmas* (World Scientific, 2010).
- [125] F. Massi, L. Baillet, O. Giannini, and A. Sestieri, *Mechanical Systems and Signal Processing* **21**, 2374 (2007). **URL**
- [126] G. Kerschen, *Modal Analysis of Nonlinear Mechanical Systems, CISM International Centre for Mechanical Sciences* (Springer Vienna, 2014).
- [127] P. B. Snyder *et al.*, *Phys. Plasmas* **9**, 2037 (2002). **URL**
- [128] P. W. Xi, X. Q. Xu, and P. H. Diamond, *Phys. Rev. Lett.* **112**, 085001 (2014). **URL**
- [129] S.-I. Itoh, K. Itoh, H. Zushi, and A. Fukuyama, *Plasma Physics and Controlled Fusion* **40**, 879 (1998). **URL**
- [130] R. J. Maqueda and R. Maingi, *Physics of Plasmas* **16**, 056117 (2009). **URL**
- [131] G. Harrer, *Diplomarbeit, Technische Universität Wien*, 2016.
- [132] P. McCarthy, *Physics of Plasmas* **6**, 3554 (1999).
- [133] M. Willensdorfer *et al.*, *Review of Scientific Instruments* **83**, 023501 (2012). **URL**
- [134] F. Orain *et al.*, *Physics of Plasmas* **20**, 102510 (2013).
- [135] S. Pamela *et al.*, *Nuclear Fusion* **57**, 076006 (2017). **URL**
- [136] M. Hoelzl *et al.*, *Physics of Plasmas* **19**, 082505 (2012).
- [137] L. Spitzer and R. Härm, *Phys. Rev.* **89**, 977 (1953). **URL**
- [138] R. C. Malone, R. L. McCrory, and R. L. Morse, *Phys. Rev. Lett.* **34**, 721 (1975). **URL**
- [139] M. Hoelzl *et al.*, *Nuclear Fusion* **49**, 115009 (2009). **URL**

- [140] O. Sauter *et al.*, *Phys. Plasmas* **4**, 1654 (1997).
- [141] A. Gude, S. Günter, S. Sesnic, and ASDEX Upgrade Team, *Nucl. Fusion* **39**, 127 (1997). **URL**
- [142] X. Q. Xu *et al.*, *Phys. Rev. Lett.* **105**, 175005 (2010). **URL**
- [143] M. Hoelzl *et al.*, *Journal of Physics: Conference Series* **401**, 012010 (2012). **URL**
- [144] O. Sauter, C. Angioni, and Y. R. Lin-Liu, *Physics of Plasmas* **6**, 2834 (1999). **URL**
- [145] in *Statistik: Datenanalyse und Wahrscheinlichkeitsrechnung* (Springer Berlin Heidelberg, 2005), pp. 101–135.
- [146] H. R. Wilson and R. L. Miller, *Physics of Plasmas* **6**, 873 (1999). **URL**
- [147] A. Hasegawa, C. G. MacLennan, and Y. Kodama, *The Physics of Fluids* **22**, 2122 (1979). **URL**
- [148] H. Xia and M. G. Shats, *Phys. Rev. Lett.* **91**, 155001 (2003). **URL**
- [149] P. Manz, M. Ramisch, and U. Stroth, *Plasma Physics and Controlled Fusion* **51**, 035008 (2009). **URL**
- [150] L. Frassinetti *et al.*, *Nuclear Fusion* **55**, 023007 (2015). **URL**
- [151] T. Eich *et al.*, *Nuclear Materials and Energy* **12**, 84 (2017), proceedings of the 22nd International Conference on Plasma Surface Interactions 2016, 22nd PSI. **URL**
- [152] E. Trier *et al.*, *Nuclear Fusion* (submitted 2017).
- [153] R. Colchin *et al.*, *Nuclear Fusion* **42**, 1134 (2002). **URL**
- [154] G. D. Conway *et al.*, *Phys. Rev. Lett.* **106**, 065001 (2011). **URL**
- [155] G. Xu *et al.*, *Nuclear Fusion* **54**, 103002 (2014). **URL**
- [156] G. Birkenmeier *et al.*, *Nuclear Fusion* **56**, 086009 (2016). **URL**
- [157] K. Itoh, S.-I. Itoh, and A. Fujisawa, *Plasma and Fusion Research* **8**, 1102168 (2013).
- [158] A. Medvedeva *et al.*, *Plasma Physics and Controlled Fusion* **59**, 125014 (2017). **URL**
- [159] M. Cavedon *et al.*, *Nuclear Fusion* **57**, 014002 (2017). **URL**

- [160] A. Kallenbach *et al.*, Plasma Physics and Controlled Fusion **55**, 124041 (2013).
URL
- [161] J. Schweinzer *et al.*, Nuclear Fusion **51**, 113003 (2011). **URL**
- [162] P. A. Schneider *et al.*, Plasma Physics and Controlled Fusion **56**, 025011 (2014).
URL
- [163] T. E. Evans *et al.*, Nature Physics **2**, 419 (2006). **URL**
- [164] Y. Liang *et al.*, Phys. Rev. Lett. **98**, 265004 (2007). **URL**
- [165] W. Suttrop *et al.*, Phys. Rev. Lett. **106**, 225004 (2011). **URL**
- [166] M. Willensdorfer *et al.*, Phys. Rev. Lett. **119**, 085002 (2017). **URL**
- [167] M. Bécoulet *et al.*, Phys. Rev. Lett. **113**, 115001 (2014). **URL**
- [168] H. Strauss *et al.*, Nuclear Fusion **49**, 055025 (2009). **URL**
- [169] EuroFusion, JET main features,
<https://www.euro-fusion.org/jet/jets-main-features/>, accessed: 2017-12-14.

Appendix A.

Details of the JOREK Run

The simulations presented in section 6.3 are based on a CLISTE equilibrium reconstruction using pre-ELM profile measurements (the corresponding ASDEX Upgrade shot file is found at micdu:eqb:33616:1:7.2s). The safety factor and pressure profiles are shown in Figure 2.4 along with the finite element grid used for the simulations (about 14000 elements in the poloidal plane). The resistivity is given by $\eta = \eta_0 \cdot (T/T_0)^{-3/2}$ where T_0 denotes the initial temperature in the center of the plasma, and $\eta_0 = 1 \cdot 10^{-7}$ in normalized units corresponding to about $2.5 \cdot 10^{-7} \Omega\text{m}$ in SI units. The viscosity profile is set up with the same temperature dependency and an initial center value of $3 \cdot 10^{-8}$ in normalized units corresponding to about $0.05 \text{m}^2/\text{s}$. Neoclassical effects are considered in the form of a neoclassical tensor similar as described in Ref. [134], using constant coefficients: neoclassical friction is $\mu_{\text{neo}} = 1 \cdot 10^{-5}$ in normalized units, corresponding to about 17.7s^{-1} , and neoclassical heat conductivity is $k_{\text{i,neo}} = -1$. Hyperresistivity and hyperviscosity are spatially constant and set up in a way that in the region of the instability $\eta_H \approx \eta^2$ and $\nu_H \approx \nu^2$ ensuring that they do not influence simulation results. Heat and particle source profiles are very simplified, and the perpendicular heat and particle diffusion coefficients are set up in a way that on the time scale of the ELM crash, profiles do not change significantly in an axisymmetric simulation without instability. This in particular means they are strongly reduced in the pedestal region to model the edge transport barrier. A more careful setup of sources and diffusivities in line with experimental measurements is required in future cases to simulate full ELM cycles. The JOREK input files are available upon request. The JOREK version used to perform the simulation corresponds to version 8206ec4bd37325e2dad0cb44356ceae31b942d2a of the develop branch in the central git repository as of November 30th 2016.

Danksagung

Abschließend möchte ich mich herzlichst bei allen bedanken, die mich während der Entstehung dieser Arbeit unterstützt haben:

- **Ulrich Stroth** für seinen umfassenden und hilfreichen Einsatz als mein Doktorvater. Ich habe deine ehrliche und direkte Art immer sehr gemocht und wusste daher immer woran ich bin. Unsere vielen Gespräche haben mir an manchen Stellen einen entscheidenden Impuls gegeben. Ich habe mich dabei immer ernst genommen und durch deinen leichten hessischen Dialekt manchmal richtig heimisch gefühlt. Besonders werden mir deine akribischen Korrekturen in Erinnerung bleiben. Die waren zwar auch frustrierend, aber im Rückblick habe ich daraus vor allem viel gelernt. Das wichtigste ist aber natürlich, dass du mir überhaupt ermöglicht hast diese Arbeit schreiben zu können, denn ohne Doktorvater gibt es auch keinen Doktor.
- **Elisabeth Wolfrum** für ihren herzlichen und kompetenten Einsatz als meine Betreuerin. Du warst die treibende Kraft hinter meiner Arbeit, insbesondere in den ersten Monaten als es darum ging erste Ergebnisse zu produzieren und diese gegen viel Gegenwind durchzusetzen. Du hattest immer Zeit und Interesse über neue oder alte Themen zu diskutieren und ich bewundere den hohen zeitlichen Aufwand, den du dafür investiert hast. Ich weiß außerdem sehr zu schätzen, dass du mich immer in meinen Ideen, Plänen und Meinungen unterstützt hast, auch wenn diese mal gegen deine oder eine konventionelle Meinung standen. Ich glaube es zeugt von viel Weisheit, Erfahrung und Herzlichkeit offen gegenüber solchen Meinungen zu sein. Am meisten hat mich aber deine positive Einstellung und Begeisterungsfähigkeit zu allen Themen fasziniert. Aus jedem noch so kleinen Ergebnis konntest du eine beeindruckende Interpretation hervorbringen und mich auf die richtigen Bahnen lenken.
- **Matthias Hölzl** und **François Orain** für die JOREK Auswertungen und die Diskussionen aus der Sicht von Theoretikern. Ich verdanke euch einen großen Anteil meiner Arbeit. Ohne den schönen Vergleich zur Theorie wäre meine Arbeit sicher weniger wert. Ich finde es gleichzeitig sehr gut, dass wir nun zusammen einen Anstoß geben konnten, der in Zukunft mehr Kooperation zwischen Theorie und Experiment zulässt.

- Bei allen Helferinnen und Helfern, die mir ihre Diagnostiken, Routinen, Auswertungen oder Grafiken zur Verfügung gestellt haben. Ich konnte was das angeht wirklich aus dem Vollen schöpfen. Dazu zählen Magnetikdaten, IDA-Auswertungen, Bikohärenzanalysen, Rotationsmessungen, MISHKA-Auswertungen, Reflektometerdaten und vieles vieles mehr. Die wichtigsten hier zu nennenden Leute sind **Marc Maraschek, Sina Fietz, László Horváth, Felix Klossek, Florian Laggner, Georg Harrer, Eli Viezzer, Marco Cavedon, Mike Dunne, Pascale Hennequin, Luís Gil, Matthias Willensdorfer** und das **ASDEX Upgrade Team**.
- Bei allen anderen, die mich durch Diskussionen oder neue, spannende Ideen weitergebracht haben. Hier möchte ich besonders **Peter Manz, Hartmut Zohm, Gregor Birkenmeier** und **Branka Vanovac** hervorheben.
- Bei all denen, die mich bei meinem JET Aufenthalt unterstützt und zu diesem bewegt haben. Dies sind vor allem **Thomas Eich, Emila Solano** und das **JET Team**.
- Bei den Sekretärinnen für das Organisatorische. Danke für die Hilfe bei Dienstreiseanträgen, Gleitzeitformularen, Büromaterialausgabe, Krankheitsattesten, Flugbuchungen und mehr vor allem an **Gabi Dörsch** und **Biggy Perey**.
- Bei allen Kolleginnen und Kollegen, die für mich vor allem persönlich sehr wichtig waren und den Rahmen für ein sehr gutes Arbeitsklima gebildet haben. Dazu zählen die Essens-Crew, die Doktorandensprecherkollegen, die Spieleabendler, die Konferenz-networking-people, die Doppelplasma-Aufbauer, die Doktorandenfeiern-Aufräumer, die Betriebsausflug-Bergsteiger, das Besuchertouren-Team, die Oktoberfestler und viele mehr, aber am meisten die weltbesten Bürokollegen **Michael Griener** und **Javier Pinzón**. Besonders ihr beide habt mich drei Jahre lang ausgehalten, bespaßt, genervt, erfreut, vorangebracht. Ihr habt mit mir gelacht, getratscht, diskutiert und euch mit mir aufgeregt. Kurzum, es war einfach eine super Zeit mit euch!

Zu allerletzt möchte ich mich bei meinen **Freunden** und meiner **Familie** bedanken. Ihr habt mir auf eure ganz persönliche und individuelle Weise geholfen. Ohne euch wäre der lange Weg bis zu dieser Arbeit nicht möglich gewesen. Insbesondere habt ihr, liebe Geschwister, mir diesen Weg vorgelebt und ihr, liebe Eltern, diesen Weg unterstützt! Ein spezieller Dank gilt meiner Verlobten, **Wiebke Pier**, die mir in jeder Situation zur Seite stand.